Framework for Multi-Vehicle Adaptive Sampling of Jets and Plumes in Coastal Zones

by

Matthew Lee Gildner

S.B., Massachusetts Institute of Technology (2011)

Submitted to the Department of Mechanical Engineering
in partial fulfillment of the requirements for the degree of

Masters of Science in Mechanical Engineering

at the

MASSACHUSETTS INSTITUTE OF TECHNOLOGY

February 2013

Author .....
Department of Mechanical Engineering
December 12th, 2012

Certified by .....
Nicholas M. Patrikalakis
Kawasaki Professor of Engineering
Thesis Supervisor

Accepted by .....
David E. Hardt
Graduate Officer, Department of Mechanical Engineering

Framework for Multi-Vehicle Adaptive Sampling of Jets and Plumes in Coastal Zones

by

Matthew Lee Gildner

Submitted to the Department of Mechanical Engineering
on December 12th, 2012, in partial fulfillment of the
requirements for the degree of
Masters of Science in Mechanical Engineering

Abstract

This thesis presents a framework for the sampling of thermal and effluent jets and plumes using multiple autonomous surface vehicles. The framework was developed with the goal of achieving rapid and accurate in-situ measurement and characterization of these features. The framework is presented as a collection of simulation, estimation and field tools for use within the Mission Oriented Operations Suite (MOOS) and a novel Acoustic Doppler Current Profiling system that is capable of reorientation and real-time feedback. Key features developed within MOOS include a multi-parameter model of thermal and effluent jet and plume fields, online parameter estimation and sensor fusion. Using these tools, a collaborative adaptive sampling strategy is implemented to efficiently sample an industrial jet and plume. The capabilities of this strategy are demonstrated in realistic mission simulations and in field trials using a fleet of autonomous kayaks equipped with environmental sensors.

Thesis Supervisor: Nicholas M. Patrikalakis
Title: Kawasaki Professor of Engineering

Acknowledgments

This thesis would not have been possible without the support of many people. Foremost, I would like to thank my advisor, Professor Nicholas Patrikalakis, for his continued guidance and support. I would also like to thank Dr. Gabriel Weymouth, who was always available to discuss ideas and provide key suggestions throughout the development of this thesis. Professor Franz Hover also assisted me in structuring this thesis, in addition to providing me with valuable mentorship during my time at MIT.

The work presented in this thesis makes extensive use of the MOOS-IvP autonomy system. Early on in the development of this work I was able to participate in a new course focused on MOOS-IvP led by Professor Henrik Schmidt and Dr. Michael Benjamin. The skills and concepts I learned in this course proved to be invaluable and helped to shape the direction of this thesis.

I would also like to thank members of my research group and colleagues in Singapore. Jacob I., thanks for you insightful mechanical design suggestions. Josh L., I am very grateful for your essential help with software development and our thought-provoking discussions about the future of marine robotics. The field tests conducted in Singapore as part of this thesis would not have been possible without the help of Tawfiq T. and Tony V. Their tireless contributions and practical knowledge related to marine robotics could not be appreciated enough.

I would also like to thank my friends and family who have supported me since I began my studies at MIT as an undergraduate. Many long days and nights spent working on difficult problems were made better through them.

This research was supported by the American Board of Shipping, the National Research Foundation of Singapore through the Singapore-MIT Alliance for Research and Technology's (SMART) Center for Environmental Sensing and Modeling (CENSAM) IRG Research Program.

This doctoral thesis has been examined by a Committee of the Department of Chemistry as follows:

Professor Jianshu Cao .....
Chairman, Thesis Committee
Professor of Chemistry

Professor Troy Van Voorhis .....
Thesis Supervisor
Associate Professor of Chemistry

Professor Robert W. Field .....
Member, Thesis Committee
Haslam and Dewey Professor of Chemistry

Contents

List of Figures

List of Tables

List of Jet and Plume Model Symbols

(x, y)	Global Cartesian Coordinates	57
(x', y')	Local Jet Cartesian Coordinates	63
(X_O, Y_O)	Virtual Origin of Jet	57
α_i	Jet Field, i.e. Velocity, Temperature or Salinity	58
ϕ	Ambient Current Angle	57
θ	Jet Angle	57
B_O	Buoyancy Momentum Flux	60
C	Trajectory Coefficient	63
D	Jet Diameter	57
$E_i(s, r)$	Non-Dimensionalized Excess Field Quantity	58
g'_O	Effective Gravity of the Source Fluid	60
H	Depth of Water	60
l_B	Buoyancy Length Scale	60
L_C	Steady Cross Flow Length Scale	62
L_O	Volume Flux Length Scale	58
M_O	Source Momentum Flux	58
N_i	Field Decay Coefficient	65
Q_O	Source Volume Flux	58
r	Radial Distance from Jet Centerline	57
R_i	Field Spreading Coefficient	65
S	Salinity Field	57

s	Distance Along Jet Centerline	57
S_a	Ambient Salinity	57
S_O	Source Salinity	57
s_O	Length of Zone of Flow Establishment	57
T	Temperature Field	57
T_a	Ambient Temperature	57
T_O	Source Temperature	57
u	Component of Current Field Aigned with x Axis	67
u'	Axial Velocity Along Jet Centerline	57
U_a	Ambient Current	57
U_C	Ambient Current Normal to Outfall	57
U_O	Source Velocity	57
V	Water Velocity Field	57
v	Component of Current Field Aigned with y Axis	67
v'	Radial Velocity Along Jet Centerline	57
Z_O	Depth of Outfall	60

Chapter 1

Introduction

The ability to rapidly and accurately sample and characterize marine features is essential to the effective planning of many human activities and understanding the world we live in. These features include local and global currents, biological and chemical plumes and densimetric stratification. Because these features are often dynamic and vary across a range of temporal and spatial scales, automated sampling and characterization processes using mobile platforms can obtain more accurate and complete results, while lowering the acquisition costs of this data.

Marine robotic platforms such as autonomous surface vehicles (ASVs) and autonomous underwater vehicles (AUVs) are ideal tools for marine sampling and characterization efforts due to their ability to autonomously navigate the marine environment and collect in-situ measurements. In order to leverage these capabilities and the increasing powerful computational resources deployed on these platforms, a framework is needed that integrates vehicle's autonomy systems and models of features. This thesis documents such a framework as it applies to thermal and effluent jets and plumes and autonomous surface vehicles.

1.1 Motivation For Sampling and Characterization of Marine Features

Mapping and tracking of coastal features, climate monitoring and environmental impact assessment are areas that benefit from rapid and accurate sampling and characterization of marine features.

1.1.1 Mapping and Tracking of Coastal Features

Due to economic, safety and security concerns, the operation of large harbors and ports requires extensive data about their marine environments. The Port of Singapore, the area of experimental focus of this thesis, offers a pertinent example. As of 2005, the Port of Singapore was the busiest in the world. In that year over 130,000 ships visited the port carrying over 1.15 billion gross registered tons (GRT) [56]. Efforts to coordinate and schedule the operation of these vessels can be affected by local features. Coastal currents can impact navigation, while tides and sediment transport limit ship mobility.

Harbor and port security can also benefit from automated sampling and characterization. By tracking wakes or acoustic and visual signatures, marine robots may be able to identify intrusions by unwanted personnel or vehicles. Mine counter-measures are particular important for the protection of military harbor assets. The detection of foreign objects attached to a ship traditionally requires trained divers working in dangerous conditions. Sampling and detection algorithms deployed on a autonomous marine vehicle could potentially lower or eliminate the need for human inspections.

1.1.2 Climate Monitoring and Environmental Impact Assessment

In order to better understand the earth's climate and how human activities impact it and our environment, wide-spread marine monitoring is needed. Global ocean circulation is suspected to relate to global warming [71] and regional currents, such

as the Loop Current found in the Gulf of Mexico, have been shown to alter the strength and trajectory of hurricanes [50]. In the case of an industrial disaster like the Exxon Valdez or Deepwater Horizon oil spills, tracking of pollutant and dispersant plumes is essential for cleanup and environmental damage assessment.

The data collected on these types of features is often use to improve numeric models of marine processes. Currently these models utilize data collected from remote sensing systems such as satellites [2, 21] and in-situ measurements taken from automated mobile platforms including Argo Profiling CTDs [62] and marine gliders [63]. In the case of mobile sensing platforms, intelligent deployment is key to the rapid and low cost collection of high value data. While the mobile platforms mentioned here are able to collect large amounts of marine data without the need for a human presence, they generally lack the ability to identify and direct their efforts towards regions of higher interest.

Intelligent deployment that maximizes utility is a challenge faced when deploying mobile sensing platforms in any environment. One approach to this challenge is to incorporate models of the sampled environment into the autonomy systems used to direct and control these platforms. The first step in this approach is the development of an appropriate model of a feature of interest such as a thermal and effluent jet.

1.2 Thermal and Effluent Jets and Plumes

Effluent jets and plumes are common features found in coastal environments. Sources include outfalls disposing fluids from waste-water treatment plants, cooling water from power plants and liquid by-products from industrial processes [58, 11, 1]. These features have been a topic of extensive study due both to their status as a benchmark of turbulent flow theory [59, 16] and the need to properly assess their impact on the environment[66, 51, 69, 74]. This thesis focuses on thermal and effluent jets and subsequent plumes produced at power plant cooling water outfalls.

1.2.1 Environmental Implications

Thermal and effluent jets have a number environmental effects which make them important features to monitor. Most well documented of these are their effects on fish and algal populations. Depending on seasonal changes and ambient conditions, the increased water temperatures in regions near the jets have been shown to alter fish local migratory patterns [66, 37]. This effect potentially increases the fishes' exposure to commercial fishing and predators. The elevated temperatures can also negatively impact the reproduction of some species [51].

Figure 1-1: Dead mullet accumulated after a harmful algal bloom related fish kill [25].

Harmful algal blooms (HABs) are caused by chlorophyll producing algal organisms or animal-like protozoans that cause harm to their surroundings due to the production of toxins or the accumulation of excessive biomass [5]. This harm can manifest itself in a number of ways including polluted shellfish populations or fish kills as shown in Figure 1-1. While HABs can arise naturally, in recent decades an increase in HABs has been observed and can be attributed to human activities. Nutrient influx due to sewage and animal waste as well as agricultural runoff are some of the known causes of these blooms [5]. Thermal effluent jets have also been linked to harmful algal blooms [69, 74]. In enclosed waterbodies such as China's Daya Bay, thermal effluent from power plants can cause widespread raised water temperatures. These increases appear to alter the seasonal occurrences of HABs. Since the opening of the first power plant along the Daya Bay in 1994, HABs have become prevalent all year around, where before they were simply a seasonal phenomenon in the fall and spring

[74].

1.2.2 Relevant Prior Work in Modeling and Characterization

Turbulent jet flows have been the centerpiece of numerous studies. The modeling effort in this thesis is primarily based on past theoretically analysis of these flows [59] and experimental characterization of the jet fields in a variety of outfall and ambient conditions [10, 65, 53, 49, 73] . These conditions typically relate to the location and geometry of the jet outfall, the relative density of the jet and ambient fluid and the presence of the crossflow. The thermal and effluent jets of interest to this study can generally be defined as buoyant turbulent horizontal jets subjected to a crossflow.

Being a benchmark of turbulent flow theory, jet flows have been extensively covered in literature. Typically, the round jet and plane jet model flows are used to better understand jet flows found in marine environments. These flows describe a fluid entering an infinite ambient environment from a submerged outfall with round or 2D geometry. These flows are part of a larger group of turbulent flows known as self-similar flows. The defining characteristic of self-similar flows is that specific aspects of their shape do not change in time [59]. This characteristic makes it possible to develop time invariant laws describing the geometry of the flow field, such as spreading rate and centerline decay. A brief discussion of jet model flows is given in Section 3.2.

Experimental investigations of turbulent jet flows enable scientists to bridge the gape between theoretical model flows and jet flows found in the environment. The results of these investigations can be used to establish empirical laws and generalizations related to certain jet flows. Section 3.3 demonstrates how generalized empirical laws can be used to develop a model of the thermal and effluent jet fields sampled in our robotic measurements. In [10] dimensional and length scale analysis is used to determine a set of independent parameters and length scales for a heated surface effluent jet entering a reversing crossflow. These parameters and length scales are related to laws defining the jet temperature field spreading, 2D trajectory and centerline decay.

1.3 Autonomy Architecture

The autonomy architecture developed in this thesis integrates the aforementioned modeling efforts, real-time estimation and adaptive sampling with existing tools for marine vehicle autonomous operations. The resulting architecture can be deployed in both simulation, in order to plan and develop sampling strategies, or in the field to effectively sample a thermal and effluent jet with ASVs.

1.3.1 Behavior-based Robotics and MOOS-IvP

This framework is developed as a collection of applications and behaviors within the popular open source Mission Oriented Operations Suite (MOOS) and MOOS-IvP software [7]. The strength of MOOS as a whole is the division of functionality into modules, including MOOS applications and IvP Behaviors, and the corresponding infrastructure within which these modules operate. Applications and behaviors are written in C++ and share a set of common libraries that enabled the shared infrastructure. The MOOS-IvP is an extension of MOOS that enables and coordinates behavior-based control of MOOS nodes and provides tools for custom behavior development and field deployment. A more detailed description of MOOS and MOOS-IvP is found in Appendix A.

1.3.2 Adaptive Sampling Approaches

Adaptive sampling is a broad term for sampling strategies that utilize information about the environment to direct automated sampling efforts and optimize the collection of critical data. Offline and online approaches an be implemented that make uses of real-time data and/or models of the environment. Adaptive sampling is a topic of much interest to the field of marine robotics and a variety of approaches have been proposed and tested in simulation and the field. Work by R. Smith, et a.l [67] has focused on using the Regional Ocean Model System [64] to develop marine glider trajectories with the goal of tracking the center and bounds of harmful algal blooms. This strategy utilizes intelligent planning offline to produce trajectories that

account for the predicted location of the feature and the effects of currents on vehicle navigation.

Other strategies apply algorithms that redirect platforms online using data collected in real-time and knowledge of sampled feature(s). Such an approach is implemented by D. Wang et a.l. to optimally sample the vertical thermocline using an AUV and assimilate the data in real-time to a ocean-acoustic model. Much like the autonomy architecture developed in this thesis, the strategy described in [72] is implemented within MOOS-IvP and leverages its multi-behavior optimization capabilities.

Real-time display of in-situ measurements has been used to adaptively sample plume features produced by industrial outfalls, [4], and oil spills, [40]. In both cases analysis of real-time data by humans was used to direct the trajectories of sensing vehicles to produce adaptive transects. In the case of [40], a deep water AUV capable of acoustic telemetry was used. Human-aided classification of real-time data streams was coupled with automated analysis to redirect the vehicle during its dive.

1.3.3 Sensing/Sampling Platforms

During the field trials documented in this thesis the sampling framework was deployed on SCOUT autonomous kayaks manufactured by Robotic Marine Systems [18]. These ASVs are capable of autonomous navigation and positioning through the MOOS-IvP system running on a onboard Linux/GNU computer. The vehicles are propelled by a rear azimuthing thruster and are powered by a 24V Lithium-Ion battery pack providing up to 4h of mission time. The maximum attainable speed of the vehicles is approximately 2m/s.

In addition to a Global Positioning System (GPS) sensor and Inertial Measurement Unit , a number of environmental sensors can be deployed on the ASVs and integrated into MOOS-IvP. During thermal effluent jet sampling missions an RD Instruments Workhorse Acoustic Doppler Current Profiler (ADCP) and a YSI multi-parameter sonde capable of measuring temperature, salinity, chlorophyll and pH are typically installed on the vehicles. An image of a SCOUT kayak with a YSI sonde is shown in

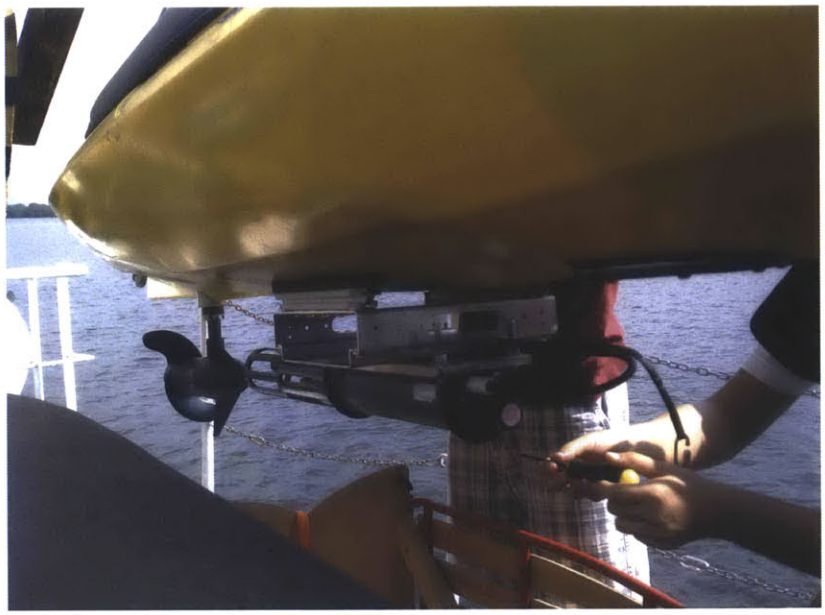

Figure 1-2: Image of a SCOUT kayak equipped with a YSI multi-parameter sonde.

Figure 1-2.

1.4 Thesis Structure

The goal of this thesis is to present a framework for multi-vehicle adaptive sampling of thermal and effluent jets and plumes using autonomous surface vehicles. This goal is achieved through the integrated application of feature modeling, parameter estimation and marine vehicle autonomy. To compliment these efforts and enhance the sampling platform used in the thesis, an augmented ADCP system was developed. The development and testing of these components is described in Chapters 2-4. Chapter 5 briefly summarizes these efforts and directs future development.

1.4.1 Reorienting ADCP

I begin by documenting the design and testing of a reorienting ADCP system in Chapter 2. The SCOUT kayak's inability to adequately reject large current disturbances can degrade the quality of the data it gathers, especially the velocity measurements obtained by an ADCP. For this reason as well as those documented in Section 2.2, an

improved ADCP system with a dynamic orientating capability was developed. This capability was achieved through the integration of a pan and tilt mounting apparatus with the ADCP transducer. Supplemental software drivers were also written to integrate the system within MOOS-IvP, providing mission level control of the system orientation and real-time processing and availability of the sensor's measurements.

1.4.2 Jet-Plume Field Model

Chapter 3 describes a thermal and effluent jet-plume field model and the parameter estimation methodology used to fit the model. The development of a jet-plume field model was driven by the need for a robust, configurable simulation environment for planning jet sampling missions and writing sampling autonomy behaviors. The model uses a selection of empirical laws describing a centerline decay, spreading and trajectory of an effluent jet to produce the jet-plume velocity, temperature and salinity fields based on outfall and ambient conditions. By applying parameter estimation to this model it is possible to fit the model to historical and in-situ data. This estimation is performed using a simulated annealing methodology. Parameter estimation techniques and results are discussed in Section 3.5.

For simulation purposes the model is implemented as a C++ library. It can be initialized and queried across the model space by simulation or autonomy software such as a simulated sensor, parameter estimator or field visualizer. Random noise can also be added to the model with user selected standard deviations based on sensor requirements. Figure 1-3 shows an image of a simulated jet temperature field produced by the new simulation visualization tool.

1.4.3 Autonomous Sampling Strategy

Chapter 4 begins by documenting a jet-plume sampling simulation environment developed through the integration of the jet model and estimation methodology with MOOS-IvP. I then document an adaptive sampling strategy implemented within MOOS-IvP and optimized within the simulation environment. Sampling strategy de-

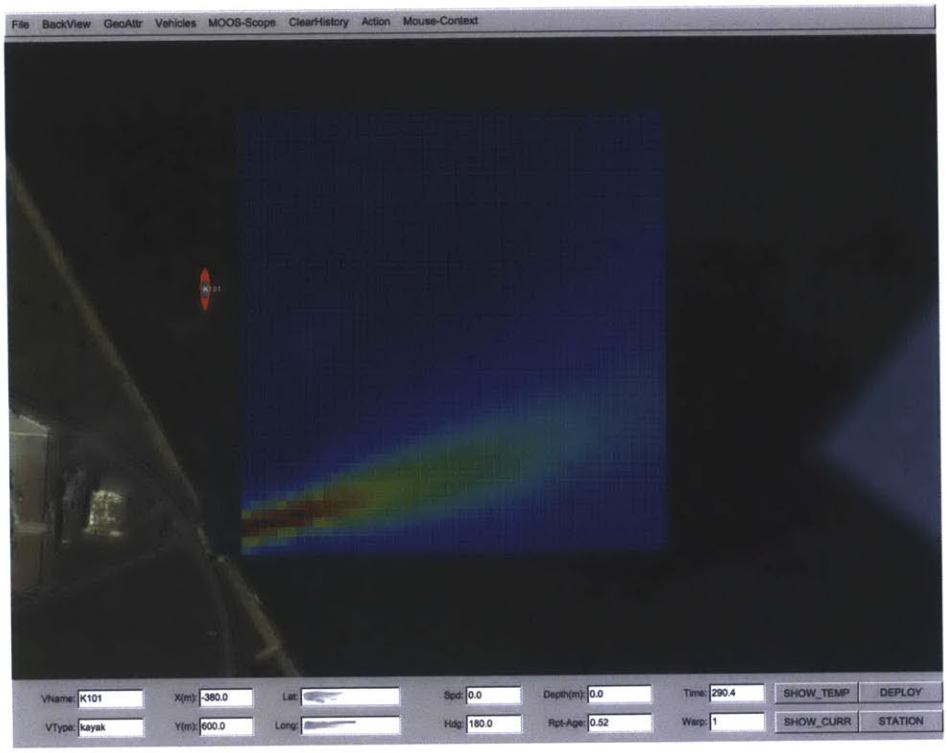

Figure 1-3: Overlay of the temperature field of a simulated jet at Site 2.

veloped in this thesis builds upon the adaptive strategies describe in [30, 47, 22, 11]. This strategy employs a sensor fusion and feature location method, referred to here as a the jet indicator function, and an adaptive transect behavior. The jet indicator function provides a means of using multiple sensor readings to localize a vehicle within a cross section of an thermal and effluent jet-plume. This function is consumed by the adaptive transect behavior to direct and bound a vehicle's transects of a jet. The implementation of this strategy within MOOS-IvP is described in Section 4.2. Simulation and field results are then presented in Sections 4.4-4.5.

Chapter 2

Design of Reorienting Acoustic Doppler Current Profiler

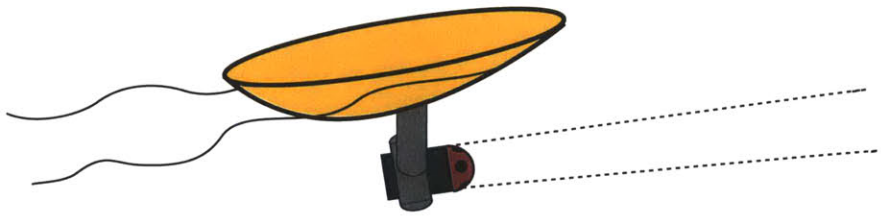

Figure 2-1: The reorienting ADCP system is mounted below a vehicle, in this case a kayak. The sensor can be panned and tilted to measure water velocities in different regions without moving the vehicle.

This chapter documents the development of a velocity measurement system designed to expand the sensing capabilities of marine surface vehicles. This is achieved through the integration a Teledyne RD Instruments Workhorse Broadband ADCP with a submersible pan and tilt motor mount. The novel mounting method allows the ADCP to be reorientated with 180° motion on the pan axis and 90° on the tilt axis, enabling the measurement of water velocity vectors in front of, beside and below a vehicle. A custom MOOS instrumentation application handles data parsing, measurement localization and transformation into global frame and publication. This system expands the velocity sensing area of vehicles with traditionally mounted ADCPs. This capability enables a vehicle to rapidly produce 3D velocity maps and sense

surface disturbances such as wakes. A simple drawing describing this system is shown in Figure 2-1.

This chapter beings with a brief discussion of relevant ADCP theory and the motivation for the new system in Section 2.1. The design of the mechanical and electrical components of the system is discussed in Sections 2.3 and 2.4. In Section 2.5 I document the design of the position control software for the pan and tilt mount. Section 2.6 documents the software supporting the control of the ADCP and real-time analysis of its data. Results of experimental tests of the system are presented in Section 2.8.

2.1 ADCP Theory

ADCPs measure water currents using the doppler effect. The doppler effect refers to the observed change in frequency of a wave form when the observer is moving relative to the source [28]. This change in frequency can be related to the relative velocity between the source and observer according to Eq. 2.1

$$F_d = F_s \frac{V}{C} \tag{2.1}$$

where F_d is the shifted frequency, F_s is the normal frequency, V is the relative velocity and C is the speed of the wave form when observer and source are stationary.

ADCPs are active instruments that measure reflections or echoes of waveforms produced by the sensor. Pressure waves produced by the sensor's piezo-electric transducers reflect off of sound scatters such as small particles or plankton. By analyzing the reflected signals the sensor is able to determine the relative velocity between the scatters and the transducer. Broadband ADCPs perform this analysis by sending out two pulses very close to one another and measuring phase lag between the returned signals. The frequency shift and relative velocity is then calculated from the lags [28].

Multiple transducers are oriented at different angles to allow the sensor to measure water velocity along different vectors through trigonometric relations. Profiling is achieved by range gating the reflected signals. Signals returned later result from

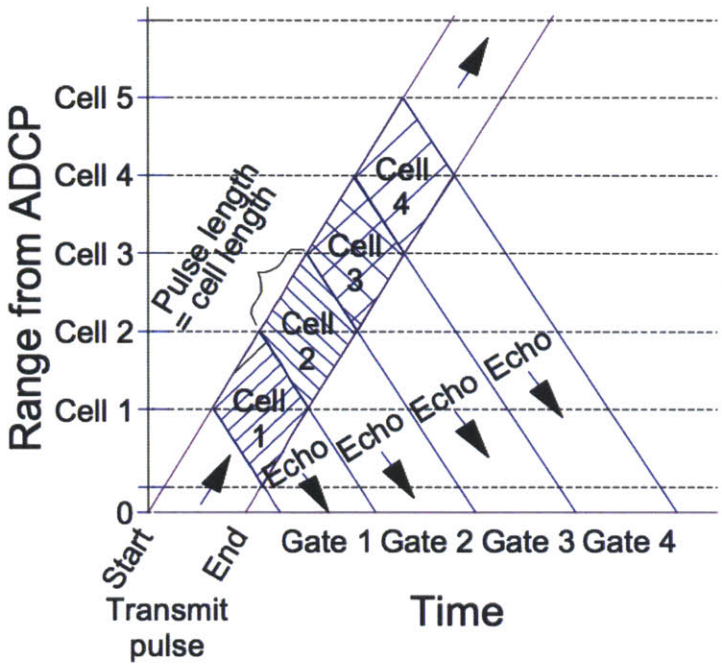

Figure 2-2: This range-time plot demonstrates the concept of ADCP range gating. The result of one pulse produces reflected or echo signals over a wide temporal range. By devisioning the returned signals along specific times, it is possible to analyze sets of signals that corrospond to specific measurement bins [28].

scatters that are farther away from the sensor; i.e. the return time of a signal can be related to the distance from the sensor. Thus, by averaging the results of all the signals returned during a period of time, an average measurement of the water velocity in the region corresponding to this period of time can be calculated. Each of these regions are referred to as measurement bins or depth cells [28]. A diagram demonstrating the concept of range gating and measurement bins is shown in Figure 2-2. Larger sized bins, while lowering profiling resolution, have the benefit of lowering measurement noise due to the increased number of signals averaged.

ADCPs are a dual purpose sensor. In addition to water velocity measurements, ADCPs can function as Doppler Velocity Loggers (DVLs). DVL measurements use the same principles as ADCPs to measure the relative velocity of the sensor and seabed. This capability can be used by dead reckoning algorithms for vehicle navigation [43, 61, 46]. While this capability is available for SCOUT kayaks, it is not essential

due to the availability of GPS and the low position accuracy requirements of most environmental measurements.

2.2 Motivation for Expanded Sensing Capability

Traditionally, vessel-mounted ADCPs are attached to the underside of vehicles and oriented towards the sea floor [70] as seen in Figure 2-3. This mounting method has several advantages that contribute to is widespread use. Foremost is the ability to combine two types of measurements taken by the sensor to obtain values for the absolute water velocity according to Eq. 2.2. Velocity measurements relative to the ADCP are taken along fixed bins normal to the ADCP face. At the same time, DVL measurements record the velocity of the ADCP relative to the seabed. By adding the DVL measurements, $\vec{v}_v$, to the measurements relative to the ADCP, $\vec{v}_{inst}$, the absolute velocity is obtained.

$$\vec{v}_w = \vec{v}_v + \vec{v}_{inst} \tag{2.2}$$

Another advantage of this configuration is current homogeneity across all four beams of the ADCP. The trigonometric relations used to calculate the velocity vectors of the current are simplified by assuming that each beam is measuring the water velocity at the same location. If the ADCP is oriented vertically, the beam measurement locations are in the approximately same horizontal plane, albeit at different points on this plane. Since marine currents tend towards homogeneity in the horizontal plane and the largest gradients occur along the z-axis, this assumption does not produce large errors in measurement [28].

Despite the advantages inherent to the traditional ADCP mounting configuration, this configuration limits how and where velocity measurements can be taken. These limitations, described in Section 2.2.1, are overcome by mounting the ADCP to the underside of an ASV using a pan/tilt mount. This approach also enables a vehicle to rapidly obtain three dimensional velocity maps in its vicinity and track high magnitude disturbances such as the wake of another vehicle.

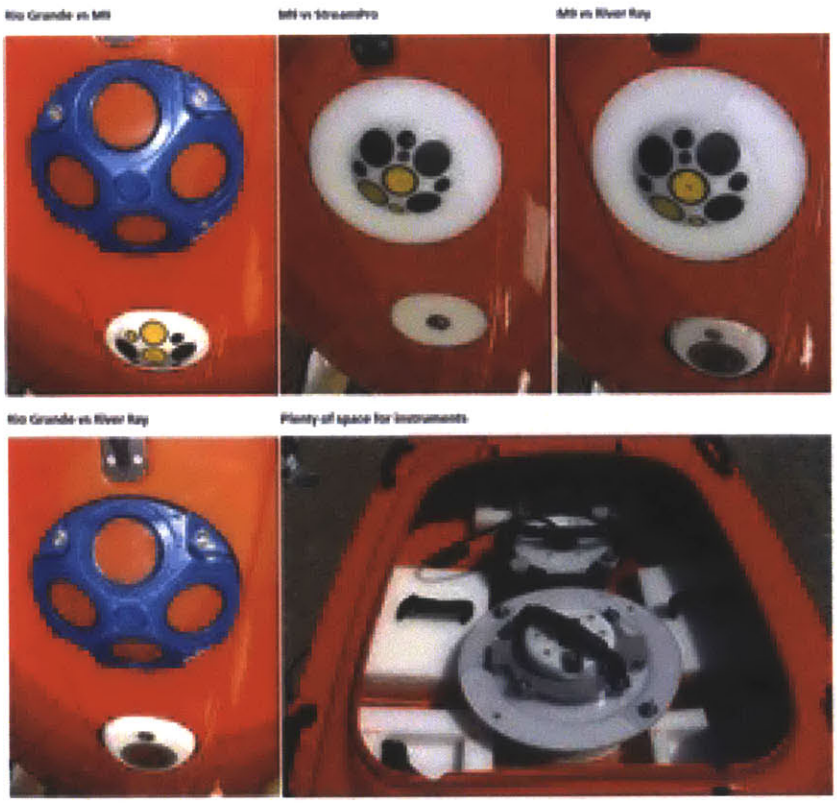

Figure 2-3: Several different models of ADCPs mounted on a remote controlled Q-Boat 1800P [55].

2.2.1 Limited Vehicle Operation Space

Despite the advantages inherent to the traditional ADCP mounting configuration, this configuration also has its limits. The disadvantages of the traditional mounting configuration include the limited area for which velocity measurements can be obtained and the inability to obtain undisturbed near surface measurements. A vehicle must be maneuvered over an area of interest before measurements can be made. Environmental conditions or operational restrictions can often limit the operational space of a surface vehicle, thus limiting the measurable area. In the case of surface measurements, the sampled volume is subjected to disturbances caused by the vehicle. These disturbances can affect the velocity measurements, making it difficult to obtain accurate near surface measurements from moving vehicles.

Both of these disadvantages are highlighted during the sampling of a effluent jet located on the surface. Near-surface velocity measurements near the outfall can be

used to evaluate effluent-ambient mixing and are valuable for model fitting. However, the strong currents produced here make it difficult to maintain the position of an ASV. Additionally, the presence of the outfall structures coupled with the decreased level of position control increases the chances of a collision when the ASV is maneuvering in close vicinity to the outfall. These issues are avoided when using a pan and tilt mounting scheme by orienting the ADCP horizontally ahead of the vehicle. This technique makes it possible to utilize the ADCP's range to obtain velocity measurements near the outfall, while maintaining a safe distance and avoiding the high flow regions.

2.2.2 Measurement and Tracking of Complex Flow Features

Complex, three dimensional, time-varying flows are common in coastal environments. Examples include river and industrial jet outfalls, surface and internal gravity waves and flow past man-made structures such as jetties. ADCPs are one of the few ways to obtain velocity measurements of these features in the marine environment. A reorienting ADCP could be used to produce 3D velocity maps of these features and track their changes over time with minimal movement by a vehicle. This capability would not be achievable with a statically mounted ADCP on a vessel or seafloor.

A flow feature of particular interest are wakes. These features are the result of disturbed flow behind a object that is moving relative to a fluid. The ability to detect and track wakes in real-time is mainly desirable from a security and military standpoint. A number of studies have investigated using acoustic systems to detect surface wakes [33, 39, 48]. In [33] Jeong et al. propose using an active sonar system mounted on the seabed to detect bubbles from surface vessel wakes. Their approach uses an adaptive detectection algorithm to compare the amplitude and time interval of the reflected signal to readings from non-wake conditions. Preliminary tests of the system in an ocean environment show promising results. The Naval Underwater Warfare Center have investigated using automated algorithms to filter echograph data from active sonar for harbor intruder detection. Vehicle wakes can be tracked using this system [39]. These proposed systems have some disadvantages. They rely on

statically mounted sonar instruments, so detection is restricted to the deployed area. These instruments also produce large data sets and thus complicated algorithms are required for detection and tracking.

The proposed mounting scheme would allow an ADCP to detect wakes in front of the platform it is mounted on and track the wakes as they move relative to the sensor. This capability is tested using the new ADCP system. The results of this test appear in Section 2.8.2.

2.3 Mechanical Design

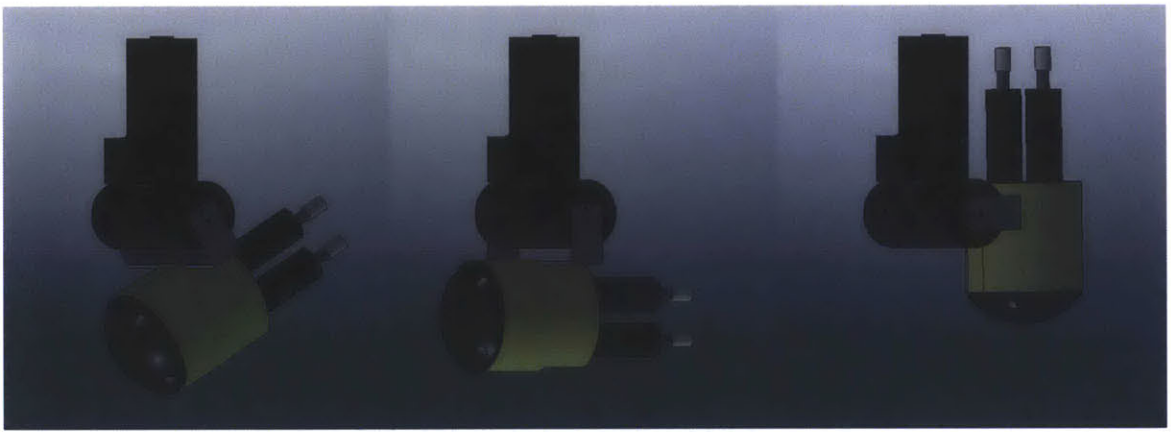

Figure 2-4: Solidworks Model of the Reorienting ADCP System

The major mechanical components of the reorienting ADCP system consist of the transducer housing and the pan and tilt mount. Efforts were made to minimize costs and manufacturing time due to limited resources and a three month design cycle. A rendering of the completed system is shown in Figure 2-4.

2.3.1 Housing

The primary objectives of the new transducer housing design are to maintain a dry environment on the side and rear of the transducer, to provide a secure mounting point for the pan/tilt plate, allow access to the transducer's electrical ports and simplify manufacturing. These objectives are achieved by using a cylindrical design that

mimics the geometry of a transducer mount on the underside of a vessel. Black ABS plastic is used for the housing material because of its generally good machinability, resistance to corrosion, low density and toughness. The basic design of the housing is shown in Fig. 2-5

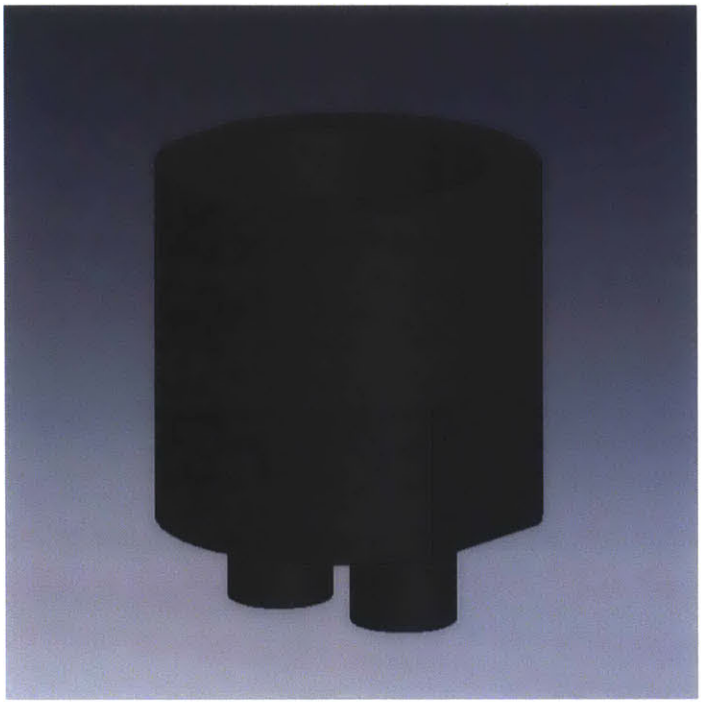

Figure 2-5: Solidworks Model of the Tranducer Housing

2.3.2 Pan/Tilt Mount

Several factors affected the selection of a suitable pan/tilt mount for the sensor system. The mount needed to be able to output enough torque to reposition the transducer and housing quickly in a variety of current conditions, while maintaining a low weight and small profile in order minimize effects on the vehicle movement. The mount also needed to be waterproofed.

In order to quantify the torque requirements of the tilt actuator, an estimate was made of drag on the transducer and housing. The resulting torque was calculated

according to the following Eq. 2.3.

$$T = l\frac{1}{2}\rho_w C_D U^2 A_f \tag{2.3}$$

where l is the separation between the center of drag and the tilt axis, C_D is the drag coefficient for a cylindrical body in axial flow with a rounded face, U is the vehicle speed and A_f is the frontal area of the transducer/housing assembly. For a cylindrical body with a rounded face and a $\frac{l}{d} \approx 1.5$, C_D can be approximated as 0.3 [27]. Assuming a separation of 0.15m and a frontal area of XXX^2, the resulting torque is $XXXX$.

Considering the time and resources need to develop a custom mount, it was preferable to pursue an off-the-shelf option. The pan/tilt mount that was ultimately selected was a Remote Ocean Systems Air-Filled Waterproof PT-10 FB. Each axis of this unit is capable of 13.56N m of torque and 360° of rotation with a maximum speed of 15°/s. This provides the mount with enough torque to maintain the transducer position in expected drag conditions. An integrated RS-485 interface allows the automated control of the axes speed through a variety of ASCII commands. Position feedback from an internal encoder is also provided by the interface. Using the speed control and feedback, a controller was developed to position the actuator. The controller development is discussed in Section 2.5.

2.3.3 Vehicle Integration

The integration of the ADCP and pan/tilt mount with the kayak involved securing the mount to the underside of the kayak and managing the cable connections between the ADCP, mount and kayak electronics. The fully mounted system is shown in Figure 2-7. An important aspect of the integration is the ability to quickly install and remove the sensor system so that the kayak can be easily reconfigured in the field. The pan/tilt mount is secured to the kayak using a mounting plate connected to the pan yoke and a set of 80/20 aluminum channels that are permanently mounted on the underside of the vehicle. These channels are shown in Figure 2-6.

Figure 2-6: Image of instrument mounting channels on the underside of a SCOUT kayak.

While the pan/tilt cabling is waterproof and can simply pass through the kayak hull port, the ADCP cables must be routed through a waterproof sheath so that they remain dry. This sheath takes the form of a clear plastic tube. One end of the tube is hose-clamped and sealed with adhesive to the transducer housing port, while the other end passes through the hull port and into the vehicle. Because there is little slack in the cabling, software limits are placed on the pan movement so that the cables are not strained.

Figure 2-7: Reorienting ADCP assembly mounted underneath a SCOUT kayak.

2.4 Electrical System

Both the ADCP and pan/tilt mount draw their power from battery that serves as the vehicle power supply. In the case of the ADCP, 12V power is needed and is obtained from the vehicle sensor box. The pan/tilt mount operates off of 24V, drawn directly from the vehicle battery. Each axis draws a maximum of 750mA under full load and less than 100mA while at rest with no braking. Both devices communicate with the vehicle computer with ASCII serial interfaces using serial to USB converters.

2.5 Pan/Tilt MOOS Driver

The control of the pan/tilt mount is implemented as the MOOS application, iPanTilt. Integrated with iPanTilt is a digital PI controller that outputs speed commands and is used to control the position of each axis. The controller setpoints are set by posting to the MOOS variables `DESIRED_PAN` and `DESIRED_TILT`. These postings can be made by any MOOS application. iPanTilt publishes the following MOOS variables: `CURRENT_-`

PAN, CURRENT_TILT, and ROS_SET. These variables notify the MOOSDB of the current pan/tilt position and whether the actuation has reached its setpoint.

A PI controller was selected for its ease of implementation in software and robustness. To ensure that the controller ran a fixed frequency, it was implemented as a separate thread within iPanTilt. As with any controller design, considerations had to be made for limitations in the hardware and the nature of the controller execution. These considerations led to the implementation of effort limits, anti-windup and breaking within the control algorithm.

Each iteration of the position control algorithm follows the procedure summarized for one axis in Procedure 2.1. The algorithm begins by querying the position of each axis. This feedback is then used to calculate the current position error of each axis. The algorithm proceeds to calculate the control effort for each axis that will ultimately be sent to the mounts internal speed controllers.

Procedure 2.1 Produce control effort outputs for a pan or tilt axis

1: P_k = GetPositions()
2: $e_k = P_{desired} - P_k$
3: $u_k = floor(\left(K + \frac{KT}{T_i}\right) e_k + s_{k-1})$
4: **if** $|u_k| > u_{max}$ **then**
5: $\quad u_k = sgn(u_k)umax$
6: **end if**
7: **if** $u_k == 0$ **then**
8: $\quad Brake$ = on
9: **else**
10: $\quad Brake$ = off
11: **end if**
12: **Output:** u_k
13: **Output:** $Break$
14: $s_k = s_{k-1} + \frac{K}{T_i} e_k$
15: **if** $|s_k| > antiwindup$ **then**
16: $\quad s_k = sign(s_k)antiwindup$
17: **end if**

In a digital PI controller,the calculation of the control effort, u_k, at iteration k is based on the current error, e_k and an integral term from the previous iteration, s_{k-1},

as shown in Eq. 2.4.

$$u_k = \left(K + \frac{KT}{T_i}\right) e_k + s_{k-1} \tag{2.4}$$

In the above equations the K, T_i and T constants represent the controller gain, integral time and controller sample time respectively. Each can be tuned individually to improve stability. Before the control efforts are output to the axes' speed controllers, they are bounded to ensure that they are within an acceptable input range. The efforts are then converted to ASCII speed commands and sent to mount's internal control system. In the event the either effort is 0, a braking command is sent rather than a speed command so that the actuators maintain their position in the presence of distrubances. This continues until a non-zero effort is produced.

The last steps of the algorithm involve maintaining the integral term for each axis and recording a loop timer. Integral term is calculated using a forward triangle method as shown in Eq. 2.5. Before the integral term is stored for the next iteration, anti-windup is implemented and the term is bounded according to preset limits. This ensures that the control efforts are not quickly saturated following a large setpoint change.

$$s_k = s_{k-1} + \frac{K}{T_i} e_k \tag{2.5}$$

The controller was tuned by adjusting the sample and integral time, gain and the anti-windup and saturation limits. The final control settings appear in Table 2.1 and the response of the tilt actuator to a 90° step input is shown Figure 2-8. A conservative 0.1s sample time was selected to ensure that the position controller exhibited slower dynamics than the internal speed controllers. This sample time also represents the shortest realistic update period for setpoints given the MOOS infrastructure.

Table 2.1: iPanTilt Control Parameters

Parameter	**Value**
T	0.1s
K	0.5
T_i	0.1s
u_{max}	30counts/s
Antiwindup	5counts/s

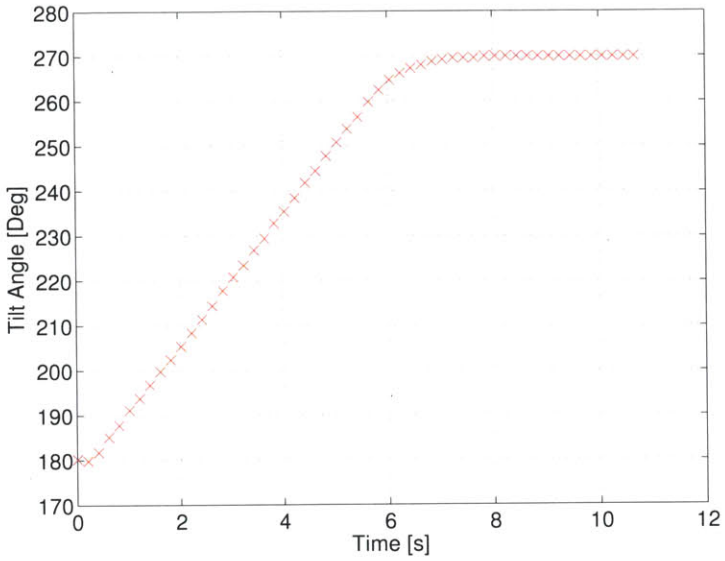

Figure 2-8: Response of the tilt actuator to a 90° set input. Position controller exhibits no overshoot, while slow ramp clearly demonstrates effects of control effort limits.

Initial efforts to select a proper gain and integral time proved difficult for a number of reasons. Backlash in the internal gearing and quantization of the feedback and effort caused dead-banding and resulted in steady-state error. Decreasing the integral time combats this effect by producing larger efforts over time for small offsets. However, this adjustment causes saturation when there is large error. Ultimately, more aggressive anti-windup and saturation limits fixed these issues, while sacrificing controller speed. This tradeoff is acceptable for the current iteration of this ADCP system, since trajectory following is not a goal. A higher performance controller may be necessary in future iterations to enable target tracking by the ADCP.

2.6 ADCP MOOS Driver

In order to fully integrate the ADCP system with MOOS and account for the complexity associated with the reorienting capabilities, a new MOOS software driver was developed for the ADCP. The application, iADCPInstrument, handles sensor configuration and control, coordination with iPanTilt, real-time data processing and data

publication. The general operation of this application is outlined in Figure 2-9.

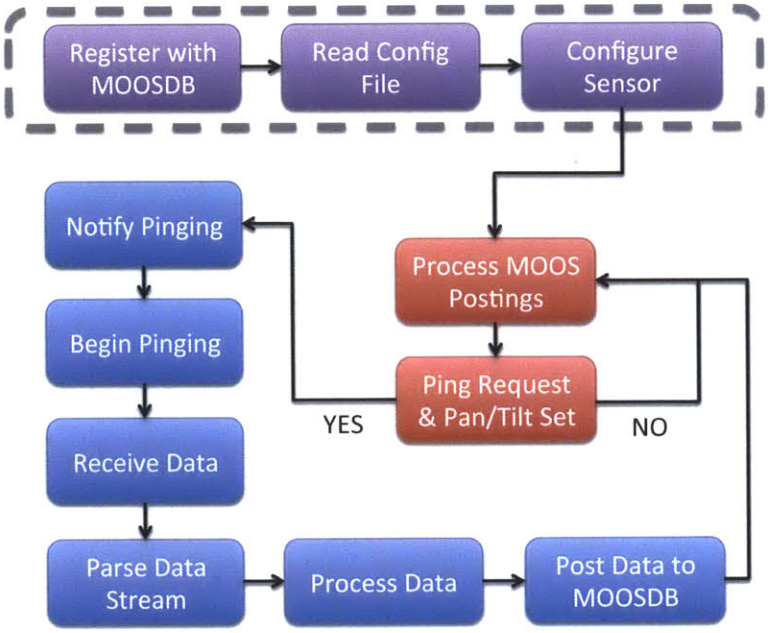

Figure 2-9: Outline of iADCPInstrument operation. Functions shown at the top are only called at the application's start.

2.6.1 Software Architecture

iADCPInstrument begins by connecting to the MOOSDB, reading from its configuration file and registering for variables. These processes are generally performed at the start of all MOOS applications. Configuration commands are then sent to the sensor. This concludes the software's startup routine.

The primary loop of iADCPInstrument begins by processing postings from other MOOS applications. These postings update iADCPInstrument with the vehicle's current position and attitude, the position and state of the pan/tilt mount and the desired mode of operation for the ADCP. At this point, if a ping-request posting has been received and iPanTilt has posted `ROS_SET = true`, indicating that the pan/tilt actuation is complete, the ADCP will begin a pinging sequence. Otherwise the loop restarts. At the start of the pinging sequence a notification, `ADCP_PINGING` is sent to the MOOSDB so that other applications are aware of the pinging operation. iPanTilt

subscribes to this notification and does not initiate actuation during the pinging process. Once the set number of pings have been completed and the ADCP has transmitted it's data to the vehicle's computer, data processing commences. The processed data is then logged in a binary format and sent to the MOOSDB so other applications can use the data.

2.6.2 Sensor Configuration and Control

Teledyne RDI Workhorse ADCPs utilize an ASCII interface that enables the configuration of the sensor and control of its operation. Through these commands, adjustments can be made to the ADCP's operation modes, the acoustic signals it produces and the types of data it stores. The frequency of pinging operations, length of pings and number of pings to average are just a few of many possible settings.

During the startup phase of iADCPInstrument, the desired settings for the sensor are translated into the appropriate ASCII commands and then relayed to the sensor. If the command is accepted by the sensor, a reply command is sent back to the vehicle computer and iADCPInstrument proceeds to the next command. Otherwise, the configuration sequence is restarted. The first command that is sent to the sensor is always a reset command to ensure that the sensor is in a known state.

Several of the desired settings can be user-defined through iADCPInstrument's configuration file. These settings define the number of pings to average, the ping period, the size of the measurement bin and the number of bins. The default values for these settings and a recommended range is shown in Table 2.2. This table also references several other user-defined parameters thats are set for iADCPInstrument within its configuration file. These parameters relate to the positioning of the ADCP transducer relative to the vehicle's origin and are used in data processing.

Once the instrument has been configured, control of the ADCP consists of sending commands to initiate pinging. After a command is sent to initiate a single measurement cycle, the loop waits to received the instrument's output and then begins to process the data. Pinging does not recommence until the data is processed.

Table 2.2: iADCPInstrument User-Defined Setting Parameters

Parameter	Description	Default	Range
PING_PERIOD	Length of each ping	50ms	10 – 100ms
PING_#	Number of pings averaged for each measurement	30	5 – 50
BIN_SIZE	Length of depth cell	200cm	50 – 200cm
BIN_NUMBER	Number of depth cells	10	5 – 40
ALIGNMENT	Alignment of third beam with vehicle's bow	0	N/A
LZ	Distance between tilt axis and vehicle origin	−40cm	N/A

2.6.3 Data Management

Unlike scalar temperature or salinity measurements, the vector data obtained from an ADCP is more complex and requires additional processing to make it usable. Since a large amount of data is collected during each measurement cycle, the ADCP outputs a binary data stream that must be parsed so that it can be interpreted and/or used by a human or software process. Within iADCPInstrument a parsing algorithm is implemented according to the syntax provided in [70]. The results of this algorithm are a set of fixed and variable leader data, and the data collected for each bin: velocity vectors, echo intensity, correlation magnitude and error velocities. This data is logged and stored in an object suitable for data processing. The results of each measurement cycle are then processed to transform the positions of the bins and the velocity measurements into the global reference frame.

The results of these calculations are stored using a portable protocol so that they can be easily accessed by other MOOS applications. This is achieved through the use of Google Protocol Buffers and its accompanying serialization libraries [26]. Protocol Buffers (protobuf) allow serialization of structured data independent of language and platform. A data structure is defined within a proto file from which complimentary source code is generated. Functions defined by this source code can then be utilized in C++, Java or python applications to store and serialize data. In the case of iADCPInstrument, the ADCP fixed and variable leader data is set in the protobuf data structure and then repeated fields are added for each bin measurement. Once all fields within the protobuf data structure are filled, the data it is serialized to a

binary string. This string is then published to the MOOSDB under the variable name ADCP_REPORT. More information about Protocol Buffers can be obtained at [26]. The proto file defining the data structured used for ADCP data appears in Appendix B.

2.6.4 Data Processing and Reference Frames

The ADCP is configured to output velocity measurements in the reference frame of the transducer. These measurements are transformed into the global frame and associated with positions within that frame. This transformation is done using knowledge about the vehicle's position, attitude and velocity and the relative position of the vehicle and instrument. Once the measurements have been transformed into the global frame, the contribution of the vehicle's velocity can be added to obtain the absolute measurements of the water velocity at the bin locations.

The measurement transformation and localization problem is defined in Figure 2-10 using three right-handed coordinate frames. The vehicle location is defined in a East, North, Up (ENU) global frame using GPS-derived latitude and longitude coordinates that are converted to a local geodetic centered at an arbitrary latitude and longitude.

The vehicle's frame, denoted by the superscript v, has its positive x-axis towards the bow and positive z-axis pointed down. The frame of the instrument, denoted by the superscript i, has its origin located in the vehicle frame at $(0, 0, L = 0.41\text{cm})$, at the base of the pan/tilt mount, centered on the mount's axes. Its positive x-axis points in the direction of the transducer's face. Its positive z-axis points down when the transducer is level with the horizon. Traditional roll, pitch, yaw terminology, (Θ, Ψ, Φ), is used when describing the rotation around the xyz axes respectively for both the vehicle and instrument frames. The instrument frame rotates about its origin with respect to the vehicle frame via the pan/tilt mount. Panning causes yaw and tilting causes pitch.

Velocity measurements output from the ADCP are given with respect to the instrument frame. For any given bin k, these measurements, (u_k^i, v_k^i, w_k^i) are localized in this frame according to Eq. 2.6 using knowledge of the bin spacing and the x and

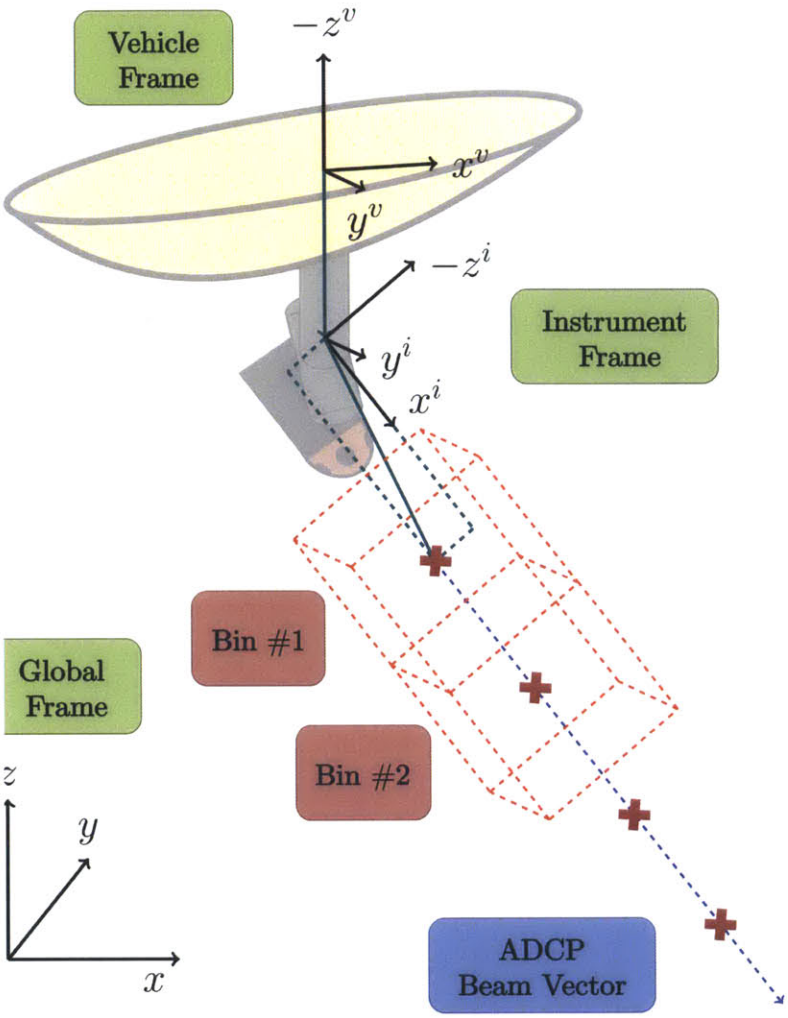

Figure 2-10: Diagram of ADCP measurement locations with respect to the instrument, vehicle and global frames.

z offsets between the frame origin and the transducer face.

$$P^i_{ADCP} = \begin{bmatrix} x^i \\ y^i \\ z^i \end{bmatrix} = \begin{bmatrix} x_{offset} + x_{bin\_1} + (k-1)\Delta_{bin} \\ 0 \\ z_{offset} \end{bmatrix} \tag{2.6}$$

Two sets of transformations are needed to calculated the global velocity measurements and positions in the ENU frame. Each set of measurements and positions are transformed first out of the instrument frame and into the vehicle frame and then out of the vehicle frame and into the global frame. These calculations are done using

combined rotation and translation matrices which produce a transformation matrix, an example of which is shown in Eq. 2.7.

$$T(a_1, a_2, a_3, b_x, b_y, b_z) = \begin{bmatrix} r_{11} & r_{12} & r_{13} & b_x \\ r_{21} & r_{22} & r_{23} & b_y \\ r_{31} & r_{32} & r_{33} & b_z \\ 0 & 0 & 0 & 1 \end{bmatrix} \tag{2.7}$$

The rotation components of the matrix, detonated by r_{xx}, are derived from the direction cosine matrix (DCM) for the given set of rotation angles, (a_1, a_2, a_3). The linear translations between the two frames make up the translation components, detonated by (b_x, b_y, b_z) . This matrix is 4x4 because it is essentially performing three operations: rotation, translation and scaling. Unity is chosen as the scaling quantity that appears in position $T_{4,4}$. A (y, x, z) DCM is used to produce the following translation matrix shown in Eq. 2.8 in which $C(x)$ and $S(x)$ are shorthand for $cos(x)$ and $sin(x)$ respectively.

$$^{yxz}T = \begin{bmatrix} C(\Psi)C(\Phi)+S(\Theta)S(\Psi)S(\Phi) & C(\Theta)S(\Phi) & -S(\Psi)C(\Phi)+S(\Theta)C(\Psi)S(\Phi) & b_x \\ -C(\Psi)S(\Phi)+S(\Theta)S(\Psi)C(\Phi) & C(\Theta)C(\Phi) & S(\Psi)S(\Phi)+S(\Theta)C(\Psi)C(\Phi) & b_y \\ S(\Psi)C(\Theta) & -S(\Theta) & C(\Theta)C(\Psi) & b_z \\ 0 & 0 & 0 & 1 \end{bmatrix} \tag{2.8}$$

Three such matrices are used to produce the final measurement positions according to Eq. 2.9,

$$\begin{bmatrix} P_{ADCP} \\ 1 \end{bmatrix} = T_3 T_2 T_1 \begin{bmatrix} P^i_{ADCP} \\ 1 \end{bmatrix} \tag{2.9}$$

where $T_1 = T(-\Psi^i, 0, -\Phi^i, 0, 0, L)$, $T_2 = T(-\Psi^v, -\Theta^v, -\Phi^v, 0, 0, 0)$ and $T_3 = T(-180, 0, 90, x_{veh}, y_{veh}, 0)$. These transformation matrices are calculated after every ADCP ping using feedback from the pan/tilt mount and the vehicle's internal compass and GPS.

The velocity measurements must account for the motion of the sensor. First the ADCP measurements, V^i_{ADCP}, are rotated into the velocity frame using the T_1 matrix with no translation components, shown here in Eq. 2.10.

$$\begin{bmatrix} V^v_{ADCP} \\ 1 \end{bmatrix} = T(-\Psi^i, 0, -\Phi^i, 0, 0, 0) \begin{bmatrix} V^i_{ADCP} \\ 1 \end{bmatrix} \tag{2.10}$$

The velocity of the instrument is the result of the vehicle's linear and angular velocity. Typical ADCP measurement cycles range in length from $1 - 5$s. In most circumstances, this is longer than vehicle's observed pitch and rolling periods. This makes it possible to neglect the angular velocity contributions, since they will be averaged out over the ADCP measurement cycle [28]. The final calculations of the absolute velocity measurements are done using modified versions of the T_2 and T_3 matrices that incorporate the vehicle's linear velocity derived from its heading, H, and speed, S . These calculations are shown in Eq. 2.11 where $T_4 = (-\Psi^v, -\Theta^v, -\Phi^v, Scos(H), Ssin(H), 0)$ and $T_5 = T(-180, 0, 90, 0, 0, 0)$.

$$\begin{bmatrix} V_{ADCP} \\ 1 \end{bmatrix} = T_5 T_4 \begin{bmatrix} V^v_{ADCP} \\ 1 \end{bmatrix} \tag{2.11}$$

Once the transformations have been completed, the global bin positions and velocity measurements are logged. If it is desired, the positions and measurements from the first ten bins can be broadcast to the whole MOOS community, enabling other applications to act on the data without having to process the protobuf structure that the ensemble data is reported in.

2.7 Noise and Localization Considerations

Random noise and issues inherent to the instrument and the process described above result in errors in the calculated global velocity measurements and their position. In this section, the larger sources of these errors are discussed and suggestions are given for limiting their effect when possible.

According to RDI's ADCP documentation, [28], the ADCP measurements are subject to both long-term bias error and short-term random error. The long-term bias error of the ADCP is typically between $10 - 20$cm/s and cannot be reduced. Random error results from internal factors such as the the ping length and external

factors such as turbulence and ADCP movement. This error can be decreased by averaging multiple pings during a cycle. Given sufficient averaging, this error can be brought below the long term bias. Both of these errors are most likely increased due to a non-vertical orientation of the sensor and failure of the current homogeneity assumptions discussed in Section 2.1 . Further analysis may be able to account for the additional error caused by horizontal orientations, but it is beyond the scope of this thesis.

The coordinate frame transformation calculations performed in iADCPInstrument are also subject to error. These calculations relay on having up-to-date and accurate measurements of the vehicle's position and attitude. Depending on the sensors that are used for the position and attitude measurements, the random error inherent to them can vary. Preliminary tests of this system made use of a 5m accuracy GPS and a OceanServer OS5000 compass with 1° accuracy on pitch and roll [54]. In addition to position measurements, GPS also provides heading and speed information. These are both relatively low accuracy units and thus result in larger errors in the coordinate transformations. Future tests will employ a OXTS Intertial+ GPS unit with an integrated Inertial Measurement Unit [57]. This system employs complex filtering and estimation algorithms for more accurate positioning and attitude information. With this unit 0.4m position accuracy, 5cm/s velocity accuracy and 0.2° attitude accuracy will be achievable.

Synchronization of the instrument's position and attitude with the velocity measurements is not fully achievable due to the non-zero length of the measurement cycle. Position and attitude measurements are recorded from sensors before a cycle beings. In data processing these old measurements are then used to produce the velocity measurements and positions. If the vehicle's state changes significantly during a cycle, the coordinate transformation calculations will produced incorrect results. Shortening cycles can limit this effect, but this results in larger random error in the velocity measurements. Future work may involve pairing longer cycles with state estimation to lower these types of errors.

In summary, the current implementation of this system is not ideal for obtaining

velocity measurements requiring less than 30cm/s precision. Future work will improve upon this in some areas, but the system is limited by the nature of the ADCP hardware. Despite this disadvantage, the current version of the system produces successful results, as shown in the next section.

2.8 Results

Preliminary tests of this system were performed at an industrial thermal and effluent jet. Wake detection experiments were also completed using a motor boat as a wake generator. Results of these tests are reported and discussed in this section.

2.8.1 Surface Velocity Measurements at a Thermal and Effluent Jet

The system was deployed on a SCOUT kayak at a thermal and effluent jet produced by a power plant cooling outfall in Singapore. The system was configured to record surface velocity measurements using a variety of pan positions and no tilt. The measurement cycle was set to 30, 10ms pings with a depth cell size of 0.5m. These settings were selected in an attempt to minimize the random noise measured by the ADCP. Bin number ranged from 5-40 bins. The vehicle conducted several transections of the jet and surveyed along the jets trajectory. The maximum speed of the vehicle during the survey was 1.6m/s.

Processing of the raw ADCP data was conducted post-experiment since online processing was not implemented at the time of the tests. A two-dimensional representation of the transformed velocity vectors is shown in Figure 2-11. The vector direction at each measurement location is indicated by an arrow. The length, width and color of each arrow correspond to the velocity magnitude in m/s. The GPS logs of the vehicle path are shown with white markers. The more simplified two-dimensional display of the three-dimensional data is achieved by representing all vector positions on the free surface and neglecting the vertical velocity components. Since all

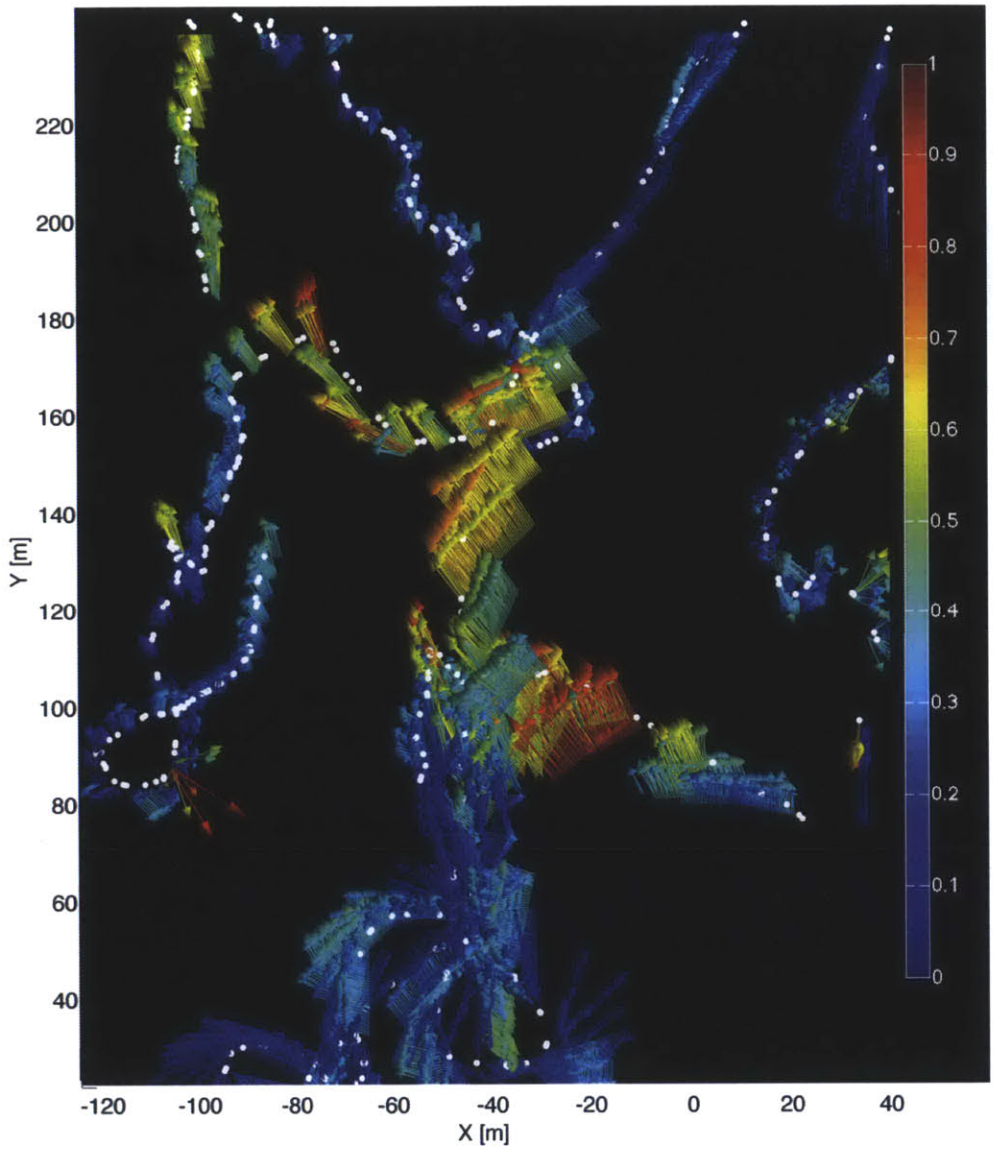

Figure 2-11: Two-dimensional surface velocity field measured by the horizontally oriented ADCP at a thermal and effluent jet. Vector direction at each measurement position is shown with an arrow. Arrow length, width and color indicate velocity magnitude in m/s. White markers show vehicle positions.

measurements were localized within 1m of the free surface and the vertical velocity components were relatively small, these simplifications are reasonable tradeoffs to improve the clarity of representation.

The industrial outfall is approximately located at the origin in Figure 2-11. This outfall produces a high velocity jet that extends into the NW corner of the plot. From the ADCP data, we see in the central region of the plot, areas of high velocity magni-

tude between 0.5−1.0m/s. These vectors are oriented towards the NNW and are found up to 220m from the outfall. In these regions the ADCP was able to obtain consistent measurements of magnitude and direction independent of the vehicle's heading and the ADCP pan position. This suggests that the coordinate transformation procedure is implemented correctly. Outside of these regions the measured magnitude decreases to $0.0 - 0.4$m/s. The non-uniform current direction and magnitude throughout the measurements is attributed to turbulence and vortical structures in the flow as well as the high noise levels discussed in Section 2.7. Issues also arose during the experiment due to drag induced by the ADCP. This drag decreased the vehicle's ability to track trajectories when transecting the jet.

Since the data is sparse and scattered, interpolation can be used to produce a more complete image of the the flow fields. Such a representation is shown in Figure 2-12. This figure was produced by separately interpolating the horizontal and vertical velocity vectors on a mesh using a natural nearest neighbor Delaunay triangulation interpolation provided in MATLAB®. Arrows are then produced at these mesh points and sized and colored based on the current magnitude calculated from the interpolated vectors. This view further establishes the jet-like flow structure with transverse spreading and centerline decay.

The results of this experiment demonstrate that this system is able to increase the amount of surface velocity measurements that can be obtain compared to a vertically oriented ADCP. This allows for less sparse data sets, which are useful for modeling and parameter estimation. Future experiments at thermal and effluent jets will attempt to station-keep the vehicle and dynamically reorient the ADCP to measure the three-dimensional flow field. Online estimation will also be implemented so that the vehicle can be directed to areas with high uncertainty in the velocity field.

2.8.2 Motor Boat Wake Detection

In order to test the wake detection capabilities of the system, an experiment was conducted with a SCOUT kayak and a pleasure craft type motor boat. The experiment was conducted in calm waters in the Johor Strait of Singapore. During the

experiment the motor boat was directed to pass across the kayak's bow at a moderate speed, so that a wake would be produced within the detectable range of the ADCP. The pan/tilt mount were oriented horizontal and pointed towards the bow of the kayak. The measurement cycle was set to 5, 10ms pings so that several ping cycles could be made before the wake diminished. A small depth cell size of 0.1m was

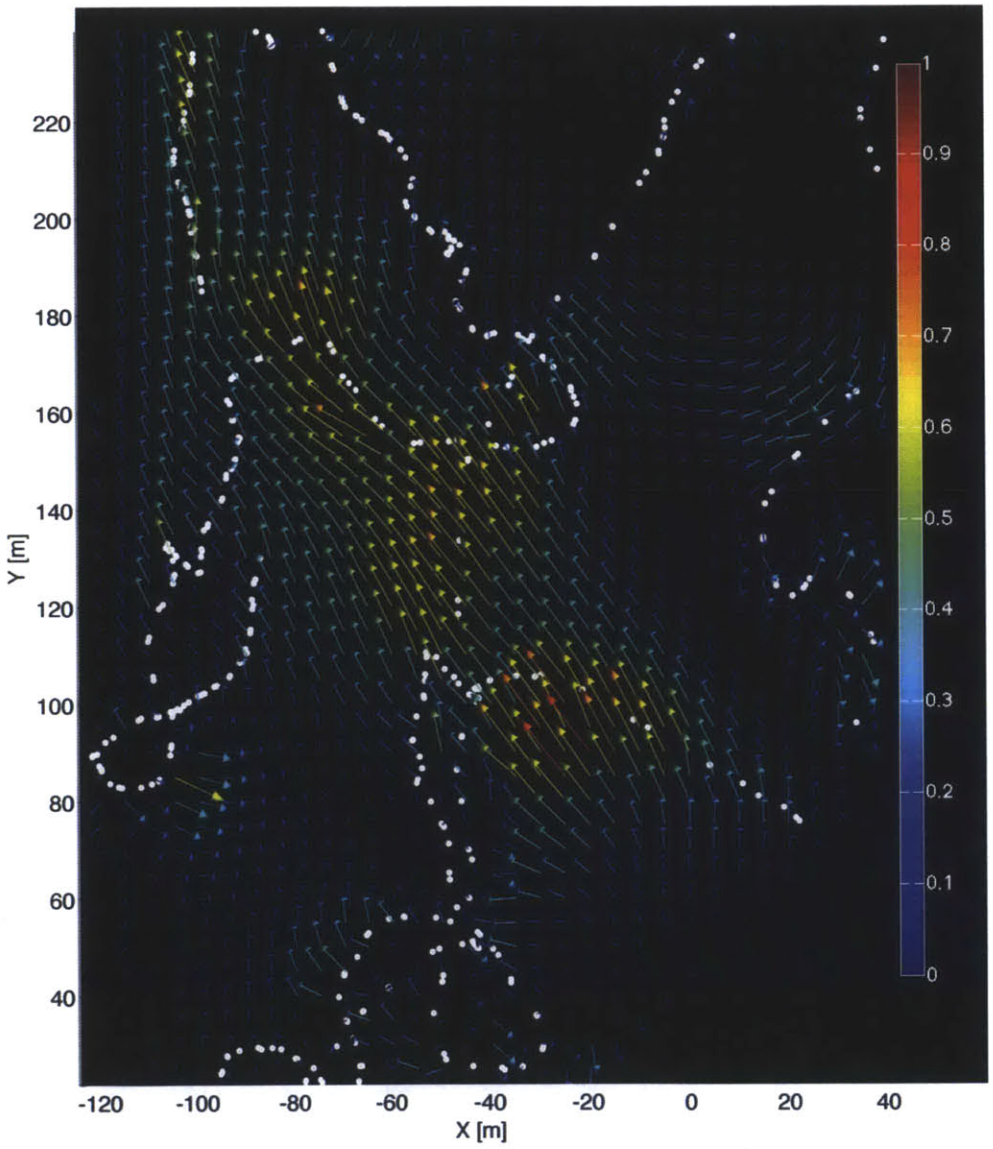

Figure 2-12: Interpolated two-dimensional surface velocity field at a thermal and effluent jet. ADCP measurements are interpolated to a mesh using Delaunay triangulation interpolation. Vector direction at each position is shown with an arrow. Arrow length, width and color indicate velocity magnitude in m/s. White markers show vehicle positions.

used with a bin count of 40 so that measurements could be taken across the width of the wake.

ADCP measurements were processed in real-time and posted to the MOOSDB. The results shown here are taken from logs of these processed measurements. Current direction was shown to be inconsistent near the wake, most likely due to noise from the turbulence, small depth cell size and bubbles in the wake. For this reason, a magnitude plot is used to display the velocity data in Figure 2-13. Current magnitude is plotted verses time and distance from the instrument.

During the trial shown here the boat makes two passes at approximately $t = 105$s and $t = 135$s. Due to the wake disturbance, the stationary vehicle's yaw angle varied from $35 - 60°$. Leading up to the first pass the current magnitude increases at the farthest bins reaching a peak at 20.3m from the ADCP at $t = 111$s with a maximum current of 1.63m/s. The current then settles to some extent before the second pass. The peak caused by the second pass occurs at 21.3m from the ADCP at $t = 152$s with a maximum current of 1.43m/s.

In the regions of the wake the instrument measures large magnitude currents that have inconstant direction due to noise. It is still not apparent if the higher observed magnitudes are due to actual doppler measurements of the current speed or if the effects of bubbles and turbulence cause a high magnitude bias error in the reported measurements. This ambiguity does not necessarily hamper the usefulness of the system for wake detection. Assuming the system is deployed in a calm environment, these findings suggest that wakes can produce a distinct ADCP signature and could be detected by a real-time algorithm to enable tracking.

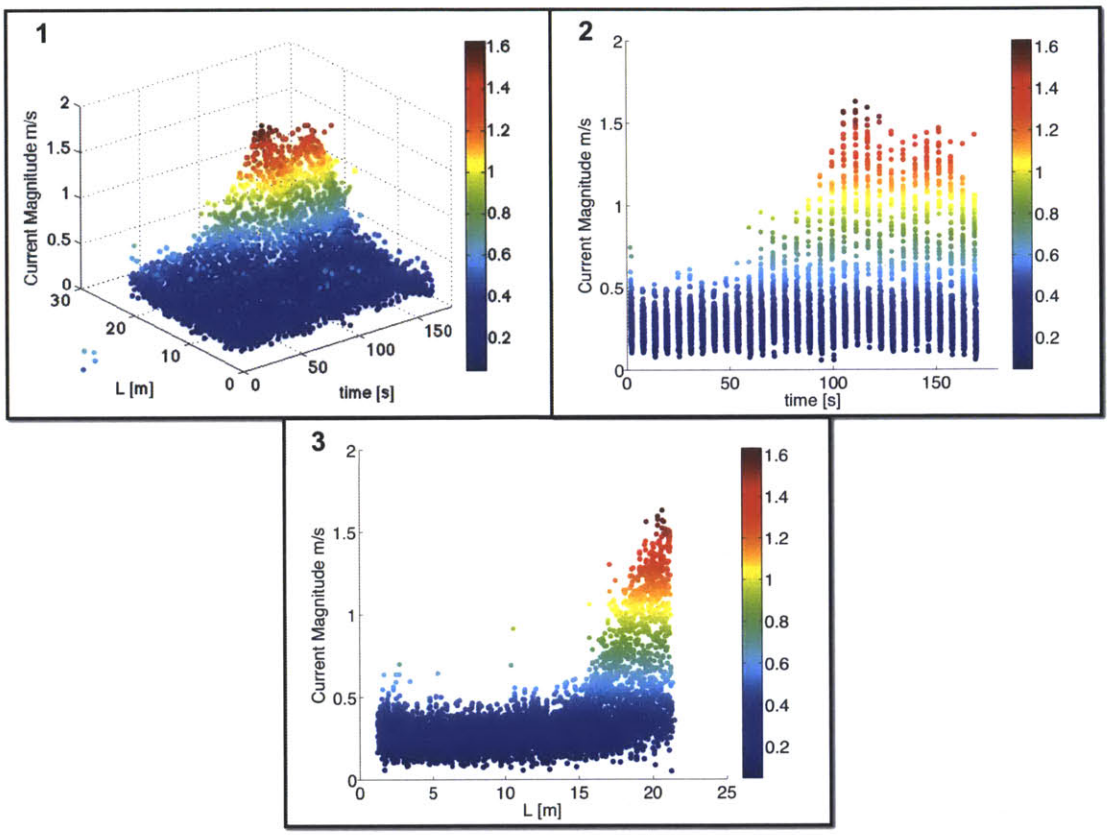

Figure 2-13: Measured current magnitude plots verses time and distance from instrument for wake detection experiment. Sensor is oriented horizontally and towards vehicle bow. Boat passes infront of vehicle twice. Data gathered using measurement cycles with 5, 10ms pings and 40, 0.1m depth cells. Plot 1: Isometric view of magnitude plot. Plot 2: Time verses magnitude. Plot 3: Distance from instrument verses magnitude.

Chapter 3

Thermal and Effluent Jet and Plume Modeling

This chapter presents a two-dimensional model of a thermal and effluent surface jet and plume that is integrated into MOOS-IvP. This integration is used to make a configurable simulation environment that can be used for developing autonomous sampling strategies. The model predicts values of the velocity, temperature and salinity fields produced by a jet based on the outfall parameters, ambient conditions and empirical constants. During the development of the model, the primary goals were the reproduction of a thermal and effluent jet and plume's macro features so that it can be used to simulate the sampling by an ASV equipped with a CTD sensor or ADCP. For this reason a two-dimensional surface model is used that does not specifically account for buoyancy effects and incorporates ample simplifications for crossflow. Parameter estimation is applied to the model for the purpose of fitting historic measurements. Online estimation using in-situ sampling is also developed to aid in autonomy operations.

The chapter begins by briefly summarizing current horizontal buoyant jet modeling techniques and demonstrating why a new model is needed for the purposes of this investigation. Dimensional analysis is then applied to a round jet model flow in Section 3.2. The empirical laws that have been established for this flow are discussed. This analysis is then extended to three-dimensional flows in Section 3.3 and consid-

erations are made for buoyancy, confinement and crossflow. Section 3.4 describes the assumptions and laws that define the model and its implementation. In Section 3.5 a brief summary of parameter estimation techniques is then provided before demonstrating the application of one such technique, simulated annealing, to the model. Section 3.6 outlines the software architecture that supports the integration of the model and online parameter estimation into MOOS-IvP. A list of symbols used in the model is found at the beginning of the thesis.

3.1 Previous Horizontal Buoyant Jet Modeling Efforts

The thermal and effluent jets of interest to this thesis are classified as horizontal buoyant jets. Most horizontal buoyant jet modeling relies on a combination of flow classification and dimensional analysis [36] that is then applied to integral modeling [49, 35, 34] or Lagrangian modeling [24, 44]. These methods are widely used to predict the flow characteristics of industrial outfalls to aid in their design and evaluate their environmental impact [36].

Due to the variety of flow categories that exist for horizontal buoyant jets, these methods either rely on expert classification systems, as in [36], or are directed to a specific category. Both approaches rely on previous knowledge of the source geometry, flow parameters and ambient conditions. In contrast, environmental models incorporated in adaptive sensing approaches must be general enough to apply to a wide variety of conditions. Inversion techniques are often applied to environmental models so that measurements can be used to determine model parameters [9, 20]. For these reasons, current horizontal jet models are not well suited to the autonomy planning and adaptive sampling efforts described in these thesis. Instead a generalized model based on empirical laws and dimensional analysis is developed.

3.2 Round Jet Model Flow

Round jet model flows are useful tools for better understanding horizontal buoyant jets. These flows can be described as fluid entering an infinite, ambient environment without gravity from a submerged source with round geometry. Round jet flows are characterized as self-similar flows with respect to the downstream distance from the source [12]. Geometrically speaking, this characterization means that the shape of these flows are identical across two cross-sections of the jet centerlines and differ only in a matter of scaling based on the conditions at the jet centerline.

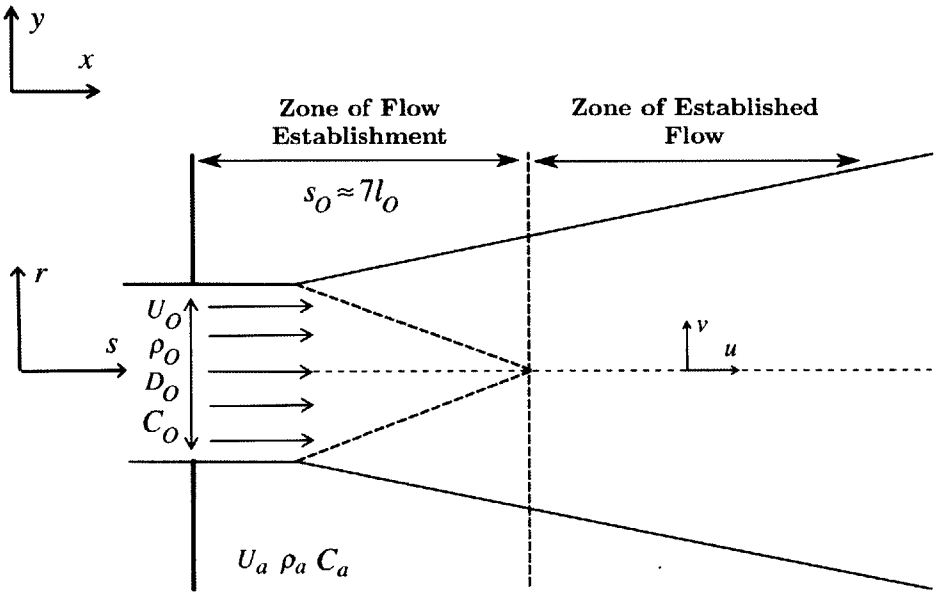

Figure 3-1: Diagram of Round Jet Model

The round jet is defined by the geometry at the source, the source conditions and the ambient conditions according to Figure 3-1. The jet is generated from a round source of diameter, D_O, that outputs fluid with velocity, U_O, density, ρ_O and concentration, C_O. The concentration can be considered as any scalar quantity in excess of the ambient environment. Since multiple concentration profiles can be considered, it is convenient to represent each jet concentration or axial velocity field α_i as a non-dimensionalized excess quantity, $E_i(s,r)$, as described in Eq. 3.1. For the round jet model flow, the ambient field is assumed to be stagnant and pure, so

$\alpha_{ia} = 0$.

$$E_i(s,r) = \frac{\alpha_i(s,r) - \alpha_{ia}}{\alpha_{iO} - \alpha_{ia}} = \frac{\alpha_i(s,r)}{\alpha_{iO}} \tag{3.1}$$

The source volume flux, Q_O, and the source momentum flux, M_O, characterize the flow. These parameters are defined in Eq. 3.2-3.3.

$$Q_O = \frac{U_O \pi {D_O}^2}{4} \tag{3.2}$$

$$M_O = Q_O U_O \rho_O \tag{3.3}$$

Using Q_O and the specific source momentum flux,M_O/ρ_O the development length scale is defined according to Eq. 3.4. This length scale determines the length of the zone of flow establishment.

$$l_O = Q_O \left(\frac{M_O}{\rho_O}\right)^{-1/2} = \frac{\sqrt{\pi}}{2} D \approx 0.89 D_O \tag{3.4}$$

The zone of flow establishment (ZFE) refers to one of the two regions of jet development. In the ZFE, the jet has a potential core with constant velocity and concentration. The core is surrounded by a mixing layer [45]. Experiments have determined that for round jets the length of this zone is typically near $7l_O$ or $6.2D_O$. The other development zone is the zone of established flow (ZEF).

In the ZEF the excess profiles are self-similar and take on a Gaussian-like structure. The peak of these profiles occurs at the jet centerline. This peak, referred to as $\tilde{E}_i(s) = E_i(s,0)$, has been confirmed experimentally to vary linearly with s according to Eq. 3.5 [3, 60, 15].

$$\tilde{E}_i(s) = \frac{s_O}{s} \tag{3.5}$$

If a Gaussian is used to define the profiles, the ZEF jet fields then are describe by Eq. 3.6.

$$E_i(s,r) = \frac{s_O}{s} exp\left[-\left(\frac{r}{B_i s}\right)^2\right] \tag{3.6}$$

Here B_i refers to the field specific spreading constant. For the axial velocity, experiments have shown that $B_i \approx 0.11$ [45]. Experiments with ink tracers as a scaler concentration field have resulted in $B_i \approx 0.13$ [45].

The round jet's radial velocity field is defined by applying conservation of mass equation to a cylindrical control volume of radius R. This results in a profile with a maximum radial velocity that is $\frac{1}{40}U_{max}$ [59]. It is important to note that radial velocity profile takes on negative values when $r < 0.11s$. This characteristic of the radial profile is known as entrainment and is important to the mixing capacity of the jet [45]. However, since magnitude of these velocities is relatively small compared to axial field, it is not necessary to consider them for the purposes of the thermal and effluent jet-plume model.

3.3 Complex Jet Effects and Experimental Investigations

The round jet model is used as a framework for studying jets that are affected by buoyancy, confinement and crossflow. These are considered so that reasonable simplifications and generalizations can be made for the thermal and effluent jet-plume model.

3.3.1 Buoyancy and Confinement Effects

Buoyant jets are produced when the density of the source fluid, ρ_O, is less than the ambient density ρ_a. This can be cause by a temperature excess or lower salinity. Depending on the source's relative position to the free surface, buoyant jets can exhibit vertically curved centerline trajectories [53] and can have altered spreading behavior [10].

Buoyant jets are described as having an source buoyancy flux, B_O. The source

buoyancy flux is related to the effective gravity of the source fluid, $g'_O = \frac{\rho_a - \rho_O}{\rho_a} g$, according to Eq. 3.7. Using the source buoyancy flux, the buoyancy length scale, l_B, is defined in Eq. 3.8, where F'_O is the jet's densimetric Froude number.

$$B_O = \frac{U_O \pi {D_O}^2}{4} g'_O \tag{3.7}$$

$$l_B = \left(\frac{M_O}{\rho_O}\right)^{3/4} B_O^{-1/2} = U_O \left(\frac{D\sqrt{\pi}}{2g}\right)^{1/2} = l_O F'_O \tag{3.8}$$

The buoyancy length scale measures the relative strength of the momentum flux and buoyancy flux. At $10 - 15 l_B$ from the source, buoyancy effects become dominant and vertical entrainment stops [10]. If the jet source depth Z_O is sufficiently large compared D_O, a curved centerline trajectory in the ZX plane is observed. In [53] horizontal heated jets of varying $R_O = l_O/l_B$ were produced in tank experiments. XZ centerline trajectories were tracked using image processing. A trajectory plot from [53] is shown in Figure 3-2. The general trend of these trajectories is that for smaller l_O/l_B the normalized trajectory is more horizontal.

Shallow water confinement effects have been the focus of a number of investigations [6, 65, 68, 14]. The general consensus of these investigations is that shallow water tends to decrease entrainment and centerline decay. As the jet approaches the free surface, vertical entrainment rapidly falls and the jet spreads horizontally.

The jets of interest to this thesis are subject to vertical confinement as defined in [16] for water depths of H according to 3.9.

$$\frac{H}{l_B} < 0.5 \tag{3.9}$$

The power plant outfalls are located in water $H < 10$m. Using historical measurements and some reasonable assumptions about the outfalls, it is possible to calculate approximate values of g'_O, l_O and l_B for these jets. These jets exhibit a weak effective gravity of $< 0.01\text{m/s}^2$. If a source diameter of 2m is assumed with a 3m/s outfall

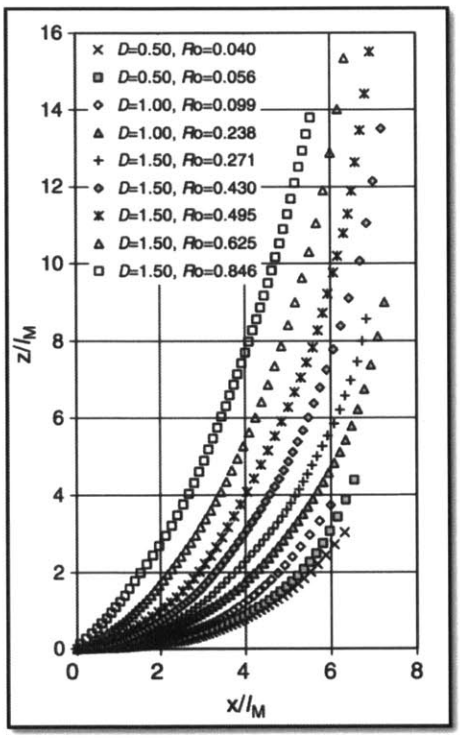

Figure 3-2: XZ centerline normalized trajectories for heated buoyant horizontal jets with varying $R_O = l_O/l_B$ taken from [53]. L_m is used for l_B. Smaller l_O/l_B results in diminished buoyancy effects and more horizontal trajectory.

velocity, $l_O = 1.78$m, $l_B = 0.4$m and $H/l_B < 0.04$. The depth to buoyancy length scale ratio suggests that these jets are indeed subject to confinement effects. Using the buoyancy and discharge length scales it is possible to place the jets among the XZ trajectories shown in Figure 3-2. Based on this plot, these jets would be most similar to the trajectory shown for $R_O = 0.04$ and would exhibit mostly horizontal XZ trajectories.

Together the findings reported by buoyancy and confinement jet investigations suggest that the jets of interests exhibit mostly horizontal behavior and that buoyancy does not need to be directly considered for a two-dimensional surface model. However, since buoyancy and confinement have been shown to affect jet decay and spreading, the model needs to account these changes in structure. This is implemented in the model by introducing independent decay and spreading parameters. These parameters are discussed further in Section 3.4.1.

3.3.2 Crossflow

Rather than entering a stagnant fluid, the jets of interest are subject to crossflow due to tidal currents. Crossflow is defined as the component of the ambient water velocity that is perpendicular to jet's initial direction. Depth average current magnitudes and directions have been measured using a bottom mounted ADCP approximately 450m downstream of a jet site. Magnitudes range between $2.5 - 12$cm/s. Current direction follows an approximately 12h cycle over which time 180° of shift is observed. These measurements do not necessarily reflect the crossflow that the outfall was subject to due to the large downstream distance between the outfall and ADCP.

The introduction of a crossflow gives rise to a new length scale. The crossflow length scale, l_C, is defined using the crossflow magnitude, u_a, according to Eq. 3.10.

$$l_C = \frac{M_O^{1/2}}{{\rho_O}^{1/2} U_C} = \frac{l_O U_O}{U_C} \tag{3.10}$$

I first consider a jet under a steady, non-reversing crossflow. Under this assumption, the crossflow length scale governs the length of the horizontal distance from source at which point the crossflow significantly impacts the jet trajectory. Outside of the jet's establishment zone, the jet loses Q_O dependence and is governed solely by the M_O, u_a and x [10]. This relationship makes it possible to characterize the jet structure by one parameter, x/l_C, in the absence of buoyancy. This parameter can then be used to develop a centerline trajectory law. If the jet is also subject to buoyancy, the effects can be characterized by l_B/l_C. Theses added effects complicate the development of a trajectory law as described below.

In [10] extensive tank experiments were performed on jets subjected to both steady and reversing crossflow and buoyancy due to thermal excess at the source. Measurements were taken on the surface in the far field. For the steady experiments $0.45 < l_B/l_C < 1.32$. This buoyancy and crossflow length scale range reflects a large portion of the range calculated for the jet sites based on the ADCP measurements discussed above and the assumptions discussed earlier: $0.25 < l_B/l_C < 1.49$. Center-

line trajectories, defined by the local jet are cartesian coordinates, tended to follow the 1/3 trajectory law established in [73], shown here in Eq. 3.11.

$$\frac{x'}{l_C} = C\left(\frac{y'}{l_C}\right)^{1/3} \tag{3.11}$$

Values for the coefficient C varied between $2 - 9.5$ with larger values corresponding to less bending. Larger values of C were loosley correlated to smaller values of l_B/l_C, indicating stronger dependence on buoyancy verses crossflow. In general, these experiments suggest that an accurate prediction of C is not obtainable and that it is influences by a variety of factors such as wall and bottom effects.

Maximum non-dimensionalized thermal excess, $\tilde{E}_T$, was also investigated in these experiments. Results showed that rather than varying linearly with s, maximum temperatures decreased at a slower rate, with larger values of l_B/l_C produced the slowest rates.

In [10] reversing crossflow experiments were also conducted. These experiments subjected buoyant jets to semidiurnal tides with a 12.4h cycle. The results of these experiments relate primarily to the horizontal extent of a plume produced by a jet. Larger extends were observed for longer cycles and stronger crossflows.

3.4 Thermal and Effluent Jet and Plume Model

The experimental results discussed in Section 3.3 demonstrate the difficulties inherent in modeling jets subjected to buoyancy, confinement and crossflow. Rather than attempt to fully accounts for these effects, the jet simulation model described here incorporates some of the empirical laws used in these investigations. Buoyancy is not directly considered due to confinement and the two-dimensional nature of the model. Reversing crossflow is not incorporated due to the complexity of its effects and since the model's focus is on the near field where ASV measurements are primarily taken. Instead a steady crossflow trajectory law is used, making it possible to test the robustness of sampling strategies to trajectory changes by altering an empirical

trajectory coefficient. In order to account for the changes in decay and spreading brought on by the buoyancy, confinement and crossflow effects, spreading and decay coefficients are also used as independent model parameters.

3.4.1 Model Laws

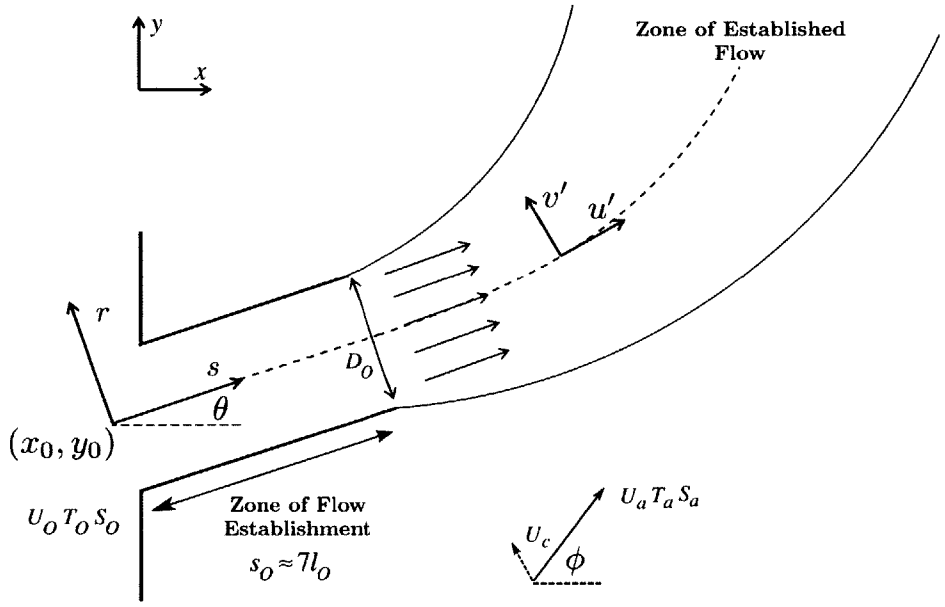

Figure 3-3: Diagram of Curved Jet Model

For the purpose of simulations only the axial velocity, u', temperature, T, and salinity, S, fields are modeled, although the model can be extended to include any scalar jet field. A diagram of this model is shown in Figure 3-3. The jet is defined along an axis rotated by angle θ at the virtual origin (X_O, Y_O). Distance along the jet's centerline is represented by s and distance from the centerline is represented by r. At the source the fluid has velocity, temperature and salinity represented by (U_O, T_O, S_O). The source has diameter D_O. The ambient current, temperature and salinity of the ambient environment is represented by (U_a, T_a, S_a). The ambient current has direction ϕ. The crossflow current U_C is defined according to Eq. 3.12. During calculations of $E_i(s, r)$, the ambient velocity, U_a is always set to zero. This initialization is done because the ambient current must be added to the jet velocity field through vector addition.

$$U_C = sin(\phi - \theta)U_a \tag{3.12}$$

Neglecting buoyancy, the discharge length scale and crossflow length scale are use in the model equations and are defined according to Eq. 3.4 and Eq. 3.8. Reflecting the round jet model, the ZFE defined as starting at $(s = 0, r = 0)$ and having width D_O and length $s_O = 7l_O$. To simplify the modeling, $\tilde{E}_i(s)$ is kept constant in the ZFE and equal to the source conditions.

Outside of this region the centerline decay follows a power law. For each jet field the centerline value decays with increased s according to Eq. 3.13. The decay coefficient, N_i is specific to each field. For example, surface cooling can be simulated by setting temperature to decay more quickly than salinity. This coefficient also makes it possible to incorporate slowed decay effects due to confinement that were discussed in Section 3.3.1.

$$\tilde{E}_i(s) = \left(\frac{s_o}{s}\right)^{N_i} \tag{3.13}$$

A radial basis function known as a inverse multiquadric is used to approximate the self-similar field profiles [59]. This function produces the Gaussian-like profiles that are observed for the round jet. Using this function the expression for the jet fields is shown in Eq. 3.14. The field specific spreading coefficient, R_i, simulates different widths for the jet fields.

$$E_i(s, r) = \tilde{E}_i(s)\left(1 + R_i\left(\frac{r}{s}\right)^2\right)^{-2} \tag{3.14}$$

The jet trajectory is calculated using Eq. 3.11. As noted in Section 3.3.2, the trajectory coefficient, C, is related to the relative strength of buoyancy and crossflow. Smaller values near 2 produce straighter trajectories and correspond to stronger buoyancy forces. Larger values increase the trajectory's curve.

With the addition of the decay, spreading and trajectory coefficients, the indepen-

dent model parameters are as follows:

$$\begin{pmatrix} u' \\ T \\ S \end{pmatrix} = f\left(X_O, Y_O, \theta, \phi, D_O, U_O, U_C, T_O, T_a, S_O, S_a, N_i, R_i, C\right) \tag{3.15}$$

This set of parameters will be referred to as
$P = \{X_O, Y_O, \theta, \phi, D_O, U_O, U_C, T_O, T_a, S_O, S_a, N_i, R_i, C\}$.

3.4.2 Model Implementation

The model is implemented as both a straight jet with no trajectory law and a curved jet. Under the straight implementation the fields are explicitly defined at all positions locations. When the straight model is queried at position (x_p, y_p), the position is rotated into the jet frame according to Eq. 3.16-3.17. Negative s positions are filtered and placed at large distances from the jet so that the returned fields will be in the ambient.

$$s_p = cos(\theta)(x_p - X_O) + sin(\theta)(y_p - Y_O) \tag{3.16}$$

$$r_p = -sin(\theta)(x_p - X_O) + cos(\theta)(y_p - Y_O) \tag{3.17}$$

The fields are then calculated according to Eq. 3.13-3.14 and the constant ZFE condition. The axial velocity, u' is rotated into the global frame and added to the ambient current to produce the global velocity field, (u, v), according to Eq. 3.19-3.19. The global velocity, temperature and salinity, (u, v, T, S), is then reported. Before reporting it is possible to add Gaussian noise to each value to simulate measurements by real sensors.

$$u = cos(\theta)u' + cos(\phi)U_a \tag{3.18}$$

$$v = sin(\theta)u' + sin(\phi)U_a \tag{3.19}$$

The curved jet model does not benefit from being explicitly defined for all positions. Instead the jet fields are calculated at points defined along and across the trajectory curve that is computed in the rotated jet frame according to Eq. 3.11. This collection of points, P_m, and the velocity field is then rotated into the global frame. Querying the model at (x_p, y_p) is done through a crude interpolation of the values defined at P_m. This proximity search of P_m is performed until a point (x'_p, y'_p) within P_m is found that satisfies a distance threshold to (x_p, y_p). The field values at (x'_p, y'_p) are then reported. As in the straight model, Gaussian noise can be added to the reported values if desirable.

This implementation is computationally slow and less accurate compared to the straight jet. Increasing the density of P_m increases the interpolation accuracy by decreasing the space between points. This comes at a cost of model startup time because field calculations must be made at more locations. Query time also increases because of the increase in the size of P_m. Due to the computational cost of this implementation, it is not possible to perform parameter estimation using the full curved model. This is discussed additionally in Section 3.5.2.

3.5 Parameter Estimation

The thermal and effluent jet-plume model is fit to physical measurements of velocity, temperature and salinity fields at cooling outfalls. This is achieved through parameter estimation. A number of parameter estimation techniques exist. These include least-squares, Kalman filtering and its various extensions, genetic algorithms and simulated annealing. Of these, least-squares and Kalman filtering are well suited for low dimension, linear problems, but are not effective for higher-order, non-linear models such as the jet model. The unscented Kalman filter (UKF) [38] can be used to solve non-linear problems and does not require the calculation of a model's Jacobian, for which would be complicated for our model's equations. However, a UKF is unnecessarily complicated approach for the time invarient model presented here.

Genetic algorithms and simulated annealing both offer stochastic, heuristic approaches to parameter estimation and thus are well suited for highly non-linear problems. As it name suggests, genetic algorithms (GA) mimic the evolutionary process to generate optimal solutions to a cost function [23]. The computational implementation of GA parameter estimation can be rather complicated, requiring the creating and tracking of a variety of virtual representations of evolutionary constructs such as genes and generations. This makes it unsuited for integrating into the MOOS-IvP autonomy system and online implementation.

Simulated annealing (SA) parameter estimation is a stochastic search algorithm that attempts to optimally fit a model to measured data by randomly permuting model parameters across the parameter space [41, 17]. Solutions are accepted at each iteration with a probability that is a function of the change in a cost function and a global time-varying parameter known as the temperature. In addition to being well-suited to non-linear problems, SA parameter estimation can be easily implemented online. For these reasons it is used here to fit the model and is integrated into MOOS-IvP for online estimation.

3.5.1 Simulated Annealing

SA parameter estimation draws its name from annealing in metallurgy. Metallurgical annealing involves the controlled cooling of a material to decrease its defects by minimizing its thermodynamic free energy. This is reflected in SA through the decreased probability of accepting worse solutions as the global temperature parameter decreases. This aspect of SA allows the algorithm to explore the solution space while settling on a optimal or near optimal solution over time.

A basic SA algorithm is presented in Algorithm 3.1. At each iteration k of the SA algorithm a cost function, C_k, is computed from the a new solution, S_k. The cost function is computed based on the current measurement set, M_k and model predictions resulting from S_k. An annealing temperature, T_k, is also computed based on the current iteration setup and typically decreases at each step. Based on the change in cost function,$\Delta C_k = C_k - C_{k-1}$, and T_k, the acceptance probability, $P_k(\Delta C_k, T_k)$,

is calculated. The current solution is accepted with P_k. If $\Delta C_k < 0$, $P_k = 1$ and S_k is always accepted. Otherwise P_k is calculated according to some set function.

Procedure 3.1 SA algorithm to determine if a new solution, S_k, is accepted or rejected.

Compute: S_k
$C_k = f(M_k, S_k)$
$T_k = f(k)$
if $(C_k - C_{k-1}) < 0$ **then**
    $P_k = 1$
else
    $P_k = f(\Delta C_k, T_k)$
end if
$X \sim U[0, 1]$
if $X < P_k$ **then**
    Accept: S_k
else
    Reject: S_k
end if

Each solution is computed by randomly varying each of the model's parameters between the bounds set for each parameter. A least square cost function is used to fit the observed data. For each of the jet fields, n_i measurements exist at positions (x_{ij}, y_{ij}). At each of these locations a model prediction, $\alpha_i(x_{ij}, y_{i_j})$ is computed using the solution S. These predictions are used to calculate the root mean square error (RMSE), R_i, for each field. The total cost is the sum of each field's RMSE. By using the RMSE for each data type, the cost function is independent of observation count and source. This is summarized in Eq. 4.5-3.21.

$$R_i = \frac{1}{n_i} \sum_{j=1}^{n_i} \left(\alpha_i(x_{ij}, y_{ij}) - \alpha_{ij}^{obs} \right) \tag{3.20}$$

$$C = \sum_{i=1}^{3} R_i \tag{3.21}$$

The annealing temperature is calculated using a exponential decreasing function shown in Eq. 3.23. The number of cooling steps, c_s, can be adjusted to slow cooling. The acceptance probability is also determined using a decreasing exponential shown in

Eq. 3.23. The temperature constant, k_t, controls the affect of annealing temperature on the acceptance probability.

$$T_k = exp(-2\frac{k}{c_s}) \tag{3.22}$$

$$P_k = exp(-\frac{\Delta C_k}{k_t T_k}) \tag{3.23}$$

3.5.2 Model Fitting

Model fitting was performed using MATLAB's simulated annealing package. This package offers a similar implementation as described in Algorithm 3.1 while adding options for re-annealing and alternative cooling and probability functions. Re-annealing is the process of increasing the annealing temperature after a period of time so that local minimum are avoided. The parameter estimation was run using temperature and salinity data collected by a YSI sonde mounted on a SCOUT autonomous kayak on Jan. 7th, 2012 and July 14th, 2012 at Site 1. The kayak path followed a simple lawnmower pattern, which extended approximately 175m from the outfall.

As mentioned in Section 3.4.2 the implementation of the curved model is computational expensive. The computation time for the cost function of the curved model is $O(1\text{s})$ for typically sized measurement sets. This prohibits its use for model fitting. Instead the straight model for temperature and salinity is used with the parameters:

$$\hat{P} = \{X_O, Y_O, \theta, D_O, U_O, T_O, T_a, S_O, S_a, N_i, R_i\}$$

This tradeoff should not significantly impact the model fitting results. Most of the historic field data was gathered in weak ambient current conditions relatively close to the outfall, so the bending effects were minimal on the observed jet trajectory.

Bounds were selected for the estimation using knowledge of the jet location and measurements of the ambient conditions. Reasonable ranges for the source conditions bounds were based on the round jet model, results from [10] and a survey of some industrial outfall conditions. Initial selections were then adjusted after several test

rounds to loosen the more restrictive bounds. Final bounds are shown in Table 3.1 for Site 1. The initial solution is selected from the bound mid points.

Table 3.1: Bounds used for MATLAB simulated annealing straight model fit of temperature and salinity YSI data from Site 1.

	LB	**UB**
$\boldsymbol{X_O}$	200m	250m
$\boldsymbol{Y_O}$	-340m	-300m
$\boldsymbol{\theta}$	103°	143°
$\boldsymbol{D_O}$	1m	4m
$\boldsymbol{U_O}$	0.5m/s	2.0m/s
$\boldsymbol{T_O}$	$32°C$	$50°C$
$\boldsymbol{T_a}$	$28°C$	$31°C$
$\boldsymbol{S_O}$	$27ppt$	$32ppt$
$\boldsymbol{S_a}$	$24ppt$	$26ppt$
$\boldsymbol{N_T}$	0.05	1
$\boldsymbol{R_T}$	0.5	30
$\boldsymbol{N_S}$	0.05	1
$\boldsymbol{R_S}$	0.5	20

Using these bounds the estimation is performed five times on three sets of data from Site 1. One set is from Jan 7th, 2012, while the other two were taken 30min apart on July 14th, 2012. Results are shown in Table 3.2. The cost function calculations for the given solutions are shown in the top row. Figure 3-4 contains side by side plots of the observed and estimated temperature and salinity fields from the January set and one July set.

From the these results, several conclusions can be drawn about the jet model, estimation methodology and jet characteristics at Site 1. By comparing the side by views of the observed and estimated fields in Figure 3-4, it is seen that the estimation algorithm is able to accurately localize the jet in the near field and estimate spreading constants that produce comparable jet widths for both observed fields. Location, angle and ambient parameters are the most consistent between estimations on the same set. Other parameters demonstrate significant variability across estimations. These parameters are tied to the region of the jet where larger field gradients exists.

The straight trajectory model fails to reproduce the effects of the ambient current that are seen deflecting the farther extents of the observed jet fields to the top right

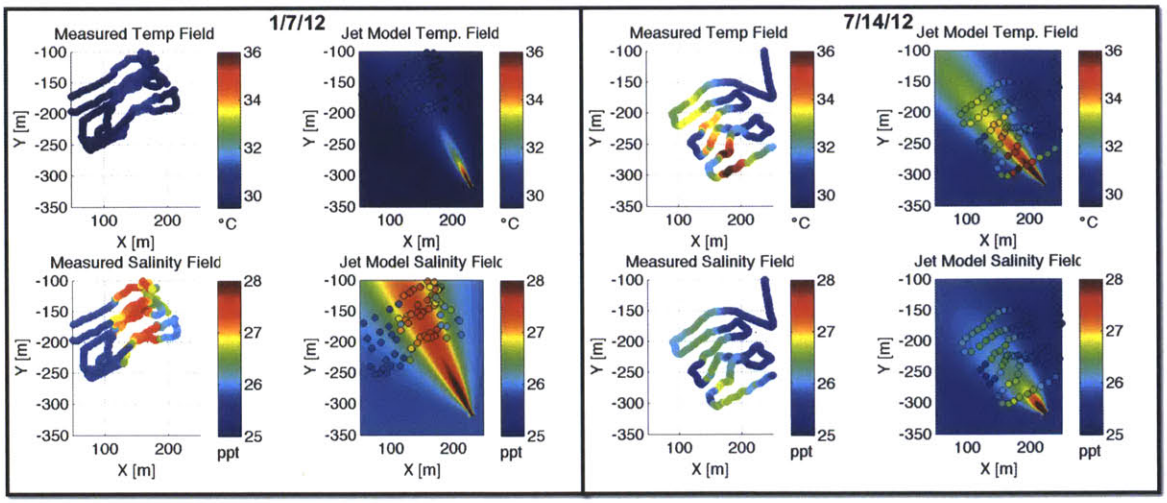

Figure 3-4: Observed (left) and estimated (right) temperature and salinity Fields for YSI data collected at Site 1 on Jan 7th, 2012 (left) and July 14th, 2012 (right). The Jan. model fit has a cost of 0.70 while the July fit has a cost of 1.11. Fits were made using parameters shown in Tabel 3.2 for Trial 2 from Set I and III.

of the estimation plots. Additionally, the observed fields appear to contain areas of non-uniform decay and spreading that the model does not account for. This is expected given the simplified scope of the model.

In the data from July 14th, a large span of heated and high salinity water can be seen near the outfall's north side. This could be due to reattachment, or supplementary outlets. These observations can not be accounted for by the model and tend to bias the estimates towards wider jet flows and high source temperatures and concentrations.

Across the three sets of estimation results there exists variation within the estimated parameters. The January estimation results include lower source temperatures, higher temperature decay and narrower temperature span than the July results. The salinity source, spreading and decay results do not appear to exhibit any correlation between sets. The January temperature results suggest that the cooling outfall was operating at a lower load at the time of the January sampling compared to July data.

One probably contribution to the variability in the estimation results is the quality of the data sets. The January set does not include any points within 100m of the outfall location. While July sets do include data closer to the outfall, they inade-

quately sample the jet boundaries as can be seen in the upper portions of the July measurement plots in Figure 3-4. These issues are the primary motivators for an adaptive sampling strategy. Such a strategy would allow for more extensive coverage of the jet and its boundaries.

Table 3.2: Bounds for MATLAB simulated annealing straight model fit of temperature and salinity data at Site 1 on Jan. 7th, 2011.

I: 1/7/12	**T1:** $C = 0.74$	**T2:** $C = 0.70$	**T3:** $C = 0.71$	**T4:** $C = 0.68$	**T5:** $C = 0.66$
X_O	222.0m	230.1m	226.7m	222.4m	222.8m
Y_O	−317.0m	−319.9m	−319.8m	−319.3m	−320.4m
θ	114.6°	116.9°	115.7°	115.7°	115.7°
D_O	2.1m	2.2m	1.2m	3.1m	2.4m
U_O	1.4m/s	1.0m/s	0.8m/s	0.8m/s	1.6m/s
T_O	34.6°C	43.0°C	41.9°C	43.1°C	38.7°C
T_a	29.5°C	29.4°C	29.3°C	29.4°C	29.4°C
S_O	31.5*ppt*	29.7*ppt*	32.0*ppt*	28.5*ppt*	30.8*ppt*
S_a	25.2*ppt*	25.8*ppt*	25.8*ppt*	25.8*ppt*	25.3*ppt*
N_T	0.45	0.82	0.62	0.88	0.63
R_T	21.2	12.7	18.3	13.3	15.8
N_S	0.32	0.31	0.35	0.19	0.34
R_S	8.7	9.6	13.6	9.7	4.6

II: 7/14/12	**T1:** $C = 1.28$	**T2:** $C = 1.33$	**T3:** $C = 1.22$	**T4:** $C = 1.38$	**T5:** $C = 1.35$
X_O	226.3m	221.0m	226.0m	223.5m	220.5m
Y_O	−322.2m	−322.4m	−323.4m	−321.2m	−323.1m
θ	128.9°	126.0°	127.8°	125.9°	125.0°
D_O	1.7m	2.8m	2.2m	1.6m	1.4m
U_O	1.1m/s	0.7m/s	2.0m/s	0.6m/s	1.6m/s
T_O	42.6°C	40.4°C	42.8°C	38.6°C	46.0°C
T_a	31.0°C	31.0°C	30.7°C	30.8°C	30.9°C
S_O	28.3*ppt*	29.7*ppt*	27.3*ppt*	30.0*ppt*	28.9*ppt*
S_a	25.4*ppt*	25.6*ppt*	25.5*ppt*	25.6*ppt*	25.5*ppt*
N_T	0.44	0.43	0.50	0.35	0.52
R_T	14.6	16.0	8.8	14.4	15.9
N_S	0.27	0.58	0.12	0.47	0.46
R_S	8.8	9.4	15.3	12.9	14.2

III: 7/14/12	**T1:** $C = 1.17$	**T2:** $C = 1.11$	**T3:** $C = 1.10$	**T4:** $C = 1.05$	**T5:** $C = 1.16$
X_O	224.3m	224.3m	224.5m	231.0m	231.0m
Y_O	−318.2m	−317.8m	−324.0m	−324.9m	−324.0m
θ	129.4°	130.5°	127.0°	130.4°	131.7°
D_O	3.9m	1.6m	1.8m	2.8m	2.7m
U_O	1.0m/s	1.5m/s	1.2m/s	1.4m/s	0.6m/s
T_O	41.1°C	47.5°C	43.5°C	37.9°C	40.3°C
T_a	30.9°C	30.7°C	30.8°C	30.6°C	30.7°C
S_O	28.4*ppt*	31.7*ppt*	29.2*ppt*	27.0*ppt*	28.1*ppt*
S_a	25.5*ppt*	25.3*ppt*	25.5*ppt*	25.3*ppt*	25.1*ppt*
N_T	0.57	0.59	0.49	0.33	0.35
R_T	16.0	11.5	13.9	7.9	13.0
N_S	0.38	0.74	0.49	0.08	0.34
R_S	13.6	2.3	8.7	9.7	7.5

3.6 Model Integration with MOOS-IvP

Using the model and parameter estimation results, a number of MOOS applications were developed to aid in mission planning, behavior development and online estimation. The model is implemented as a C++ library that can be used across different applications. These applications include simulated sensors, visualization tools, and online estimators. The modeling fitting results reported in Section 3.5.2 are used to select appropriate parameters to use with the library. By varying around these results, different jet conditions can be simulated.

Two simulated sensor applications were developed: iYSISim and iADCPInstrumentSim. These applications simulate temperature and salinity sampling by a CTD or sonde and velocity measurements by an ADCP. Parameter settings are typically shared across application configuration files so that the same jet is being sampled by each virtual sensor. The application can be configured with standard deviation settings so that the reported measurements maintain the same noise characteristics as the physical sensor.

By design, the applications report their readings to the MOOSDB using the same format as the MOOS applications driving the physical sensors. This feature makes it possible to plan sampling missions within simulation before testing in the field. Any other applications interacting with the sensor data, such as a behavior planner, can be configured to interact with the simulated sensors in the same way as the field sensor. In the case of adaptive behaviors, this feature greatly decreases development time and need for field testing. Behavior developers can test and optimize MOOS behaviors in simulation and then deploy the autonomy in the field without making any changes to the behavior configurations.

Two visualization tools were also developed to aid in simulation and field deployments. These applications operate by displaying a colored grid overlay onto a map within the MOOS-IvP mission viewer application, pMarineViewer. The first application, pJetGridRender, displays the simulated jet field on the viewer map. This allows mission planners and developers to observe the simulated jet that virtual vehicles are

sampling. At the beginning of a mission, it queries the model at each grid point to determine the value of the simulated temperature, salinity and velocity at that point. These values are then used to color the grid. Depending on what is selected, either the temperature, salinity or velocity field can be displayed.

As often the case with marine sampling missions, limited cruise time and knowledge of a targeted feature makes the rapid assessment of data products essential for successful direction of sampling efforts [40]. An additional visualization application known as pSensorData was developed to specifically address this issue by providing a real-time display of sensor data during a mission. By doing so, this application allows a vehicle operator to both verify the that sensors are operating as expected and to redirect vehicles to areas of interest without having to redeploy vehicles and analyze data.

pSensorGrid runs on a operator computer and subscribes to sensor reports published by vehicle applications containing sensor readings and their locations. These reports are relayed from the vehicle computers to the operator computer using a local WIFI network. Once a new report is received, a colored grid corresponding to the sensor report type, e.g. salinity, temperature or velocity, is updated. C++ objects representing each grid keep track of reported values within each grid box as well as the minimum and maximum values received. The active grid is displayed as an overlay within pMarineViewer. Depending on the needs of the mission, the operator can cycle through active grids so that different fields can be displayed. Because pSensorData is configured to work with the MOOS sensor drivers, it can display measurements from simulated and hardware sensors.

These components are demonstrated in Figure 3-5. In this figure a pJetGridRender overlay of a simulated jet temperature field is shown within the mission viewer. This jet field was sampled by a virtual vehicle operating the simulated CTD application. The noisy measurements taken by this application are used by the estimator to produce the estimated trajectory, shown by the green line.

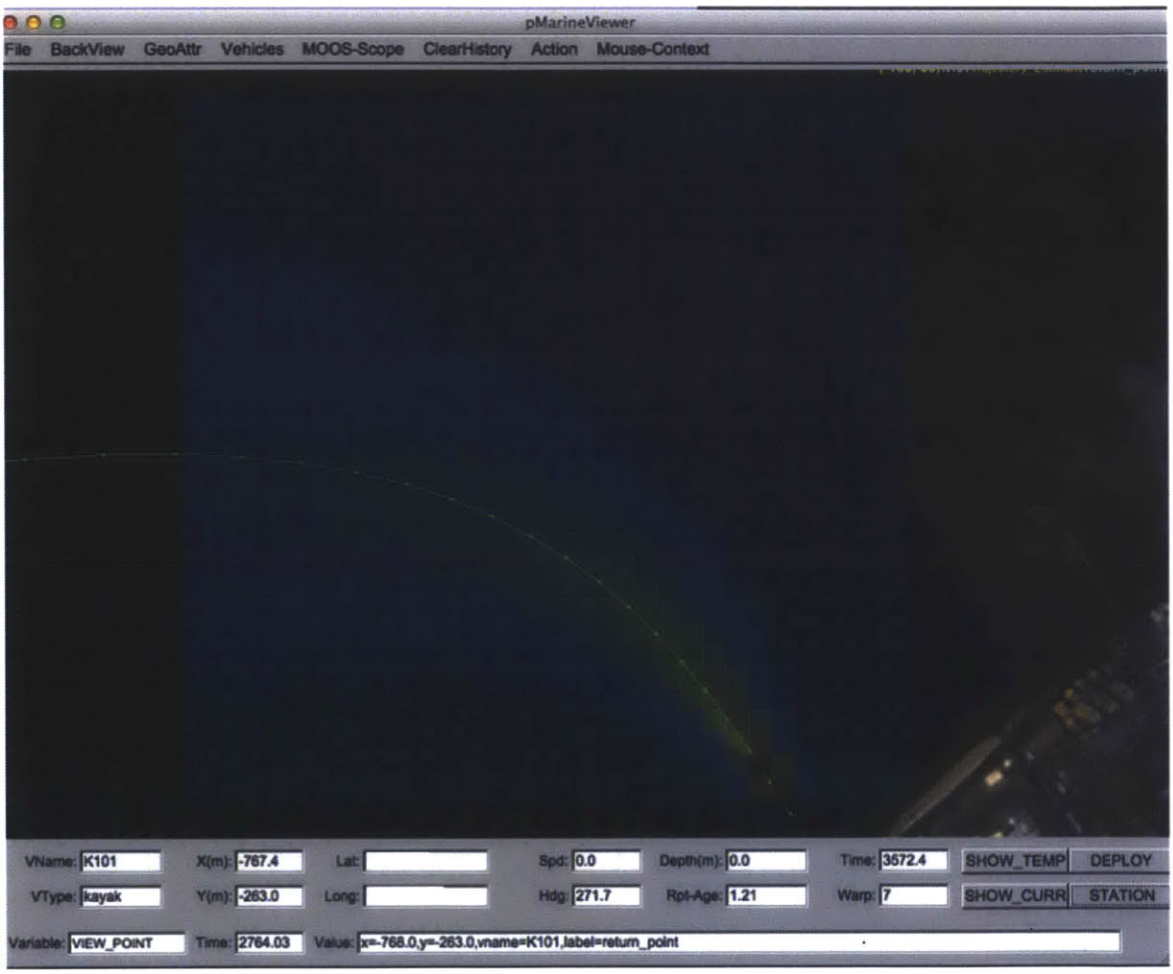

Figure 3-5: Screen shot of jet sampling simulation environment within MOOS-IvP. pMarineViewer map contains an overlay of the jet field produced by pJetGridRender. Jet trajectory estimated from measurements taken by virtual vehicle's simulated CTD is shown in with a green line.

Chapter 4

Autonomy Strategy

This chapter documents an autonomous sampling strategy that adaptively samples a thermal and effluent jet and plume using an ASV. By employing adaptive transects, sensor fusion and online estimation, the strategy is able to autonomously map the boundaries and extent of the jet field and subsequent plume. Due to tight integration with MOOS-IvP, the strategy can be deployed alongside other autonomous behaviors and is extendable to collaborative, multiple vehicle sampling missions. The strategy was developed and tested in simulation using the thermal and effluent jet-plume model presented in Chapter 3. As part of a bi-yearly coastal environmental survey in Singapore, the strategy was tested at a power plan cooling outfall. Results of this experiment are reported.

The development of this strategy was motivated out of a need to rapidly and accurately measure the distribution, span and extent of thermal and effluent jets and plumes produced at industrial cooling outfalls. These features are the focus of environmental surveys conducted by the Center for Environmental Sensing and Modeling (CENSAM) in Singapore. Previous sampling strategies consisted of pre-planned lawnmower surveys executed by ASVs. Temperature measurements obtained during one such survey are shown in Figure 4-1. As is typical with these surveys, the pre-planned paths fail to obtain measurements that could be used to identify the boundaries and extent of the jet and plume, thus motivating the need for an adaptive strategy.

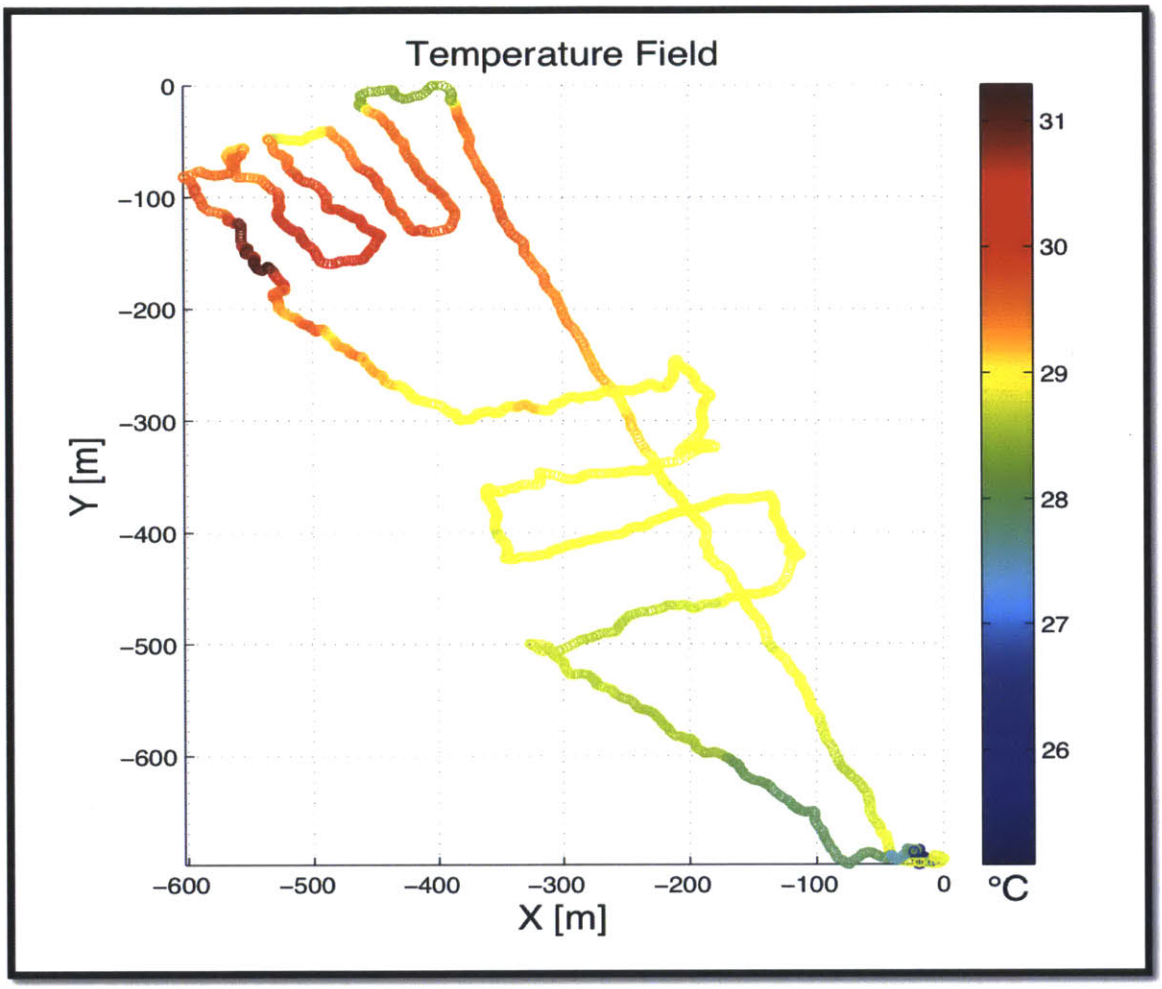

Figure 4-1: Temperature survey at Site 2. Boundaries of the jet and plume are not mapped and unnessasary transects are executed in an attempt to locate the far field of the plume.

This chapter is organized as follows. Section 4.1 provides an overview of related work on adaptive sampling. Section 4.2 documents the theory of sensor fusion and adaptive transects as it applies to thermal and effluent jets. Section 4.3 describes the implementation of the autonomous strategy within MOOS-IvP . Simulated sampling missions using single and multiple vehicles are described in Section 4.4. Field results are reported in Section 4.5.

4.1 Pior Work

Adaptive sampling is an important area of research in marine robotics. Full coverage of the sampled environment is rarely achievable and many features of interest span a wide range of spatial and temporal scales. For these reasons, sampling efforts can be improved through the implementation of adaptive strategies.

Jet and plume sampling is concerned with characterizing the feature's source, boundaries, and temporal evolution in addition to its physical, chemical and biological makeup [32, 52, 19]. Various adaptive strategies have been developed to obtain these characterizations. Many strategies combine forms of sensor fusion and adaptive transects [29, 47, 22, 11]. These approaches are adopted from plume tracking behavior observed in animals [29] and assume that sensor arrays can provide more information about plume characteristics than single sensors. In [30] sensor fusion is used with model-based gradient descent and Kalman filter methods to localize a gas plume source with a mobile robot. An approach phase is followed by a adaptive transect-based search phase that travels from the far-field to the source. In [47] and [22], a model-independent, threshold-based approach is used to direct adaptive transects as an alternative to gradient methods. This threshold approach is motivated by the strong influence of turbulence in high Reynolds number regions, such as the jet flows discussed herein, that cause significant variation in instantaneous measurements that interfere with gradient calculations. Attempts are made to direct transects so that a vehicle stays within sensor fusion thresholds.

Probabilistic strategies have also been developed that inform human planning through jet and plume characteristic detection [31, 40] . In [31] occupancy grid mapping algorithms are applied with the goal of detecting multiple hydro thermal vent sources by an AUV. The measurements taken during a lawnmower survey are analyzed to produce maps of plume source likelihood. These maps are used to redirect the vehicle on later surveys.

When the sensor signatures indicating the presence of the feature are initially unknown, additional methods must be employed to identify the significant readings.

This case is addressed in [40] in the context of the autonomous sampling by the Sentry AUV of oil plume produce by the Deep Water Horizon Oil Spill. The AUV was deployed with 11 potentially relevant scalar sensors. Initial measurements recorded by these sensors were separated into distinct classes using an algorithm based on a Bayesian, non-parametric, Variational Dirichlet Process model [42]. This model assumes that the observations can be represented using a Gaussian Mixture Model (GMM), and are independently and identically distributed (i.i.d.) when conditioned on their class label. Labeling of classes by humans allowed the algorithm to learn the classes and automatically identify significant fields and signatures.

4.2 Sensor Fusion and Adaptive Transects

Chapter 3 establishes that thermal and effluent jets produced at industrial cooling outfalls exhibit a specific structure that can be exploited by an adaptive sampling strategy. In its most basic form this structure is such that these features produce scalar fields with Gaussian cross-sections and decaying centerlines. Since all fields of the jet vary along this structure, sensor fusion can be used to compute generalized cross-sections and localize the jet centerline. Once centerline locations and cross-sections are characterized, transect directions and bounds can be adjusted to sample within the jet and plume regions. This strategy is similar to those implemented in [30, 47, 22, 11] in that it employs both sensor fusion and adaptive transects. These strategies are adapted for the specific problem of thermal and effluent jet and plume mapping in which the approximate jet location and initial direction are known.

4.2.1 Sensor Fusion

Sensor fusion is achieved using a "jet indicator function". Similarly to Cannel et. al [11], this function is computed using the weighted root-mean-square of the normalized field readings. Let $\alpha_{i,k}(t)$ represent the time series of an individual jet field $i \in \{1, .., n\}$ for transect k. The corresponding normalized reading, $\hat{\alpha}_{i,k}(t)$, is calculated

according to Eq. 4.1.

$$\hat{\alpha}_{i,k}(t) = \frac{\alpha_{i,k}(t) - \underline{\alpha}_{i,k-1}(t)}{\overline{\alpha}_{i,k-1}(t) - \underline{\alpha}_{i,k-1}(t)} \tag{4.1}$$

where $\overline{\alpha}_{i,k-1}t)$ and $\underline{\alpha}_{i,k-1}(t)$ represent the maximum and minimum field values from the previous transect. When $\alpha_{i,k-1}(t)$ falls outside of the the bounds of the previous transect, the bounds are updated to ensure that $0 \leq \hat{\alpha}_{i,k}(t) \leq 1$. The current maximum and minimum are used on the first transect. Given $\hat{\alpha}_{i,k}(t)$, the jet indicator function along transect, $J_k(t)$, is then calculated according to Eq. 4.2.

$$J_k(t) = \sqrt{\gamma_1 \hat{\alpha}^2_{1,k}(t) + \gamma_2 \hat{\alpha}^2_{2,k}(t) + ... + \gamma_n \hat{\alpha}^2_{n,k}(t)} \tag{4.2}$$

where γ_i represents the field weight. Weights can be adjusted dynamically to account for changes a field's indication value. For example, the velocity field exhibits lower influence at increased distances from the outfall, so its weight is lowered as k increases. Certain jet fields are deficient in the region of the jet. In these cases, $J_k(t)$ is calculated using $1 - \hat{\alpha}_{n,k}(t)$.

The jet indicator function takes on values between 0 and 1. A value of 1 indicates measurements taken at the jet centerline. As the radial distance from the centerline increases, the indicator function tends towards 0, indicating that measurements are in the ambient. To ensure that the output of the jet indicator function is consistent between transects, two conditions must be met. The transects must be orthogonal to the centerline direction at the crossing and the measurements obtained during the previous transect must encompass the complete range of field readings for the corresponding cross-section.

These conditions are met using eight transects of the straight jet model. Simulated, measurements of temperature, salinity and velocity are used to calculate $J_k(i)$ as shown in Figure 4-2. As transects are located farther from the jet origin, the peak of J_k remains located at the jet centerline and the spread of J_k increases. These findings are consistent with the Gaussian cross-sections defined in the model.

The introduction of a crossflow and the widening of the jet causes the same transects to fail the orthogonally and completeness conditions, the effects of which are

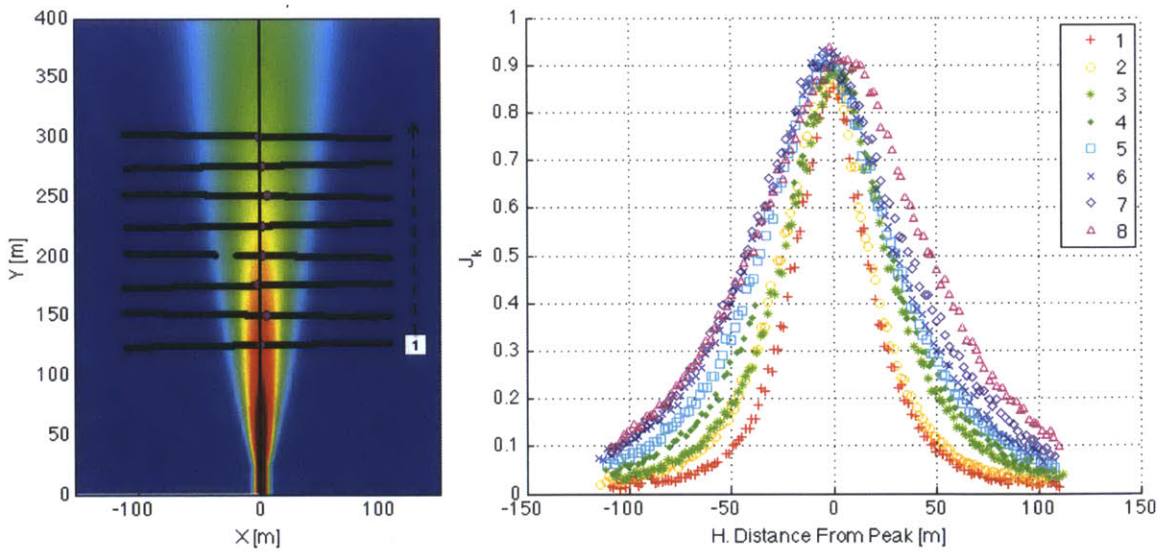

Figure 4-2: Left: Transects are orthogonal to jet centerline. Peak jet indicator function positions (pink) fall on centerline. Right: Jet indicator function series plotted along each transect. Series are shifted to align indicator function peaks. Orthogonal transects ensure symmetric series that are similar among transects. Complete transect crossings produce peaks near 1.

shown in Figure 4-3. As the jet widens, the transects no longer cross into the ambient region on both ends. Due to the curved trajectory induced by the crossflow, centerline decay of the jet fields is not consistent within a transect. This tends to bias indicator peaks away from the direction of the crossflow. Transects further from the origin do not cross the jet completely, resulting in indicator function values that are both attenuated and shifted.

4.2.2 Adaptive Transects

Adaptive transects alleviate the issues related to curved jet trajectories by altering the transect direction and length based on the indicator function readings. Peak indicator function locations are reported to the online estimator to produce estimates of the jet trajectory. This estimate is used to alter the direction of later transects to produce near-orthogonal crossings of the centerline. The orthogonal transect directions are adjusted to produce zig-zagging transects along the length of the jet. Transects are bounded according to an indicator function threshold, $\underline{J}$. Once $J_k(t) < \underline{J}$, the vehicle

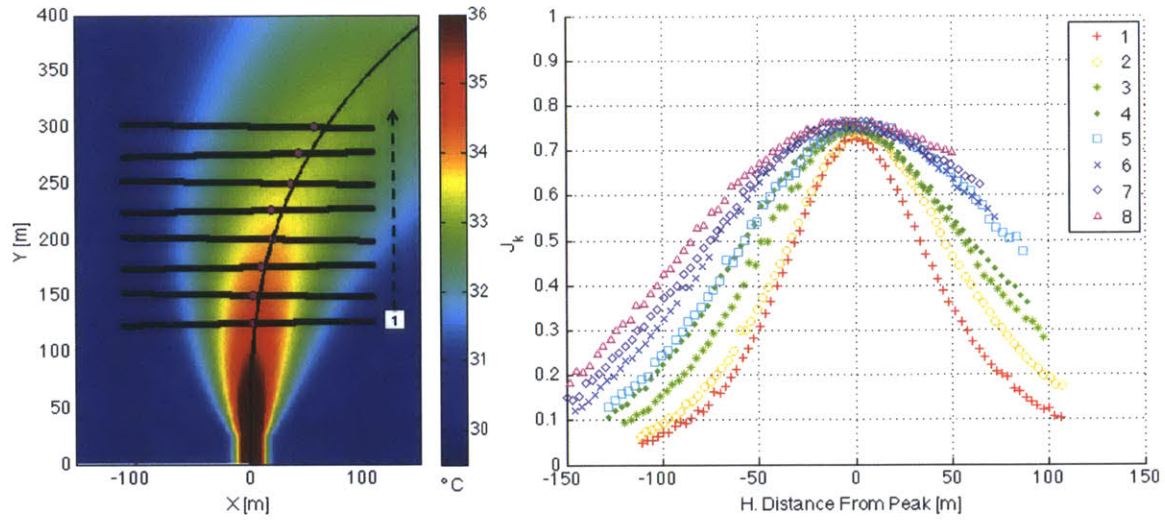

Figure 4-3: Left: Transects are not orthogonal to jet centerline. Peak jet indicator function positions (pink) fall to the left of the centerline. Right: Jet indicator function series plotted along each transect. Series are shifted to align indicator function peaks. Non-orthogonal transects cause asymmetric series that differ among transects. Incomplete transect crossings produce attenuated peaks.

transitions to the next transect. To ensure the collection of ambient measurements, adjustable padding is added to the end of each transect.

Figure 4-4 demonstrates the use of adaptive transects. A threshold of $\underline{J} = 0.2$ is used to produce wide transects that enter the ambient. After one static trajectory pass the vehicle begins adaptive transects. As shown in the indicator function plots, these transects produce symmetric indicator function series that are not attenuated. The span of the indicator series are narrower than those shown in Figure 4-3. The narrowed span is caused by the non-zero indicator threshold. Due to the consistency in these series, it is possible to develop an autonomy behavior based on the jet indicator function and adaptive transects. This behavior is capable of tracking and sampling a jet and plume into the far field.

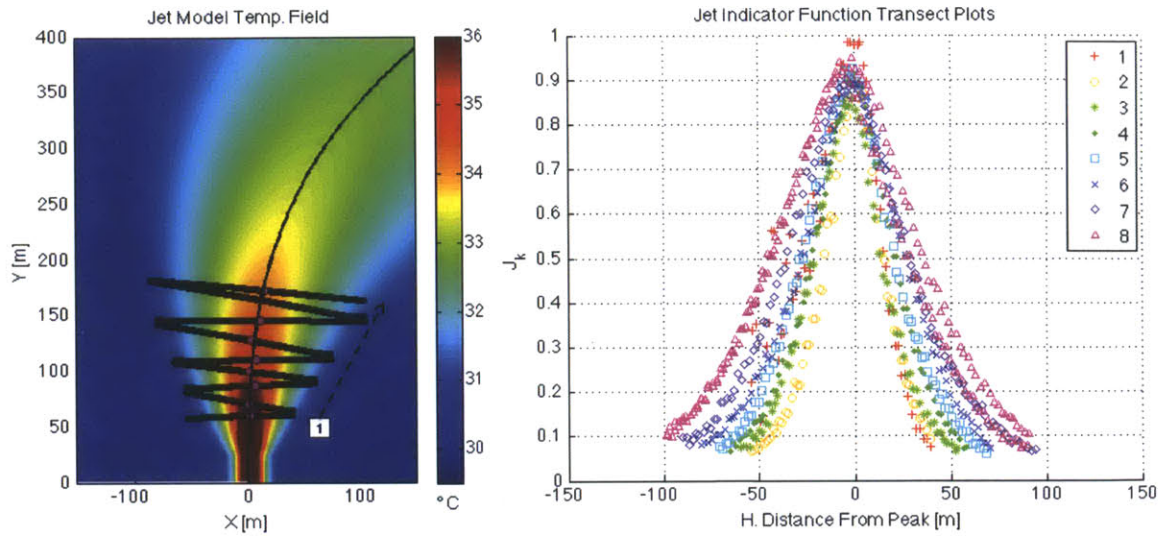

Figure 4-4: Left: Adaptive transects produce near-orthogonal crossings of the jet centerline. Peak jet indicator function positions (pink) fall on the centerline. Right: Jet indicator function series plotted along each transect. Series are shifted to align indicator function peaks. Due to the adaptive direction and length of the transects, the indicator series are symmetric and consistent. Indicator peaks approach 1.

4.3 Strategy Implementation

Parameter estimation, sensor fusion and adaptive transects are implemented within MOOS-IvP to produce an autonomous thermal and effluent jet sampling strategy. This implementation is achieved through the development of several new MOOS applications and a MOOS-IvP behavior. Through the use of these modules the sampling strategy can be deployed in the field and simulation across multiple vehicles.

4.3.1 Sensor Fusion Application: pJetData

Sensor fusion is handled by the MOOS application pJetData. pJetData can be configured to subscribe to any number of sensor reports produced by other MOOS applications on a vehicle. Each unique report type is used in the jet indicator function calculations. Upon the arrival of a new report, the active field limits are updated and the indicator function is recalculated. In order to make the indicator function more robust against eddies, turbulence, sensor noise and non-uniform patches a running average of function values is computed. pJetData then publishes an indicator report

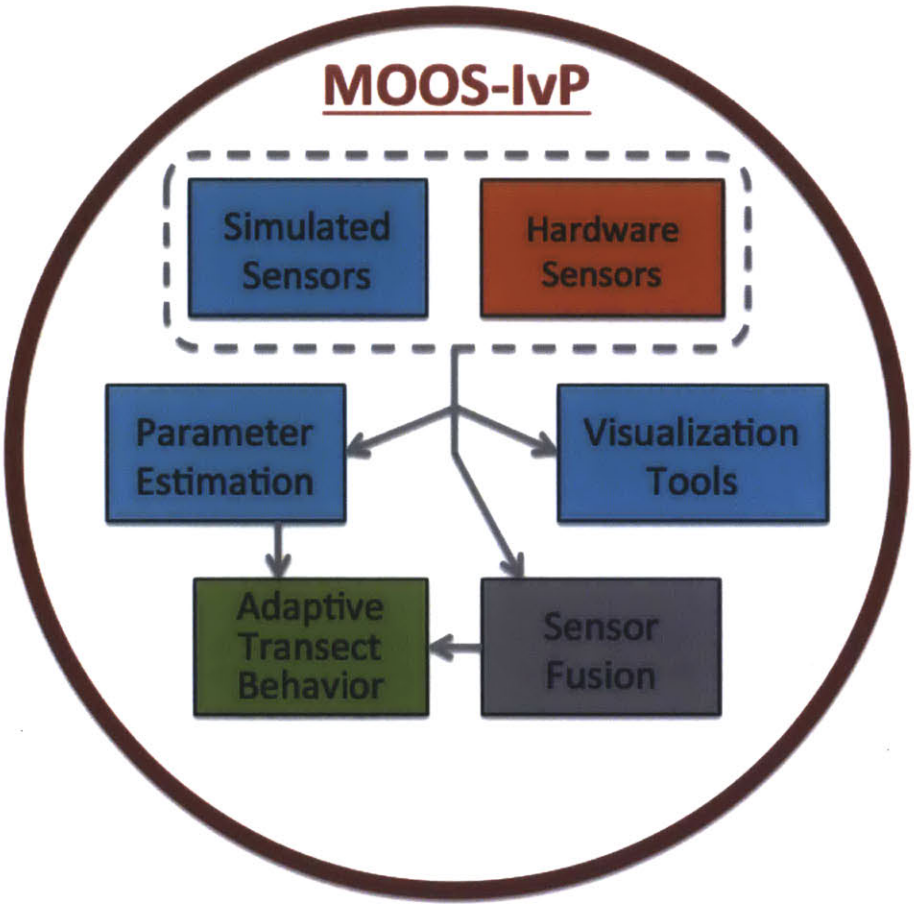

Figure 4-5: Diagram of jet adaptive sampling strategy implemented within MOOS-IvP. Simulated or hardware sensors provide measurements for parameter estimators, sensor fusion and visualization tools. An adapative transect behavior uses estimator and sensor fusion results to direct sampling.

to the local MOOSDB with the indicator function value and vehicle location. Any other MOOS application or behavior can then subscribe to these indicator reports. pJetData also relays all sensor reports to other vehicles making it possible for remote online estimators to utilize the local measurements.

Transect-based behaviors such as a lawnmower waypoint behavior or an adaptive transect behavior can be configured to inform pJetData of the start of a new transect. At the start of a new transect pJetData updates the limits that are used for normalization calculations. pJetData also posts a report to the local and remote MOOSDBs of the peak indicator function location for the previous transect. These reports are used for online trajectory estimates.

4.3.2 Online Estimation Application: pJetEstimate

Online estimation results can be used by both autonomy behaviors and human operators to direct sampling vehicles. Using the SA methodology outlined in Algorithm 3.1, two online estimators were developed to supplement the sampling strategy. The first estimator produces live straight jet parameter estimates of P during a sampling mission using temperature, salinity and velocity data collected by multiple vehicles in the field. The resulting parameters can be utilized by human operators to select areas for further investigation. A trajectory estimator fits the trajectory power law used by the jet model to measured centerline locations.

These estimators are implemented within the MOOS application pJetEstimate. The application is configured with the estimator bounds, cooling steps and temperature constants. In the case of the trajectory estimator, a new set of parameters and cost function are used. The parameters consist of the jet origin, jet angle, crossflow length scale and trajectory coefficient, all shown in Eq. 4.3.

$$\text{Trajectory} = f(X_O, Y_O, \theta, l_C, C) \tag{4.3}$$

Using these parameters the jet trajectory is calculated and rotated into the global frame. The positions of the current trajectory solution are represented by the set $p_t = \{(x_t, y_t)\}$. Error, E_j, is computed by determining the shortest distance between a reported centerline position, (x_c, y_c) and the closest (x_t, y_t). Given n centerline reports, the total cost, C, is then the RMSE. This cost function is shown in Eq. 4.5. The estimator results are reported as MOOS variables so other applications can utilize them.

$$E_j = f(x_c, y_c, p_t) \tag{4.4}$$

$$C = \sqrt{\frac{1}{n}\sum_{j=1}^{n} E_j^2} \tag{4.5}$$

pJetEstimate can utilize measurements from any vehicle to produce estimates.

During multiple vehicle deployments pJetEstimate is run on one vehicle that collects measurements and indicator reports from all vehicles in the field through a local WIFI network. Results are then relayed back to other vehicles, so estimates can be shared.

4.3.3 Adaptive Transect Behavior: BHV_JetEdge

The MOOS-IvP behavior, BHV_JetEdge, was developed to produce adaptive transect track-lines for a vehicle sampling a thermal and effluent jet. Each track-line is defined by the transect start location, direction and an arbitrary length. Track-line following is handled by MOOS-IvP's waypoint engine, leaving the higher-level functions of transect production to BHV_JetEdge. The basic operation of BHV_JetEdge is depicted in Figure 4-6. A collection of the primary configuration parameters that can be set for BHV_JetEdge is given in Table 4.1.

BHV_JetEdge is initialized by a preliminary transect produced by a waypoint behavior. The purpose of this transect is to seed the indicator function and provide BHV_JetEdge with an initial guess of the jet trajectory. After this first transect, BHV_JetEdge produces a track-line that takes this initial transect direction and adds an offset so that the vehicle makes forward progress away from the outfall. The amount of forward progress made on each pass is a configurable option set by **Y_DELTA**. After several transects, the number of which is set by **TRAJ_PASS**, the behavior begins to utilize the trajectory estimates for transect direction. This transition is executed over the course of three transects so that an abrupt change in transect direction is avoided.

The behavior can operate in one of two modes. Mode 0 produces transects that survey the complete jet span, while the second mode only surveys the jet boundaries. Once the vehicle receives several indicator reports with values above the threshold, set by **THRESH** in mode 0 and **LOW** in mode 1, a flag is thrown to signify that the vehicle has entered the jet region. If in mode 0, the vehicle continues along its trajectory until several indicator reports are received with values below the same threshold. At this point another flag is thrown. To ensure that boundaries are properly transversed extra padding, set by **EDGE_PAD**, is added to the transect before the vehicle turns

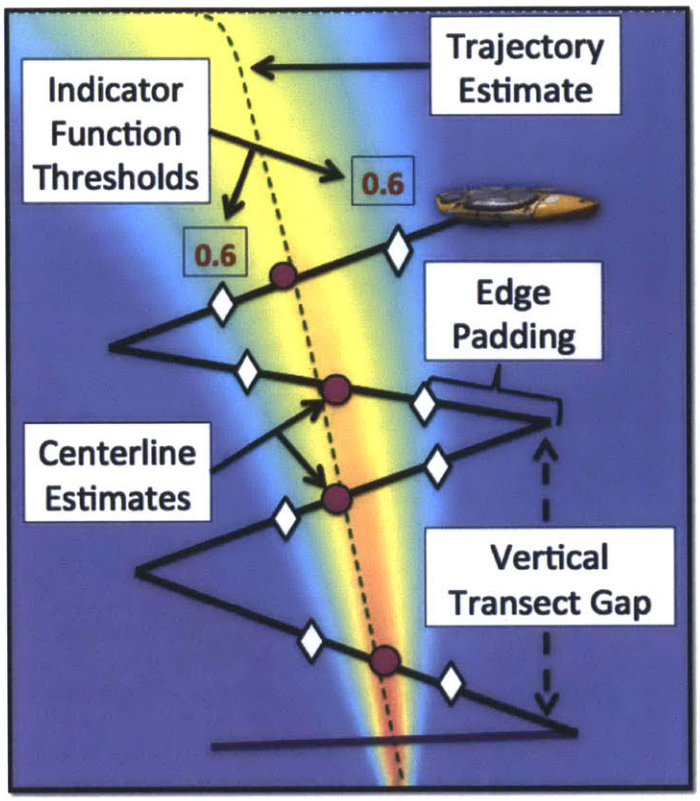

Figure 4-6: Diagram of BHV_JetEdge operation. Initial transect shown in pink line seeds jet indication function. Transects are bounded by indicator function thresholds, shown with white diamonds. Transect direction is based on jet trajectory. This trajectory is shown with a green line. Peak indicator function locations are shown with pink dots.

around. Mode 1 only differs in that the second flag is thrown when the indicator function values pass above the **HIGH** threshold.

A heuristic safety check is implemented along side the threshold detection to maintain predictable transect transitions. If either threshold flags is not thrown, a transect transition is still initiated after the vehicle has traveled twice the distance of the previous transect. The behavior completes after it completes a specified number of transects. To simply configuration, span and boundary surveys can be executed in sequence using the same behavior. When configured in this way, the boundary surveys begin at the end point of the the span surveys.

BHV_JetEdge produces several visual cues that are overlaid on the mission viewer map. These are shown in Figure 4-7. The first cue is a line segment which represents

the vehicle's intended trajectory for a given transect. The two other cues are point markers which mark indicator function threshold crossings and maximum indicator function values on each transect. The threshold crossings appear as white diamonds and the maximum values appear as pink circles. pJetEstimate produces an additional cue in the form of a green line representing the estimated jet trajectory. These cues are valuable resources for mission operators so that they can be informed of the behaviors operation.

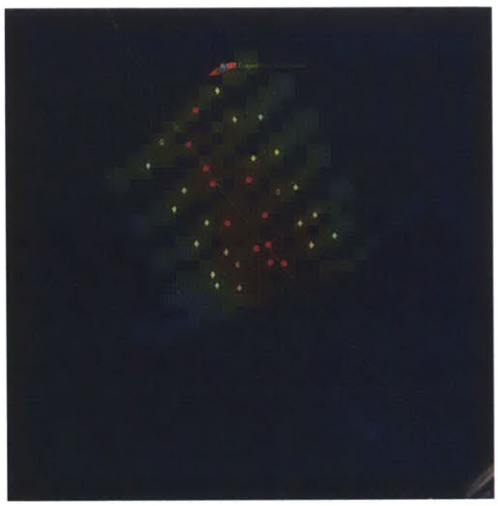

Figure 4-7: Live view of temperature field produced by pSensorGrid within the simulation environment. Note the trajectory estimate and behavior markers.

Table 4.1: BHV_JetEdge Configuration Parameters

Parameter	Default	Description
POINTS	N/A	Waypoint used in initial transect
MODE	0	Behavior mode: 0 for span and 1 for boundary tracking
SIDE	left	Side of jet that the vehicle starts on, i.e. "**left**" or "**right**"
EDGE_SIDE	left	If in mode 1, determines which edge is tracked
THRESH	0.65	Indicator threshold value used in mode 0
LOW	0.2	Low threshold value used in mode 1
HIGH	0.75	High threshold value used in mode 1
Y_DELTA	15m	Amount of progress to be made away from the outfall on each transect
THRESH_COUNT	10	Number of indicator reports needed below or above a threshold before a flag is thrown
EDGE_PAD	30m	Amount of padding to added at the end of each transect
NUM_PASS	10	Number of span passes before behavior completes
EDGE_PASS	0	Number of edge passes before behavior completes
TRAJ_PASS	6	Number of passes before behavior uses trajectory estimate

4.4 Simulation Environment

Sensor fusion, online estimation and simulated sensors are used to produce a jet-plume sampling simulation environment within MOOS-IvP. By leveraging the MOOS-IvP modules for simulated vehicle dynamics, field communications and mission planning, this environment becomes a useful tool for the development of jet-plume sampling behaviors and the planning of sampling missions.

Typical use of the environment involves the deployment of one or more virtual ASVs equipped with simulated sensors. Using either pJetGridRender or pSensorData, the jet fields are visualized so that the operator can correlate the behavior of the vehicle with the environment being sensed. Using the MOOS-IvP warp functionality simulated sampling missions are able to run at 10x speed making it possible to quickly alter model or behavior parameters and view the results. If estimation is needed, estimator results can also be displayed so that they can be evaluated by the operator.

BHV_JetEdge was developed through extensive use of this simulation environment. After behavior development was completed, multi-vehicle sampling missions were planned and simulated across a variety of jet conditions and behavior settings. The goals of these missions were to test the functionality of BHV_JetEdge and the parameter estimators, develop a multi-vehicle sampling strategy and to produce realistic mission plans which could be implemented in the field with little alteration. Three of these missions are outlined below. Two lawnmower survey missions are used as a baseline for comparison.

Jet model parameters are selected from the Site 1 July, 14th estimation results reported in Section 3.5.2 and are kept constant through all missions reported here. A weak crossflow representative of the tidal flows observed at Site 1 is introduced to induce a curve jet trajectory. These parameters as well as the estimator bounds are reported in Table 4.2. The mission simulations presented here are configured to represent missions that could realistically be deployed during CENSAM field trials. Mission length is kept under 60min and maximum vehicle speeds are set at 0.7m/s. Quantitative comparisons of missions are performed using the final cost functions

Table 4.2: Jet model parameters and estimator bounds used for mission simulations.

	Set Value	LB	UB
X_O	−165m	−200m	−150m
Y_O	−335m	−340m	−300m
θ	126°	103°	143°
ϕ	246°	N/A	N/A
D_O	3.9m	1m	4m
U_O	1.4m/s	0.5m/s	2.0m/s
U_C	0.07m/s	0m/s	2.0m/s
T_O	41°	$32°C$	$50°C$
T_a	30°	$28°C$	$31°C$
S_O	29*ppt*	27*ppt*	32*ppt*

	Set Value	LB	UB
S_a	24.5*ppt*	24*ppt*	26*ppt*
N_T	0.5	0.05	1
R_T	14	0.5	30
N_S	0.5	0.05	1
R_S	10	0.5	20
N_V	1	0.05	1
R_V	47	0.5	50
C	5	2	12
L_C	80m	20m	300m

of the straight jet and trajectory estimators, the cost of the combined curved jet estimate and the parameter root mean square relative error (pRMSRE). Temperature, salinity and velocity measurements are used for straight jet parameter estimates. Trajectory estimates make use of the peak indicator function locations reported for each transect. At the conclusion of each mission, jet and trajectory estimates are combined to produce a curved jet estimate. The RMSRE is defined for the combined set of parameters estimated by pJetEstimate:

$$P^* = \{X_O, Y_O, \theta, \phi, D_O, U_O, U_C, T_O, T_a, S_O, S_a, N_T, R_T, N_S, R_S, N_V, R_V, C, L_C\}$$

This set is made up of the jet model parameters, P, and the trajectory parameters, C and L_C. Letting p_j represent an individual model parameter and p_j^* represent the estimate of p_j, pRMSRE is calculated for the $n = 19$ parameters according to Eq. 4.6.

$$pRMSRE = \sqrt{\frac{1}{n}\sum_{j=1}^{n}\left(\frac{p_j^* - p_j}{p_j}\right)^2} \tag{4.6}$$

4.4.1 LM1 Mission: Solo Vehicle Lawnmower Survey

A baseline lawnmower survey mission is configured to reflect the lawnmower surveys typically conducted at Site 1 during CENSAM field trials. The survey is defined by a 125m long, 100m wide rectangle made up of 6 transects. The transect path is rotated so that the transect direction is orthogonal to the initial jet direction. With the maximum vehicle speed set at 0.7m/s this survey is completed in approximately 20min. This speed reflects a realistic speed achievable by a kayak while transversing a jet.

For the first lawnmower survey mission, one vehicle equipped with a simulated CTD sensor and ADCP is deployed. The standard deviation of the sensor noise is set at $0.02°C$, $0.02ppt$ and 30cm/s to reflect the noise statistics of the physical sensors. A summary of the estimator results produced during five simulation runs are reported in Table 4.3. Plots of the simulated temperature and salinity observations and the estimated curved jet fields are shown in Figure 4-8 for trial 1.

Table 4.3: LM1 Mission Results

	Str. Cost	**Traj. Cost**	**Curved Cost**	**pRMSRE**
T1:	1.52	5.16	1.51	0.667
T2:	1.58	2.88	1.54	0.192
T3:	1.52	4.39	1.56	0.608
T4:	1.52	3.82	1.67	0.525
T5:	1.52	4.40	3.34	0.151
T6:	1.53	1.26	1.59	0.235
T7:	1.52	3.29	1.56	0.662
T8:	1.52	5.30	1.58	0.662
T9:	1.53	2.08	1.60	0.103
T10:	1.53	1.80	1.63	0.148

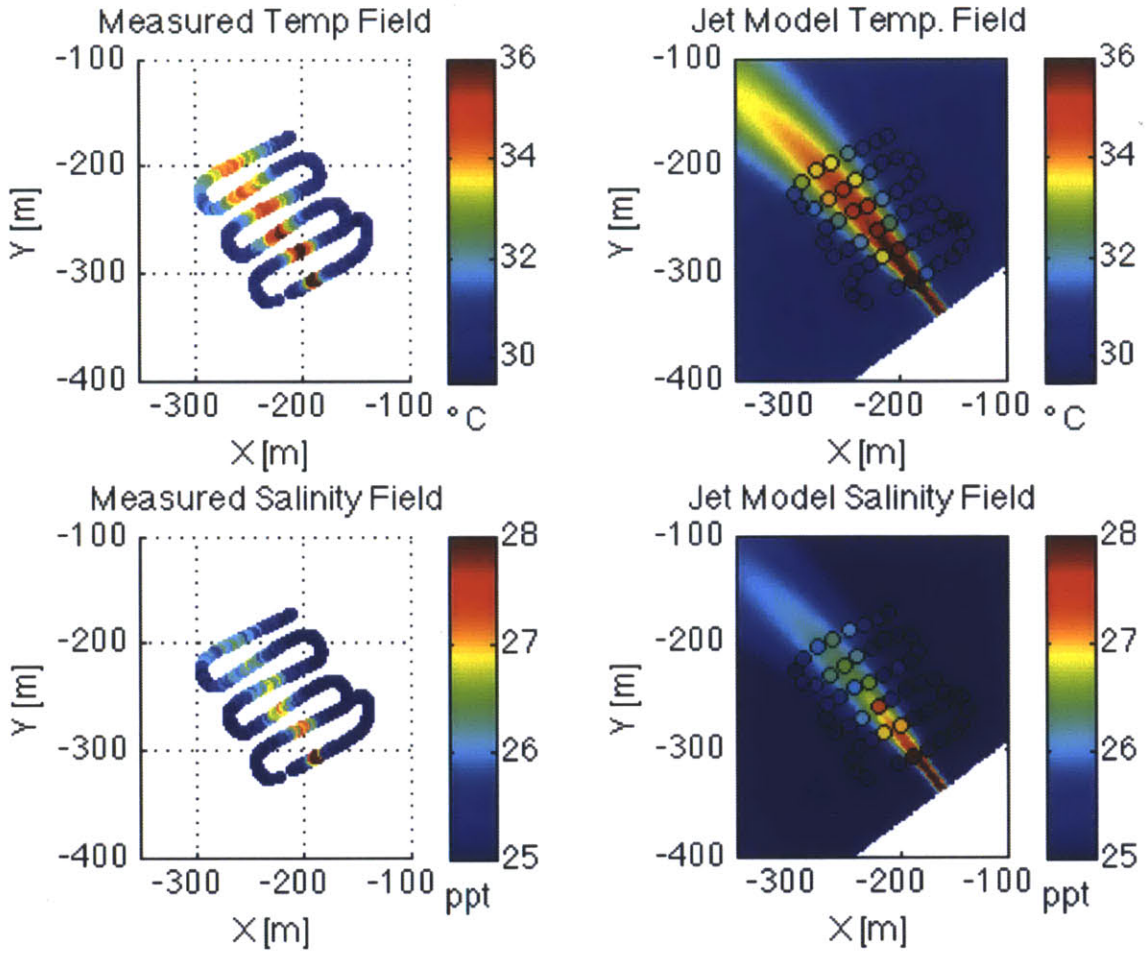

Figure 4-8: Observed (left) and Estimated (right) Temperature and Salinity Fields for a simulated lawnmower survey mission at Site 1. The curved jet estimated fields shown coorspond to a cost of 0.98.

4.4.2 LM2 Mission: Two Vehicle Lawnmower Survey

A second lawnmower survey mission is configured in order to provide a comparative baseline for adaptive transect missions that extend into the far field of the jet. This mission utilizes two vehicles each conducting one lawnmower survey. The first vehicle is equipped with an simulated ADCP and a temperature probe (a simulated CTD reporting only temperature). This vehicle conducts the same survey as described in Section 4.4.1. This survey is referred to as $S1$.

The second vehicle is equipped with a simulated CTD. Without any prior knowledge of the far-field behavior of the jet it is difficult to strategically place the second

survey, $S2$. Instead a random placement is used. Before each run of the simulation, $S2$ is place at a random angle from the outfall direction, β, and random distance, L, from the center of $S1$. The second survey is also rotated a random angle, Ψ. The sign and bounds of β are selected so that $S2$ is a appropriately placed given the tidal direction. Bounds for L are selected to place $S2$ between $1-5$ transect lengths from $S1$. A diagram of the second lawnmower survey is shown in Figure 4-9.

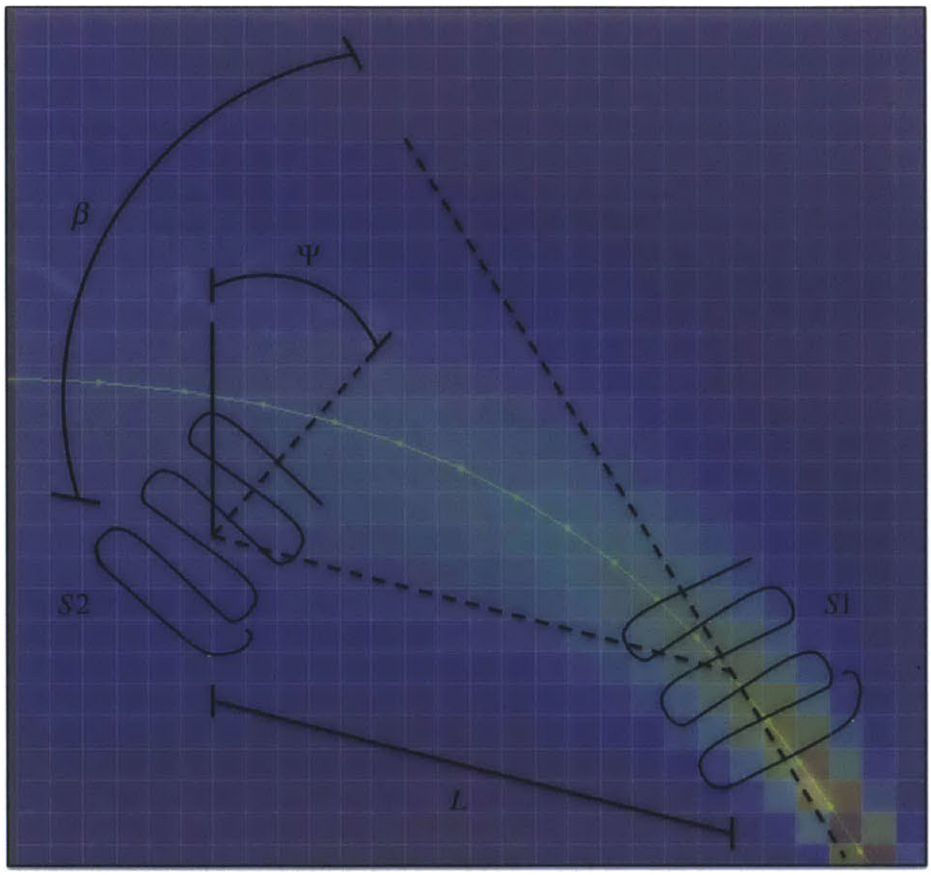

Figure 4-9: A diagram of the lawnmower survey 2. The far field of the jet is surveyed by placing $S2$ relative to $S1$ using a random set of parameters, (β, L, Ψ).

Five simulation runs are conducted. Mission lengths ranged from 20min to 30min depending on the placement of $S2$. Measurements from $S2$ are only used for straight jet estimates. The estimator costs of these runs are reported in Table 4.4. The values of (β, L, Ψ) for each run are given in the first column. Plots of the observations and estimation results for trial one are shown in Figure 4-10.

Table 4.4: LM2 Mission Results

	Str. Cost	Traj. Cost	Curved Cost	pRMSRE
T1(26.16°, 110.37m, 98.94°):	1.23	2.27	1.62	0.238
T2(26.12°, 268.15m, 59.46°):	1.23	0.77	1.51	0.361
T3(12.28°, 347.71m, 53.94°):	1.23	3.43	1.49	0.104
T4(16.01°, 348.45m, 95.25°):	1.23	0.88	1.26	0.507
T5(8.07°, 305.43m, 33.20°):	1.22	3.55	1.98	0.123
T6(47.12°, 441.59m, 88.96°):	1.23	2.22	1.56	0.211
T7(50.79°, 131.86m, 90.94°):	1.21	2.52	1.37	0.316
T8(3.92°, 271.25m, 17.38°):	1.23	2.27	2.10	0.119
T9(7.63°, 338.70m, 40.68°):	1.23	1.42	1.79	0.311
T10(6.42°, 188.12m, 62.97°):	1.23	1.80	1.47	0.218

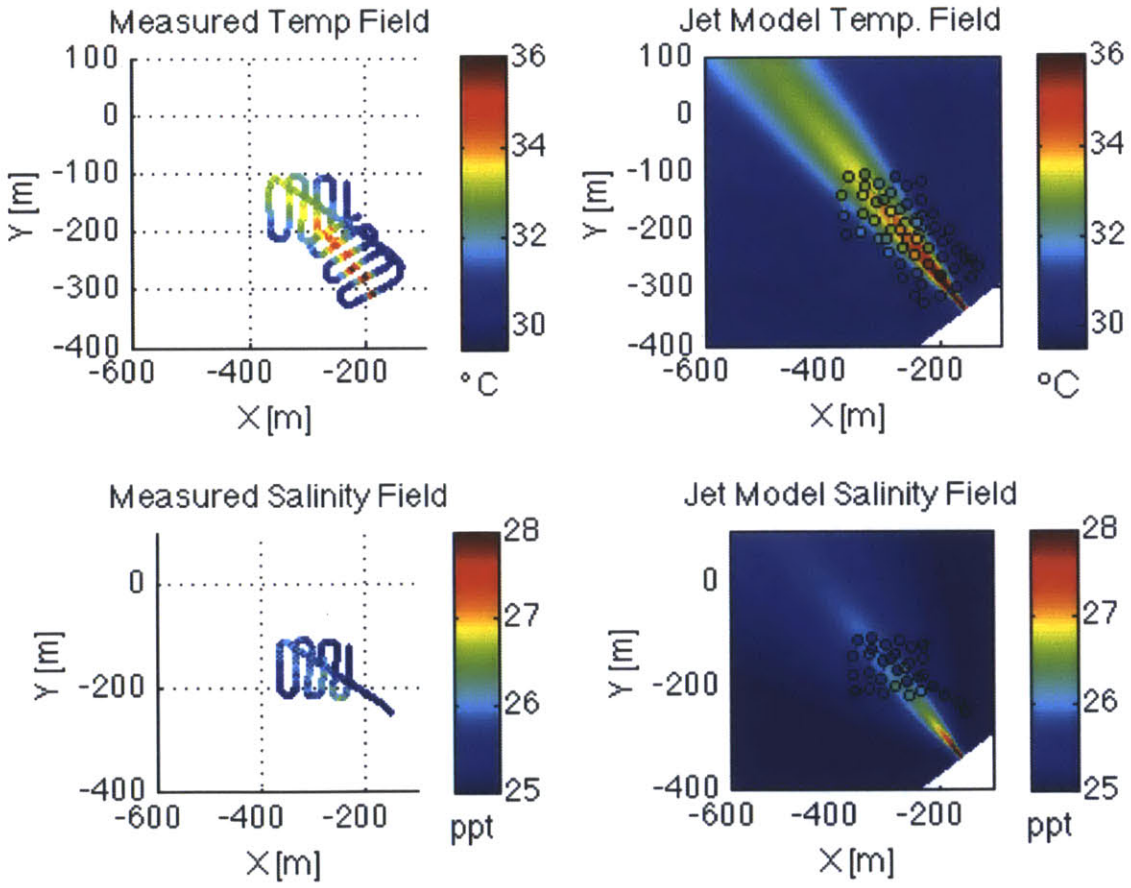

Figure 4-10: Observed (left) and Estimated (right) Temperature and Salinity Fields for a simulated two vehicle lawnmower survey mission at Site 1. The curved jet estimated fields shown coorspond to a cost of 1.24.

4.4.3 A1 Mission: Solo Vehicle Adaptive Survey

One vehicle equipped with a simulated CTD sensor is deployed in the first adaptive mission. The vehicle completes 12 adaptive transects. Trajectory estimates are used after the 3 transects. The jet indicator function threshold and edge padding are set at 0.6 and 30m respectively. Mission lengths for five simulation runs ranged from 20min to 30min. Estimator costs are shown in Table 4.5. Plots of the observations and estimation results for trial one are shown in Figure 4-11.

Table 4.5: A1 Mission Results

	Str. Cost	Traj. Cost	Curved Cost	pRMSRE
T1:	1.52	3.02	1.96	0.299
T2:	1.51	1.51	2.09	0.285
T3:	1.52	1.36	1.92	0.255
T4:	1.51	3.93	1.76	0.155
T5:	1.50	2.52	1.83	0.298
T6:	1.71	3.05	1.81	0.360
T7:	1.54	2.03	3.14	0.391
T8:	1.62	4.17	1.64	0.281
T9:	1.49	2.71	1.80	0.299
T10:	1.50	3.60	1.59	0.405

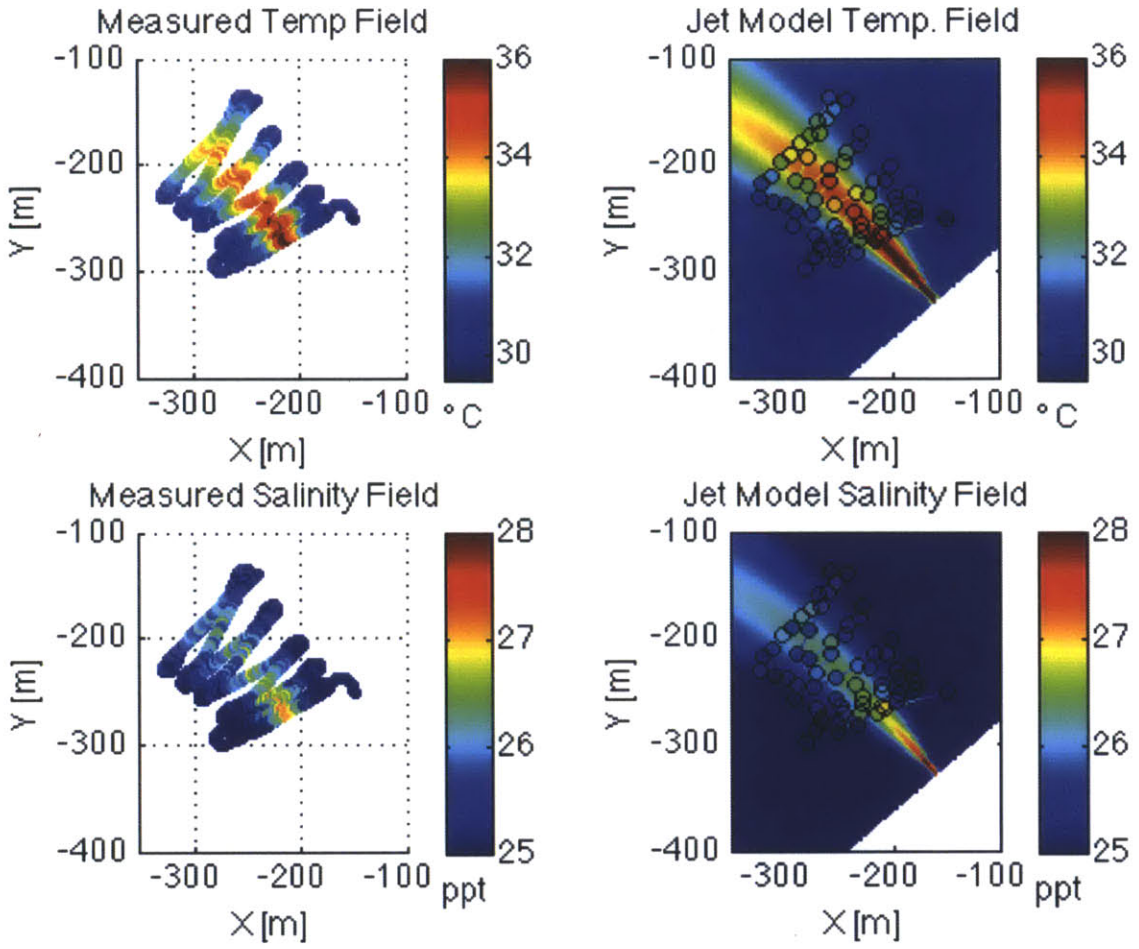

Figure 4-11: Observed (left) and Estimated (right) Temperature and Salinity Fields for a simulated solo vehicle adaptive survey mission at Site 1. The curved jet estimated fields shown coorspond to a cost of 0.94.

4.4.4 A2 Mission: Two Vehicle Adaptive Survey

An adaptive mission with two vehicles is configured to demonstrate the coordinated estimation capabilities of the sampling strategy. Edge mapping transects are also conducted. The vehicles are equipped with the same sensors as the two vehicle lawnmower survey. The first vehicle conducts a survey similar to the solo adaptive mission, but concludes the survey by completing 10 edge mapping transects on the right side of the jet. The second vehicle begins conducting transects approximately 150m downstream of the outfall. After 12 transects it begins edge mapping of the left side of the jet. The vehicle completes 8 edge mapping transects. Edge mapping transects by both vehicles are conducted with low and high thresholds of 0.2 and 0.5 respectively. Using the centerline locations detected by the second vehicle, accurate trajectory estimates are produce more quickly.

An example of this mission is summarized in Figure 4-12. Mission lengths varied from $50 - 60$min. Estimator costs of five simulations runs are shown in Table 4.5. Plots of the observations and estimation results for trial one are shown in Figure 4-13.

Table 4.6: A2 Mission Results

	Str. Cost	**Traj. Cost**	**Curved Cost**	**pRMSRE**
T1:	1.33	3.63	1.33	0.233
T2:	2.09	3.48	2.28	0.496
T3:	1.24	4.67	1.90	0.101
T4:	1.58	3.70	2.07	0.336
T5:	1.27	4.23	1.39	0.369
T6:	1.31	3.95	1.71	0.312
T7:	1.21	5.09	2.24	0.239
T8:	1.23	4.33	1.43	0.239
T9:	1.24	3.84	1.85	0.279
T10:	1.24	4.08	1.88	0.263

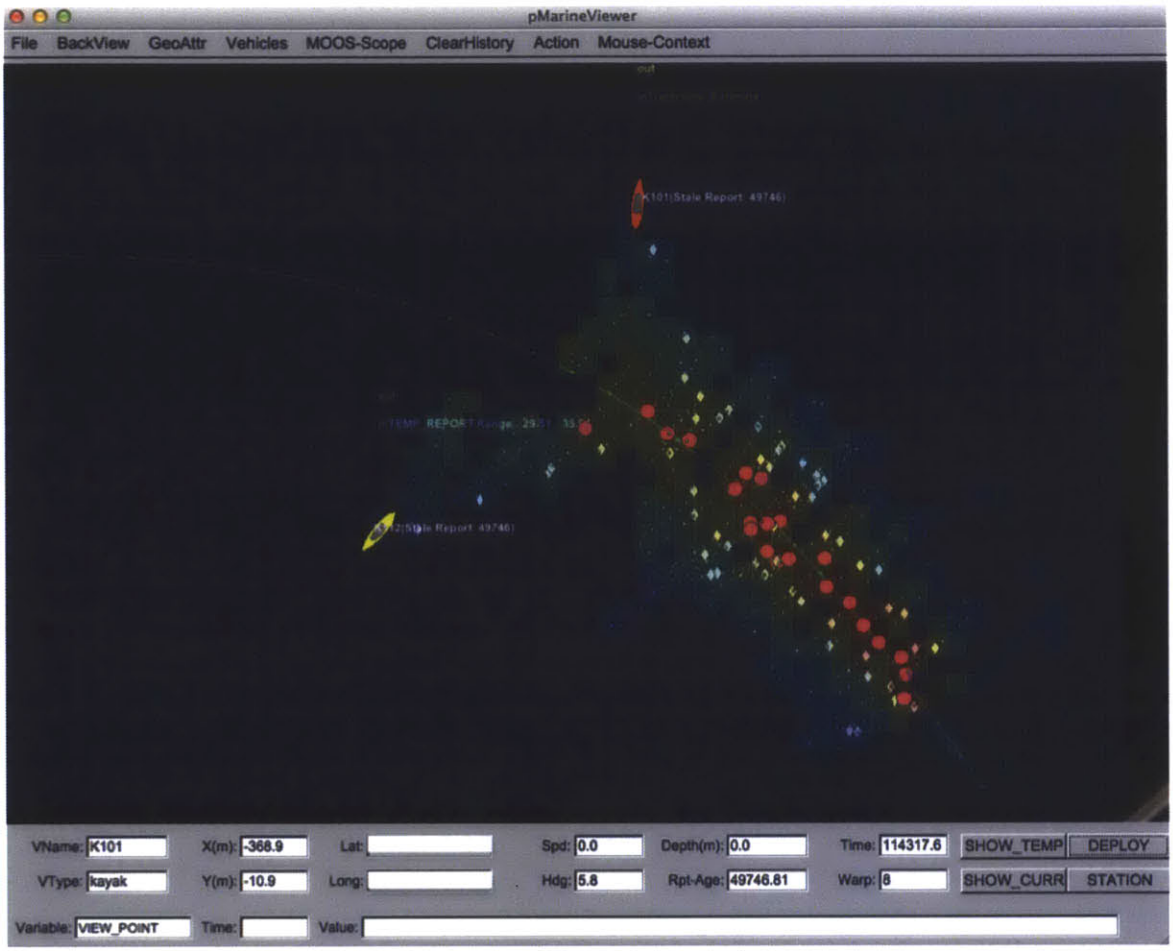

Figure 4-12: Simulated two vehicle survey exhibiting trajectory following and boundary tracking. Temperature field is shown.

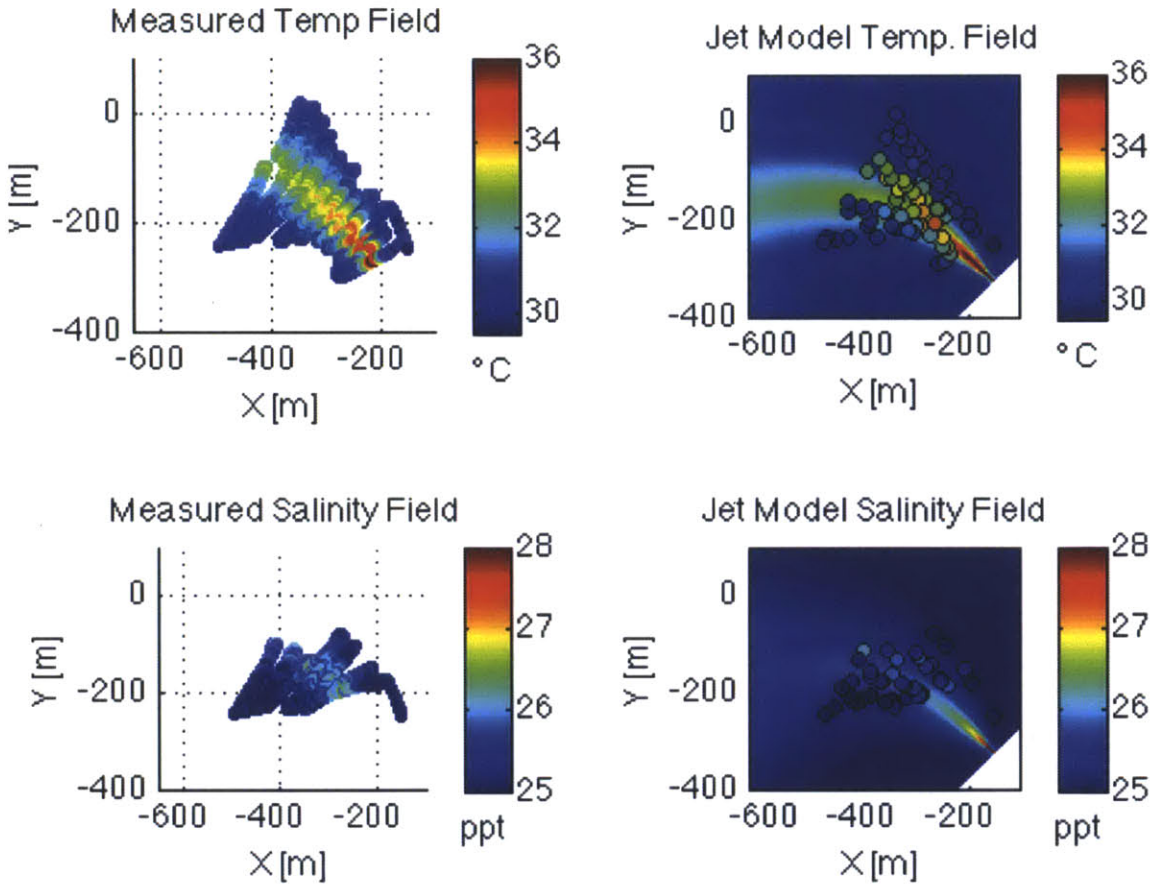

Figure 4-13: Observed (left) and Estimated (right) Temperature and Salinity Fields for a simulated two vehicle adaptive survey mission at Site 1. The curved jet estimated fields shown coorspond to a cost of 1.38.

4.4.5 Discussion

Comparing the simulation results demonstrate that the adaptive strategy is able to map the jet and plume and in some scenarios provide more accurate estimation results than predefined lawnmower surveys. The average pMRSRE results for the four surveys are listed in Table 4.7. The LM2, A1 and A2 missions perform significantly better than the LM1 missions. These surveys produced estimation results with lower pRMSRE than the LM1. This can be attributed to better jet trajectory estimates in both cases due to better centerline location estimates in the case of the adaptive missions and the addition of far field measurements in the LM2 missions. In addition to having less accurate estimation results, the predicted jet parameters of the LM1 missions exhibit higher variance, suggesting that the measurements collect in this mission produce non-unique parameter estimations.

Table 4.7: Average pRMSRE Results for Simulation Missions

LM1	0.395 SD 0.24
LM2	0.251 SD 0.13
A1	0.301 SD 0.072
A2	0.287 SD 0.10

The comparable pRMSRE results between the LM2 mission and the adaptive missions show that appropriately configured lawnmower surveys can characterize the jet's features. This finding suggests that given the needs of a mission, adaptive and predefined surveys could be used in tandem to achieve accurate characterization. For example, adaptive boundary mapping surveys executed near an outfall could be deployed alongside multiple vehicle lawnmower surveys. This class of mission is valuable since risk mitigation concerns limit the implementation of extensive autonomous functionality in certain marine vehicle deployments [40, 31]. This issue is addressed with an additional simulation mission.

4.4.6 Four Vehicle Mission with Collision Avoidance

Two primary concerns when conducting field trials are the safety of equipment and delivery of a data product. The emergent and experimental nature of new adaptive strategies can call these concerns into question. In order to secure the delivery of a data product, pre-defined surveys may be conducted in addition to adaptive ones. Equipment safety would normally dictate that these surveys be conducted separately. Time constraints as well as the dynamic characteristics of a feature make this a non-ideal scenario. Instead it would be desirable to deploy both surveys simultaneously in such a way to ensure equipment safety.

This type of mission is achievable with BHV_JetEdge and MOOS-IvP's multi-behavior optimization. This functionality of BHV_JetEdge and MOOS-IvP is demonstrated in an adaptive mission consisting of four vehicles running a collision avoidance behavior. The two vehicles conduct the LM2 mission described earlier. A third vehicle is configured to conduct boundary mapping adaptive transects on the right side of the jet using a CTD. A fourth vehicle completes 12 adaptive transects using a CTD. An additional stationary vehicle is deployed to simulate an obstacle, such as a fishing boat or buoy. Parameter estimations are conducted locally on the S1 lawnmower vehicle. The mission is deployed on a wider jet to demonstrate the utility of the combined adaptive and predefined sample sets.

The avoidance behavior, known as BHV_AvoidCollision, is provided with MOOS-IvP. It utilizes position information shared among vehicles to produce speed and heading objective functions that penalizes collision-producing maneuvers. When used in conjunction with BHV_JetEdge or a waypoint behavior, BHV_AvoidCollision tends to bend trajectories away from other vehicles and obstacles without prohibiting vehicles from returning to track lines or reaching waypoints.

The vehicle paths for this mission are shown in Figure 4-14. Despite the overlapping operation regions of the vehicles, the collision avoidance behavior served its purpose. The vehicles simultaneously sampled the jet in a using adaptive and predefined strategies while maintaining collision-free paths. Total mission length was

46min and estimator results produced a pRMSRE of 0.29.

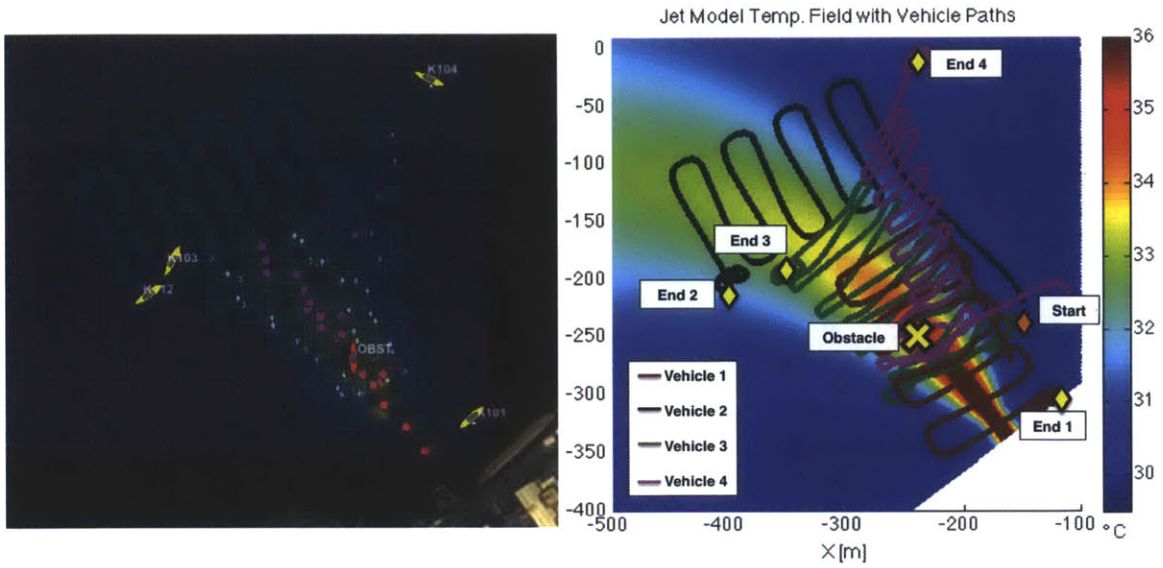

Figure 4-14: Left: The four vehicle adapative and lawnmower mission shown in the mission viewer. An obstacle vehicle is shown in red. Right: Color coded paths of the vehilcles are shown overlaid over the curved jet estimate produced during the mission. pRMSRE is 0.29.

4.5 Field Results

The sampling strategy was implemented in the field at Site 1 using a SCOUT autonomous kayak. Temperature and salinity were chosen as the indicator function fields due to their elevated levels in historical jet data. Unfortunately, hardware issues limited the trials to one kayak equipped with a multi-parameter YSI sonde probe mounted on the kayak's underside.

Much like the solo adaptive simulation mission described above, the sampling mission instructed the vehicle to conduct one predefined transect of the jet and then proceed to adaptive transects. The behavior configuration used on this mission appears in Table 4.8. Despite being configured to complete 25 transects, a lightening storm cut the mission short. The final transect count was 15 transects ranging in length of 130m to 150m. These transects extended up to 275m from the outfall. A

screen shot of the mission viewer during this mission is shown in 4-15. pSensorData provides an overlay of the live temperature measurements.

Table 4.8: Behavior Parameters for Field Trial

Parameter	Value
POINTS	(-240,-320):(-140,-265)
MODE	0
SIDE	left
EDGE_SIDE	N/A
THRESH	0.62
LOW	N/A
HIGH	N/A
Y_DELTA	25m
THRESH_COUNT	30
EDGE_PAD	15m
NUM_PASS	25
EDGE_PASS	0
TRAJ_PASS	6

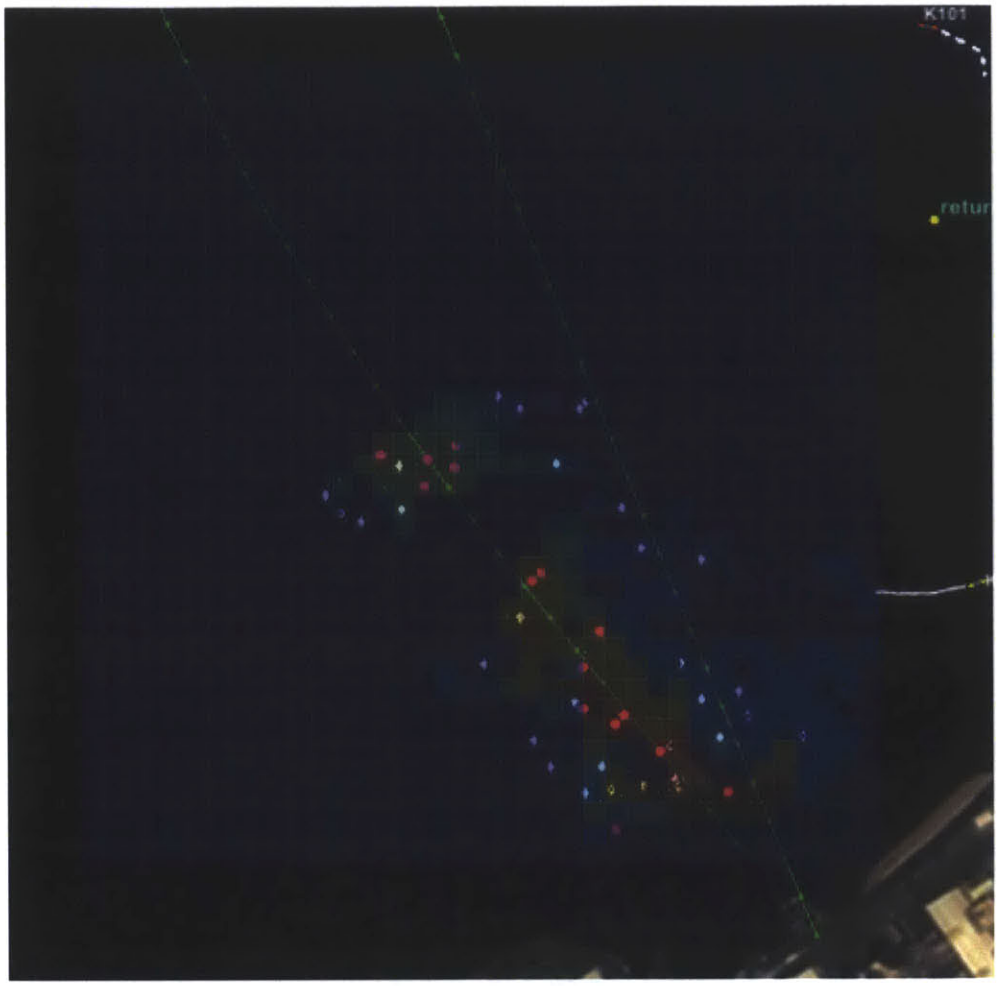

Figure 4-15: Screen shot of mission viewer taken during adaptive field mission. Live temperature measurements are shown in an overlay produced by pSensorData. BHV_-JetEdge visual cues show centerline locations in pink circles, theshold marks in white diamonds and the trajectory estimate with green lines. Trajectory estimate on right is an old estimate that was updated to the trajectory shown on the left.

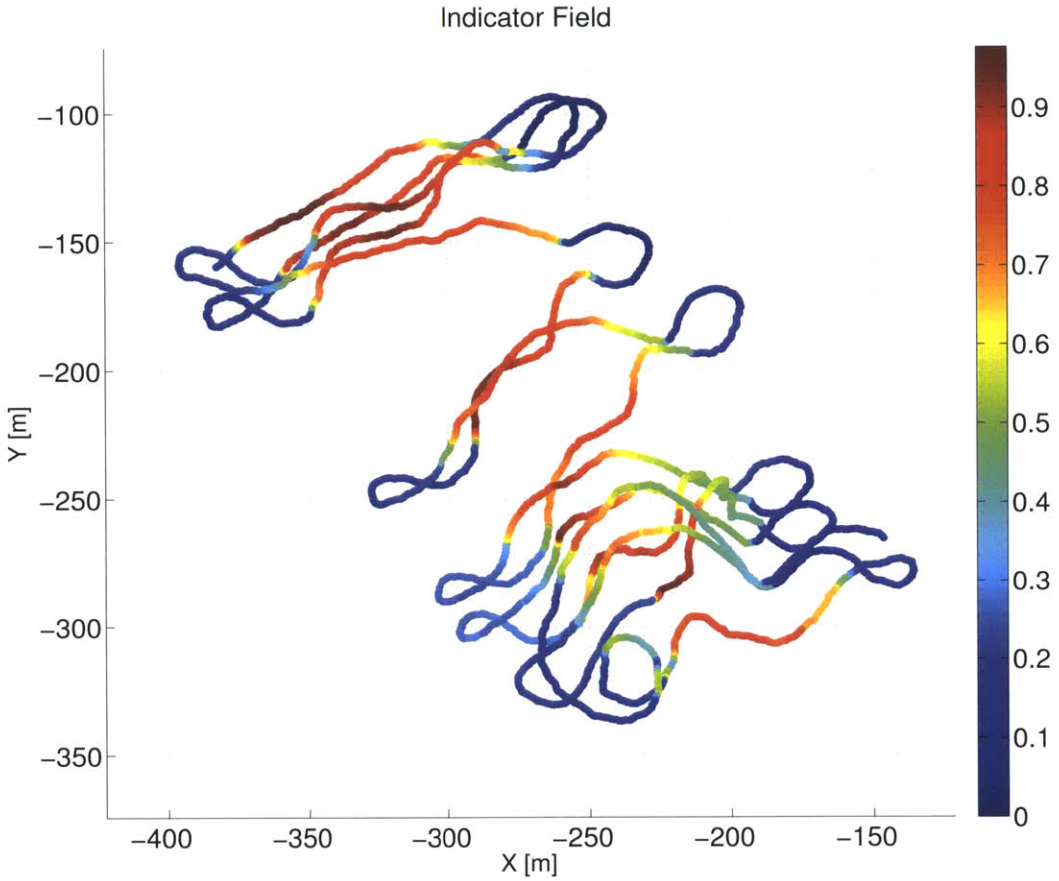

Figure 4-16: Vehicle path and indicator function field from field trial at Site 1.

The vehicle's path and the indicator function field can be viewed in Figure 4-16. Indicator function readings consistently reached peaks near unity on each transect and decayed to zero on the transect edges. These results match those predicted in Figure 4-4. Strong indicator function readings on later transects suggest that the strategy would have been successful at tracking the jet and plume for several more transects.

Unlike in the simulations, the vehicle does not follow a straight path during its transects due to the effects of the outfall current. The vehicle attempted to counteract these effects by employing track-line following on the transect headings, however it is generally too underpowered to adequately reject these disturbances. Knowing that this would be a likely issue, the behavior parameter **THRESH_COUNT** was set at a high

value of 30 to insure that threshold crossing flags would not occur prematurely due to the distorted transect path. Another notable aspect of the vehicle's path is the gap between transects 10 and 11. This gap resulted from a change in the jet trajectory estimate that occurred after transect 10. After transect 11, the trajectory estimate stabilized resulting in more consistent transect headings.

The estimator results for both the jet parameters and trajectory obtained from the temperature and salinity measurements are shown in Table 4.9. These results are used to produce the estimated temperature and salinity fields in Figure 4-17. Much like results from the historical data fits, a significantly higher centerline decay constant is estimated for the temperature field than the salinity field. With the addition of the trajectory estimate, it is possible to make some limited assumptions about the far field behavior of the resulting plume. Because of the high centerline decay constant, the temperature excess quickly becomes negligible and would not be observed in a far-field plume. On the other hand, a plume of high salinity water extends more than 400m meters into the northern area of the waterway and spans more than 300m. However, without a full 3D model that incorporates water density and mixing, an accurate prediction of the far field plumes is not possible.

Table 4.9: Jet model parameters and estimator bounds used for mission simulations.

Parameter	Estimated Results
X_O	−169.2m
Y_O	−340m
θ	126.1°
ϕ	80.2°
D_O	4.1m
U_O	1.18m/s
U_C	N/A
T_O	43.8°
T_a	31°
S_O	28.3*ppt*

Parameter	Estimated Results
S_a	24.8*ppt*
N_T	0.71
R_T	6.0
N_S	0.39
R_S	6.9
N_V	N/A
R_V	N/A
C	5
L_C	200.0m

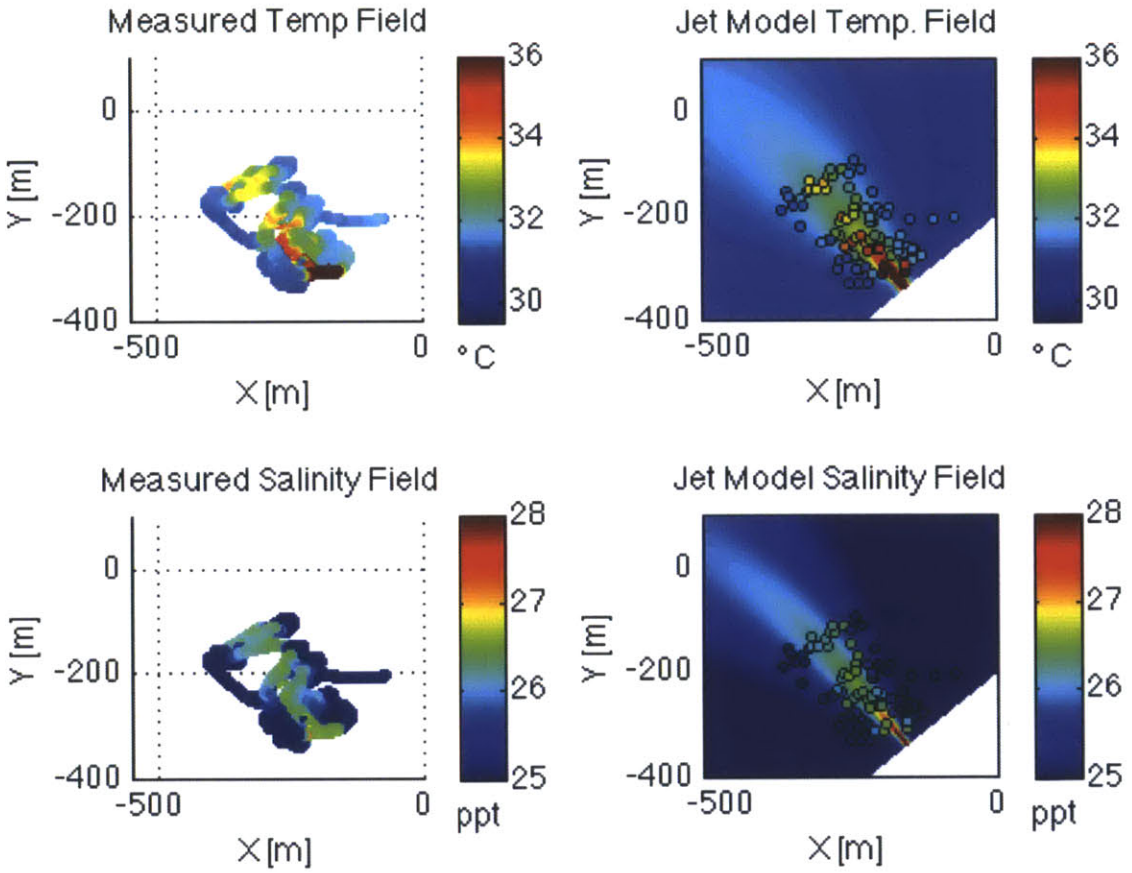

Figure 4-17: Observed (left) and Estimated (right) Temperature and Salinity Fields for a simulated two vehicle adaptive survey mission at Site 1. The curved jet estimated fields shown coorspond to a cost of 1.39.

Chapter 5

Conclusion

5.1 Summary

In this thesis a framework for autonomous sampling of thermal and effluent jets is presented. The components of this framework are able to extend the capabilities of autonomous surface vehicles sampling these marine features.

5.1.1 Reorienting ADCP

Chapter 2 presents a novel acoustic measurement system consisting of an ADCP integrated with a pan and tilt actuator. The sensing system is designed to overcome the limitations of a statically, bottom-mounted ADCPs by enabling the real-time capture of global velocity measurements and acoustic signatures over a wide range of vectors. Real-time local and remote availability of measurements results from integration with MOOS-IvP.

Experimental results from field testing are presented. The system was deployed on a SCOUT kayak at a power plant cooling outfall. Results demonstrates that they system is able to capture surface velocity measurements ahead of the vehicle and that the direction and magnitude of the processed measurements are inline with the expected velocity field produced by the outfall. A wake detection experiment was also performed using a motor boat as a wake generator. Real-time results from the

horizontally oriented instrument produced identifiable acoustic signatures indicative of the wake disturbance.

5.1.2 Thermal and Effluent Jet and Plume Model

In Chapter 3 a thermal and effluent jet and plume field model is presented. This model was developed out of a need for a versatile simulation environment for thermal and effluent jet and plume sampling.

A two dimensional model is developed that incorporates laws for spreading, centerline decay and trajectory that are derived from dimension and length scale analysis and empirical investigations. Simulating annealing parameter estimation is used to fit the model to historical data. Model fits accurately replicate jet direction, strength and spreading. The model is implemented as a C++ library to allow for integration with a variety of MOOS applications. This integration proofs to be a valuable tool for simulating sampling missions within MOOS-IvP.

5.1.3 Adaptive Sampling Strategy

Chapter 4 presents an autonomous adaptive sampling strategy developed within MOOS-IvP that is based on sensor fusion and adaptive transects. MOOS-IvP integration offers a number of important advantages. Through the sharing of estimation results, the strategy can be coordinated across multiple vehicles. The adaptive transect behavior can be deployed alongside other autonomy behaviors to create complex missions. Missions developed within a the simulation environment can be deployed in the field with minimal configuration changes.

Simulated jet and plume sampling missions demonstrate the strategy's ability to track the jet centerline and map its boundaries. Online estimation results produced by the adaptive strategy are comparable to those produced using a two lawnmower mission. A field test of the strategy successfully completes 15 adaptive transects at thermal and effluent jet produce by a power plan cooling outfall. Online estimation results are reported.

5.2 Future Work

In the future, components of this framework could be enhanced in a number of ways. The reorienting ADCP system is at an early stage of development and current tests have mainly been a proof of concept. Error and noise in the reported measurements are major concern given that the current implementation lacks precision below 30cm/s. Measurement localization and accuracy could be improved by integrating a high accuracy inertial and GPS measurement unit and filtering raw ADCP outputs. Future experiments conducted on thermal and effluent jets can utilize real-time velocity measurements for online jet parameter estimation. The estimation results could be used by path planning algorithms to produce current optimized paths. Wake detection and tracking could be automated using algorithms developed for visual servoing that track the acoustic wake signature.

The thermal and effluent jet and plume model made a number of simplifications for buoyancy, crossflow and confinement. A three dimensional model that accounted for these effects would allow for higher fidelity simulations and could be used to simulate AUV sampling. Since jet and wake flows share similar characteristics, the model could be adaptive to simulate vehicle wakes within MOOS-IvP. This wake model then could be used to further develop the reorienting ADCP system. Computational performance of the model is lacking for the curve jet case. An improved interpolation methodology or discretation of the model would increase performance.

The adaptive sampling strategy presented here could potential be combined with other sampling techniques to decrease mission time and improve estimation accuracy. Estimations produced by adaptive transects near the outfall could be use to identify areas of high uncertainty to where further sampling could be deployed. Techniques, such as those described in [13], could also make use of the estimates to produce adaptive sampling paths that minimize reconstruction error. Any further enhancements to the presented strategy should be implemented within MOOS-IvP in order to leverage the jet and plume sampling simulation environment and simplify future field testing.

Appendix A

MOOS and MOOS-IvP

MOOS-IvP is considered an autonomy middleware system made up of a number of modules that operate within a shared infrastructure. MOOS-IvP is an extension of MOOS that enables and coordinates behavior-based control of MOOS nodes and provides tools for custom behavior development and field deployment. These modules are separated into two classes: applications and behaviors. Applications control specific functionality such sensor control, navigation, networking and communication. Behaviors provide back-seat driver autonomy by selecting desirable heading, speed and depth.

A number of well tested, basic functionality applications and behaviors are publicly available. These modules can be easily integrated with user developed modules for specific circumstances. Most applications and behaviors are designed to be separate and distinct. This allows for the modification of existing modules and development of new modules, while maintaining the integrity of MOOS-IvP as a whole.

Central to the MOOS-IvP infrastructure is MOOS-IvP Core. Within the standard MOOS framework, the Core utilizes a central database, the MOOSDB, and algorithms for scheduling and passing messages. The IvP expands this to include a multi-objective optimization solver and behavior-based control. The IvP also adds a set of observation and control applications and utilities for simulating and implementing inter-node communications. With the addition of the IvP, the MOOS-IvP infrastructure configures communication and control of the software processes running

across autonomous and operator platforms.

The pre-mission simulation capabilities of MOOS-IvP are developed by creating MOOS-IvP modules to represent aspects of the real world, including processes such as sensor operations or vehicle dynamics. Using simulated data, these modules can be integrated within the MOOS-IVP infrastructure and used to plan missions. By exchanging the simulated modules for hardware-based alternatives, a vehicle mission that is planned and simulated within MOOS can be implemented in the field with minimal changes to the architecture.

Within MOOS-IvP, vehicle autonomy is coordinated by the application, IvP Helm. The IvP Helm utilizes a behavior-based architecture to compute desirable values of autonomy control domains, such as vehicle heading, speed and depth. A MOOS-IvP behavior is a standalone module that outputs objective function(s) across the Helm decision space based on the MOOSDB state. Individual behaviors control specific aspects of vehicle autonomy such as waypoint following, obstacle avoidance and speed control. The primary purpose of the IvP-Helm is to solve the multi-objective optimization problem thats resolves different behaviors and produces the desired control domain set-points. This optimization is accomplished through a methodology known as interval programming, described in [8].

Appendix B

Proto File

```
1  package adcpmess;

3  message ADCP_ensemble{
   //fixed leaders
5          optional int32 year = 1;
           optional int32 month = 2;
7          optional int32 day = 3;
           optional int32 hour = 4;
9          optional int32 minute = 5;
           optional int32 second = 6;
11         optional int32 hundreds = 7;

13 //variable leaders
           optional int32 depth_trans = 8;
15         optional double s_ofsound = 9;
           optional int32 bin1 = 10;
17         optional int32 pings = 11;
           optional int32 cell_size = 12;
19         optional int32 num_cells = 13;
           optional double x = 14;
21         optional double y = 15;
           optional double yaw = 16;
23         optional double pitch = 17;
           optional double roll = 18;
```

```
25          optional double heading = 19;
            optional double speed = 20;
27          optional double pan = 21;
            optional double tilt = 22;
29          optional bool trans = 24;
            optional double moostime = 25;
31
    //repeated fields froms bins
33          message Data_Field{

35                  optional double velocity1 = 1;
                    optional double velocity2 = 2;
37                  optional double velocity3 = 3;
                    optional double velocity4 = 4;
39
                    optional double corrmag1 = 5;
41                  optional double corrmag2 = 6;
                    optional double corrmag3 = 7;
43                  optional double corrmag4 = 8;

45                  optional double echo1 = 9;
                    optional double echo2 = 10;
47                  optional double echo3 = 11;
                    optional double echo4 = 12;
49
                    optional double pgood1 = 13;
51                  optional double pgood2 = 14;
                    optional double pgood3 = 15;
53                  optional double pgood4 = 16;

55                  optional double positionX = 17;
                    optional double positionY = 18;
57                  optional double positionZ = 19;
                    optional double positionE = 20;
59
                    optional int32 bin = 21;
```

```
61          }
            repeated Data_Field fields = 23;
63  }
```

Bibliography

[1] M. E. Abou-Elhaggag, M. H. El-Gamal, and M. I. Farouk. Experimental and numerical investigation of desalination plant outfalls in limited disposal areas. *Journal of Environmental Protection*, 2(6):828–839, 2011.

[2] Jim Aiken, Gerald F. Moore, and Patrick M. Hotligan. Remote sensing of oceanic biology in relation to global climate change. *Journal of Phycology*, 28(5):579–590, 1992.

[3] M. L. Albertson, YB Dai, RA Jensen, and H. Rouse. Diffusion of submerged jets. *Transactions of the American Society of Civil Engineers*, 115(1):639 664, 1950.

[4] C. S. Albro and A. D. Mansfield. Comparison of real time plume tracking methods in coastal waters. In *IEEE OCEANS 2006*, pages 1–6. IEEE, 2006.

[5] Donald Anderson, Patricia Glibert, and Joann Burkholder. Harmful algal blooms and eutrophication: Nutrient sources, composition, and consequences. *Estuaries and Coasts*, 25(4):704–726, 08 2002.

[6] V. Balasubramanian and S. C. Jain. Horizontal buoyant jets in quiescent shallow water. *Journal of the Environmental Engineering Division*, 104(4):717–730, 1978.

[7] A. Balasuriya, S. Petillo, H. Schmidt, and M. Benjamin. Behavior-based planning and prosecution architecture for autonomous underwater vehicles in ocean observatories. In *IEEE OCEANS 2010*, pages 1 –5, may 2010.

[8] M. R. Benjamin. The interval programming model for multi-objective decision making. Technical report, MIT Computer Science and Artificial Intelligence Lab, 2004.

[9] Keith Beven and Jim Freer. Equifinality, data assimilation, and uncertainty estimation in mechanistic modelling of complex environmental systems using the glue methodology. *Journal of Hydrology*, 249(1–4):11–29, 8 2001.

[10] Dominique N. Brocard. Surface buoyant jets in steady and reversing crossflows. *Journal of Hydraulic Engineering*, 111(5):793–809, May 1985.

[11] C.J. Cannell, A.S. Gadre, and D.J. Stilwell. Boundary tracking and rapid mapping of a thermal plume using an autonomous vehicle. In *IEEE OCEANS 2006*, pages 1 –6, sept. 2006.

[12] G. Carazzo, E. Kaminski, and S. Tait. The route to self-similarity in turbulent jets and plumes. *Journal of Fluid Mechanics*, 547:137–148, 2006.

[13] B. Chen, P. Pandey, and D. Pompili. A distributed adaptive sampling soluting using autonomous underwater vehicles. Technical report, Rutgers University Dept. of Electrical and Computer Engineering, 2012.

[14] D. Chen and G. H. Jirka. Lif study of plane jet bounded in shallow water layer. *Journal of Hydraulic Engineering*, 125(8):817–826, 1999.

[15] V. H. Chu and J. H. W. Lee. General integral formulation of turbulent buoyant jets in cross-flow. *Journal of Hydraulic Engineering*, 122(1):27–34, 1996.

[16] Vincent H. Chu and Gerhard H. Jirka. *Encylopedia of Fluid Mechanics*, volume 6, chapter Surface Buoyant Jets and Plumes, pages 1053 10–84. Gulf Publishing Company, Houston, 1987.

[17] I. Chuine, P. Cour, and D. D. Rousseau. Fitting models predicting dates of flowering of temperate-zone trees using simulated annealing. *Plant, Cell Environment*, 21(5):455–466, 1998.

[18] Joseph Curcio. Robotic marine systems. `http://www.maribotics.com/`.

[19] M. Devlin and B. Schaffelke. Spatial extent of riverine flood plumes and exposure of marine ecosystems in the tully coastal region, great barrier reef. *Marine and Freshwater Research*, 60(11):1109–1122, 2009.

[20] Gary D. Egbert and Svetlana Y. Erofeeva. Efficient inverse modeling of barotropic ocean tides. *Journal of Atmospheric and Oceanic Technology*, 19(2):183–204, 2012/11/19 2002.

[21] G. Evensen. Inverse methods and data assimilation in nonlinear ocean models. *Physica D: Nonlinear Phenomena*, 77(1):108–129, 1994.

[22] J. A. Farrell, S. Pang, and W. Li. Chemical plume tracing via an autonomous underwater vehicle. *Oceanic Engineering, IEEE Journal of*, 30(2):428–442, 2005.

[23] A. Fraser and D. Burnell. *Computer models in genetics.* New York and London: McGraw-Hill Book Company, 1970.

[24] W. E. Frick. Non-empirical closure of the plume equations. *Atmospheric Environment (1967)*, 18(4):653–662, 1984.

[25] P. M. Glibert, J. H. Landsberg, J. J. Evans, M. A. Al-Sarawi, M. Faraj, M. A. Al-Jarallah, A. Haywood, S. Ibrahem, P. Klesius, and C. Powell. A fish kill of massive proportion in kuwait bay, arabian gulf, 2001: the roles of bacterial disease, harmful algae, and eutrophication. *Harmful Algae*, 1(2):215–231, 2002.

[26] Google. Protocal buffers developer guide. `http://code.google.com/apis/protocolbuffers/docs/overview.html`, September 2012.

[27] S. Hoerner. *Fluid-Dynamic Drag*. Hoerner Fluid Dynamics, Bricktown, New Jersey, 1992.

[28] Teleydne RDI Inc. Acoustic doppler current profiler principles of operations: A practical primer. Technical report, Teledyne RD Instruments, Inc., San Diego, CA, 2011.

[29] H. Ishida, T. Nakamoto, T. Moriizumi, T. Kikas, and J. Janata. Plume-tracking robots: A new application of chemical sensors. *The Biological Bulletin*, 200(2):222 226, 2001.

[30] Hiroshi Ishida, Takamichi Nakamoto, and Toyosaka Moriizumi. Remote sensing of gas/odor source location and concentration distribution using mobile system. *Sensors and Actuators B: Chemical*, 49(1–2):52 57, 6 1998.

[31] M. Jakuba and D. Yoerger. Autonomous search for hydrothermal vent fields with occupancy grid maps. In *Australasian Conference on Robotics and Automation*, volume 8, page 2008, Canberra, Australia., 2008.

[32] M. V. Jakuba, J. C. Kinsey, D. R. Yoerger, R. Camilli, C. A. Murphy, D. Steinberg, and A. Bender. Exploration of the gulf of mexico oil spill with the sentry autonomous underwater vehicle. *Intelligent Robots and Systems (IROS), 2010 IEEE/RSJ International Conference on*, 2010.

[33] S. Jeong, S. W. Ban, S. Choi, D. Lee, and M. Lee. Surface ship-wake detection using active sonar and one-class support vector machine. *Oceanic Engineering, IEEE Journal of*, 37(3):456 466, 2012.

[34] G. H. Jirka. Buoyant surface discharges into water bodies. ii: Jet integral model. *Journal of Hydraulic Engineering*, 133(9):1021–1036, 2007.

[35] AJ Johnston, CR Phillips, and RE Volker. Modeling horizontal round buoyant jets in shallow water. *Journal of Hydraulic Engineering*, 120(1):41–59, 1994.

[36] G. R. Jones, J. D. Nash, R. L. Doneker, and G. H. Jirka. Buoyant surface discharges into water bodies. i: Flow classification and prediction methodology. *Journal of Hydraulic Engineering*, 133(9):1010–1020, 2007.

[37] GK Jones, JL Baker, K Edyvane, and GJ Wright. Nearshore fish community of the port river-barker inlet estuary, south australia. i. effect of thermal effluent on the fish community structure, and distribution and growth of economically important fish species. *Marine and Freshwater Research*, 47(6):785–799, 01 1996.

[38] S. J. Julier and J. K. Uhlmann. Unscented filtering and nonlinear estimation. *Proceedings of the IEEE*, 92(3):401–422, 2004.

[39] R. T. Kessel and R. D. Hollett. Underwater intruder detection sonar for harbour protection: state of the art review and implications. In *IEEE international conference on technologies for homeland security and safety*, Istanbul, Turkey, 2006. DTIC Document.

[40] J. C. Kinsey, D. R. Yoerger, M. V. Jakuba, R. Camilli, C. R. Fisher, and C. R. German. Assessing the deepwater horizon oil spill with the sentry autonomous underwater vehicle. *Intelligent Robots and Systems (IROS), 2011 IEEE/RSJ International Conference on*, pages 261–267, 2011.

[41] S. Kirkpatrick, C. D. Gelatt, and M. P. Vecchi. Optimization by simulated annealing. *Science*, 220(4598):671–680, 1983.

[42] K. Kurihara, M. Welling, and N. Vlassis. Accelerated variational dirichlet process mixtures. *Advances in Neural Information Processing Systems*, 19:761, 2007.

[43] M.B. Larsen. High performance doppler-inertial navigation-experimental results. In *IEEE OCEANS 2000*, volume 2, pages 1449 –1456 vol.2, 2000.

[44] J. H. W. Lee and V. Cheung. Generalized lagrangian model for buoyant jets in current. *Journal of environmental engineering*, 116(6):1085–1106, 1990.

[45] J. H. W. Lee and V. H. Chu. *Turbulent jets and plumes: A Lagrangian approach*. Springer, 2003.

[46] P.M. Lee, B.H. Jeon, S.M. Kim, H.T. Choi, C.M. Lee, T. Aoki, and T. Hyakudome. An integrated navigation system for autonomous underwater vehicles with two range sonars, inertial sensors and doppler velocity log. In *IEEE OCEANS 2004*, volume 3, pages 1586 – 1593 Vol.3, nov. 2004.

[47] W. Li, J. A. Farrell, and R. T. Card. Tracking of fluid-advected odor plumes: strategies inspired by insect orientation to pheromone. *Adaptive Behavior*, 9(3-4):143–170, 2001.

[48] K.W. Lo and B.G. Ferguson. Automatic detection and tracking of a small surface watercraft in shallow water using a high-frequency active sonar. *Aerospace and Electronic Systems, IEEE Transactions on*, 40(4):1377 – 1388, oct. 2004.

[49] Norman H. Brooks Loh-Nien Fan. Turbulent buoyant jets into stratified or flowing ambient fluids. Technical Report Report Number KH-R-15, California Institue of Technology, 1967.

[50] Alexis Lugo-Fernández. Is the loop current a chaotic oscillator? *Journal of Physical Oceanography*, 37(6):1455–1469, 2012/10/15 2007.

[51] D. Lukšienė, O. Sandström, L. Lounasheimo, and J. Andersson. The effects of thermal effluent exposure on the gametogenesis of female fish. *Journal of Fish Biology*, 56(1):37 50, 2000.

[52] S. Mau, M. B. Heintz, F. S. Kinnaman, and D. L. Valentine. Compositional variability and air-sea flux of ethane and propane in the plume of a large, marine seep field near coal oil point, ca. *Geo-Marine Letters*, 30(3):367–378, 2010.

[53] S. N. Michas and P. N. Papanicolaou. Horizontal round heated jets into calm uniform ambient. *Desalination*, 248(1-3):803–815, 2009.

[54] Ocean Server Technology Inc., Fallriver, MA. *Digital Compass Users Guide, OS5000 Serires*, 2011.

[55] Oceanscience. Oceanscience develop multi-profiler instrumentation boat to compare teledyne rd instruments and sontek/ysi acoustic doppler current profilers (adcps). `http://www.oceanscience.com/news/detail.aspx?nid=23`.

[56] Library of Congress-Federal Reserach Division. Country profile: Singapore. `http://lcweb2.loc.gov/frd/cs/profiles/Singapore.pdf`.

[57] Oxford Technology Solutions Limited, Oxfordshire, England. *Intertial+ User Manual*, 2011.

[58] P. Piedras, E. Bay, P. Buchon, and P. Arguello. Offshore monitoring and reporting program quarterly report water-colmn sampling may 2009 survey. Technical report, City of Morro Bay and Cayucos Sanitary District, 2008.

[59] Stephen B. Pope. *Turbulent Flows*. Cambridge University Press, New Yorl, eighth edition, 2011.

[60] FP Ricou and DB Spalding. Measurements of entrainment by axisymmetrical turbulent jets. *J. Fluid Mech*, 11(1):21 31, 1961.

[61] P. Rigby, O. Pizarro, and S.B. Williams. Towards geo-referenced auv navigation through fusion of usbl and dvl measurements. In *IEEE OCEANS 2006*, pages 1 6, sept. 2006.

[62] D. Roemmich, G. C. Johnson, S. Riser, R. Davis, J. Gilson, W. B. Owens, S. L. Garzoli, C. Schmid, and M. Ignaszewski. The argo program: Observing the global ocean with profiling floats. *Oceanography*, 22:34–43, 2009.

[63] S. Ruiz, B. Garau, M. Martínez-Ledesma, B. Casas, A. Pascual, G. Vizoso, J. Bouffard, E. Heslop, A. Alvarez, and P. Testor. New technologies for marine research: five years of glider activities at imedea. *Scientia Marina*, 76(S1):261–270, 2012.

[64] Alexander F. Shchepetkin and James C. McWilliams. The regional oceanic modeling system (roms): a split-explicit, free-surface, topography-following-coordinate oceanic model. *Ocean Modelling*, 9(4):347 404, 2005.

[65] AM Shinneeb. Confinement effects in shallow-water jets. *Journal of Hydraulic Engineering*, 137(3):300–314, March 2011.

[66] B. J. Shuter, D. A. Wismer, H. A. Regier, and J. E. Matuszek. An application of ecological modelling: Impact of thermal effluent on a smallmouth bass population. *Transactions of the American Fisheries Society*, 114(5):631–651, 2012/10/18 1985.

[67] R.N. Smith, A. Pereira, Yi Chao, P.P. Li, D.A. Caron, B.H. Jones, and G.S. Sukhatme. Autonomous underwater vehicle trajectory design coupled with predictive ocean models: A case study. In *Robotics and Automation (ICRA), 2010 IEEE International Conference on*, pages 4770 –4777, may 2010.

[68] R. J. Sobey, A. J. Johnston, and R. D. Keane. Horizontal round buoyant jet in shallow water. *Journal of Hydraulic Engineering*, 114(8):910–929, 1988.

[69] Lorin E. Squires, Samuel R. Rushforth, and Jack D. Brotherson. Algal response to a thermal effluent: study of a power station on the provo river, Utah, USA. *Hydrobiologia*, 63(1):17–32, 03 1979.

[70] Teledyne RD Instrument. *ExplorerDVL Operation Manual*, 2010.

[71] Gabriel A. Vecchi and Brian J. Soden. Global warming and the weakening of the tropical circulation. *Journal of Climate*, 20(17):4316–4340, 2012/10/15 2007.

[72] Ding Wang, Pierre F. J. Lermusiaux, Patrick J. Haley, Donald Eickstedt, Wayne G. Leslie, and Henrik Schmidt. Acoustically focused adaptive sampling and on-board routing for marine rapid environmental assessment. *Journal of Marine Systems*, 78, Supplement(0):S393–S407, 11 2009.

[73] S. J. Wright. Mean behavior of buoyant jets in a crossflow. *Journal of the Hydraulics Division*, 103(5):499–513, 1977.

[74] Jing Yu, Dan-Ling Tang, Im-Sang Oh, and Li-Jun Yao. Response of harmful algal blooms to environmental changes in daya bay, china. *err. Atmos. Ocean. Sci. 18, 1011-1027, doi: 10.3319/TAO.2007.18.5.1011(Oc).*, 18(5):1011–1027, 2007.